EXPERIMENTAL NANOMECHANICS OF 1D NANOSTRUCTURES

A Thesis
Presented to
The Academic Faculty

by

BHASKAR PANT

In Partial Fulfillment
of the Requirements for the Degree
Master of Science in the
George W. Woodruff School of Mechanical Engineering

Georgia Institute of Technology
August 2010

EXPERIMENTAL NANOMECHANICS OF 1D NANOSTRUCTURES

Approved by:

Dr. Olivier Pierron, Advisor
George W. Woodruff School of Mechanical Engineering
Georgia Institute of Technology

Dr. Ken Gall
School of Material Science and Engineering
Georgia Institute of Technology

Dr. Ting Zu
George W. Woodruff School of Mechanical Engineering
Georgia Institute of Technology

Date Approved: June 30, 2010

ACKNOWLEDGEMENTS

I wish to express my gratitude to my academic advisor Dr. Olivier Pierron for his continuous support, exceptional accessibility and the invaluable guidance that led to the present work.

I would like to thank Dr. Gall and Dr. Zhu for the insightful discussions during our group meetings.

I am also thankful to Dr. Samuel Graham and Dr. Yogendra Joshi for providing access to their quality laboratory equipment and for the invaluable technical assistance I received from their students.

I would also like to thank Eva Baumert, Sukwon Choi, Christine Taylor and Vivek Sahu for their invaluable contributions to the work.

Special thanks to my friends and family for their continuous support and understanding without which this work would not have been possible.

TABLE OF CONTENTS

LIST OF TABLES

LIST OF FIGURES

Page

SUMMARY

Nanotechnology offers great promise for the development of nanodevices. Hence it becomes important to study the mechanical behavior of nanostructures for their use in such systems. MEMS (Micro ElectroMechanical Systems) provide an effective and precise method for testing nanostructures. Consequently this study focuses on the development of a MEMS thermal nanotensile tester to investigate the mechanical behavior of one-dimensional nanostructures. Extensive characterization of these MEMS devices (structural, electrical and thermal behavior) was performed using experimental as well as finite element methods.

Tensile testing of nanostructures requires manipulation of individual nanostructures on the MEMS device. The study involves the development of an efficient methodology for the manipulation of nanowires and nanobeams for nanoscale testing.

Furthermore, two different sensing schemes for the developed devices, namely capacitive and resistive, have been extensively investigated and the advantages and various issues related to both have been discussed. Nanocrystalline (nc) Ni nanobeams (typical dimensions of 500 nm x 200 nm x 20 μm) have been tested to failure using the MEMS devices.

Improvements in the design for the MEMS nanotensile tester have been suggested to significantly enhance the device performance and to resolve the various issues involved with nano scale tests. Differential capacitive sensing for stress-strain measurements has been suggested to improve the accuracy of strain measurements.

CHAPTER 1

INTRODUCTION

1.1 Nanotechnology and Applications

As an emerging technology, nanotechnology offers great promise in the development of Nanoelectronics and Nano ElectroMechanical Systems (NEMS) [1-9]. Due to the unique properties of materials at submicron scales and miniaturization advantages, this technology has found several applications, like chemical and biological sensors, electronics, drug delivery systems, nano-transducers, nanotube based pressure sensors etc. NEMS form the next logical step in miniaturization of Micro ElectroMechanical Systems (MEMS). NEMS have shown a very high potential for the future development of highly sensitive low power sensors and hence has attracted significant interest recently. Potential applications include resonant sensors [1] comprised of structures supported over nanowires/nanocantilevers providing molecular level sensitivity, piezoresistive applications of nanowires in sensors (silicon nanowires have shown unusually large piezoresistive effect as compared to bulk [2]). The piezoresistive effect of nanoscale silicon and germanium is being actively researched for possible performance enhancement of transistors [3, 4]. Carbon nanotubes have also been proposed for the development of nanoelectromechanical sensors for various applications [5-8]. Furthermore nanowires have promising applications in the development of high performance flexible supercapacitors [9].

However for such applications, the knowledge of mechanical properties of such nanoscale 1-D materials is essential. In case of nanostructures (typical dimensions ranging from 10s of nm to submicron structures), the large ratio of atoms on the surface to the bulk has shown to have a profound effect on their properties [10-16].

Typically, the yield strength of materials shows an increasing trend with decreasing sample dimensions for monocrystalline materials, i.e. materials tend to get stronger and stronger as we go from bulk to nanoscales [10, 11, 15, 16]. Some studies also show an increasing trend for Young's modulus with decreasing sample dimensions for Ag and Pb nanowires [10, 11]. Consequently it becomes extremely important to probe their properties which may be very different from their bulk counterparts due to surface effects, which includes the effects of surface roughness, oxidation layer, surface stress etc. [11].

1.2 Nanoscale Testing Methodologies

The promising applications of nanotechnology and NEMS (refer Section 1.1) initiated the development of various techniques to determine the properties of 1-D nanoscale materials over the recent years. Several of these developments are reviewed next.

1.2.1 AFM and Nanoindenter Based Techniques

1.2.1.1 AFM Based Techniques for Tests in Bending Mode

AFM based techniques have been used extensively over the recent years to study the properties of nanowires in bending mode [10-14].

Cuenot et. al. [11] used resonant contact atomic force microscopy to measure the elastic modulus for silver and lead nanowires with diameters ranging from 30-250 nm. They used the shift in the resonant frequency of the AFM tip when contacted with the

nanowire (higher resonant frequency when in contact) which was then used to calculate the stiffness of the structure in contact.

Jing et. al. [10] in 2006 studied the behavior of silver nanowires using contact atomic force microscopy. Silver nanowires suspended in ethyl alcohol solution were dispersed on a silicon wafer with etched holes to obtain some nanowires suspended over these holes. A three point bending test was performed on these suspended nanowires using contact atomic force microscopy (Fig. 1.1). The ends of the nanowires over the etched holes were assumed to be fixed in the analysis.

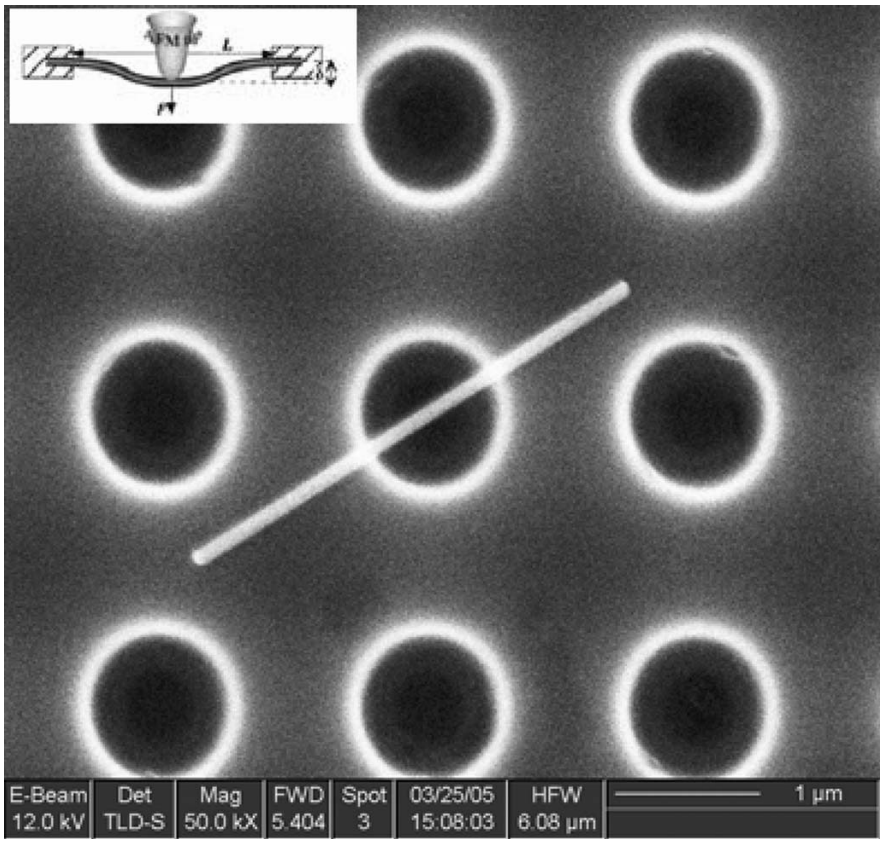

Figure 1.1: SEM image of a typical suspended nanowire (diameter 79 nm). Schematic diagram of a nanowire with midpoint deflected by an AFM tip is shown in the inset. (Courtesy Jing. et. al. [10])

Wu et. al. [12, 13] however argued that methods of placing nanowires over etched pores and consequently using contact atomic force microscopy may suffer from the complications of friction between nanowire and substrate and emphasized on clamping the nanowires at the edges of the trenches using electron beam induced Pt deposition (Fig. 1.2).

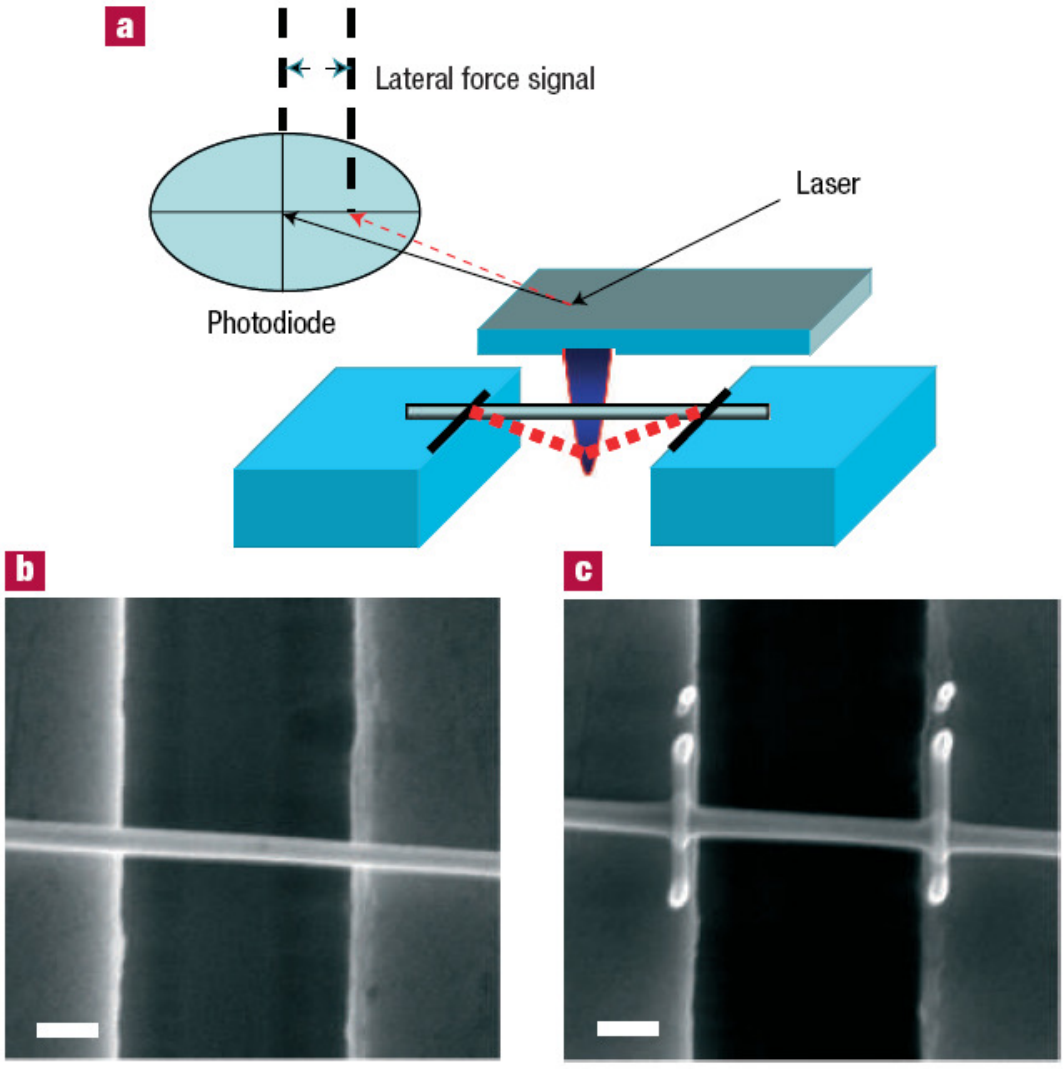

Figure 1.2: The bending test for nanowire mechanical measurements done by Wu et. al.[12]: (a) Schematic of fixed wire in a lateral bending test with an AFM tip. (b) SEM image of a 200-nm Au nanowire suspended on a trench. (c) SEM image of a Au nanowire mechanically fixed by electron-beam-induced deposition of Pt lines. The scale bars on both images are 500 nm. (Courtesy Wu et. al [12])

Ni et. al. [14] also used the three point bending testing using atomic force microscope to study the behavior of amorphous SiO_2 nanowires.

1.2.1.2 Nanoindenter Based Techniques for Uniaxial Testing

Uchic et. al. [17] in 2004 introduced a new approach to investigate the material properties of micron scale specimens. FIB (Focused Ion Beam) was used to mill cylindrical micron-scale samples into bulk crystal. These samples were then tested in compression mode using a flat punch tip in a nanoindenter.

This technique was used by Greer et. al. [18] in 2005 for uniaxial testing of gold nanopillars in compression mode (see Fig. 1.3). The nanoindentor module used has a theoretical displacement resolution of 0.0002 nm and a force resolution of 1 nN.

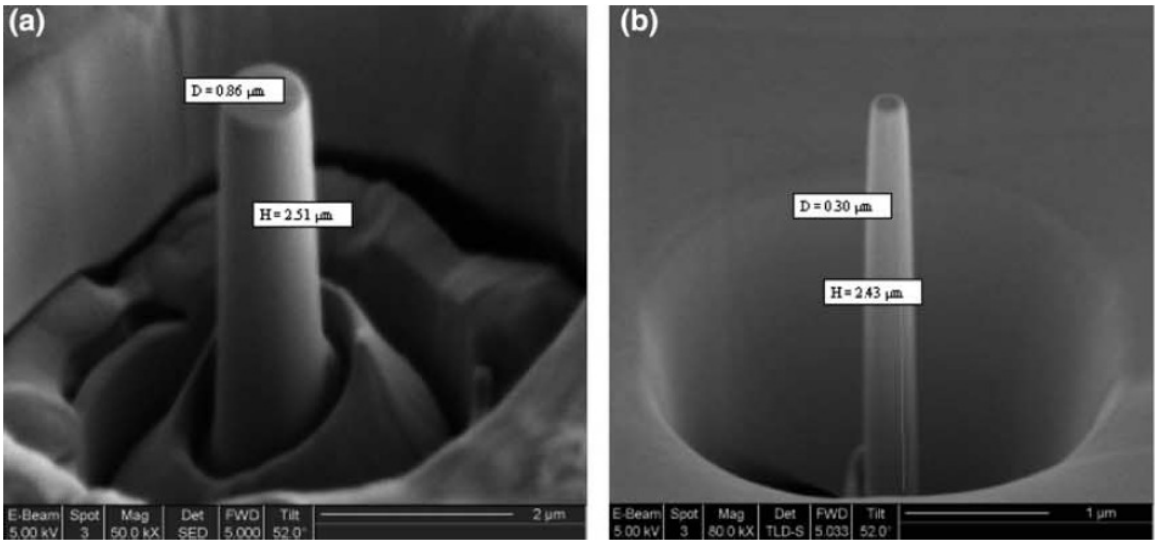

Figure 1.3: (a) FIB image of a 860 nm-diameter, 3.2 µm-tall <0 0 1> gold pillar; (b) FIB image of a 300 nm-diameter, 3.15 µm-tall <0 0 1> gold pillar, tested in compressive mode (Courtesy Greer et. al. [18])

Kim et. al. [19] in 2009 further extended the technique for uniaxial tensile testing of nanopillars (see Figs. 1.4 and 1.5). Bulk material was milled using FIB to form a dog

bone shaped tensile specimen. An equivalent nanoindentor grip was similarly milled using FIB to apply tensile loads to the specimen.

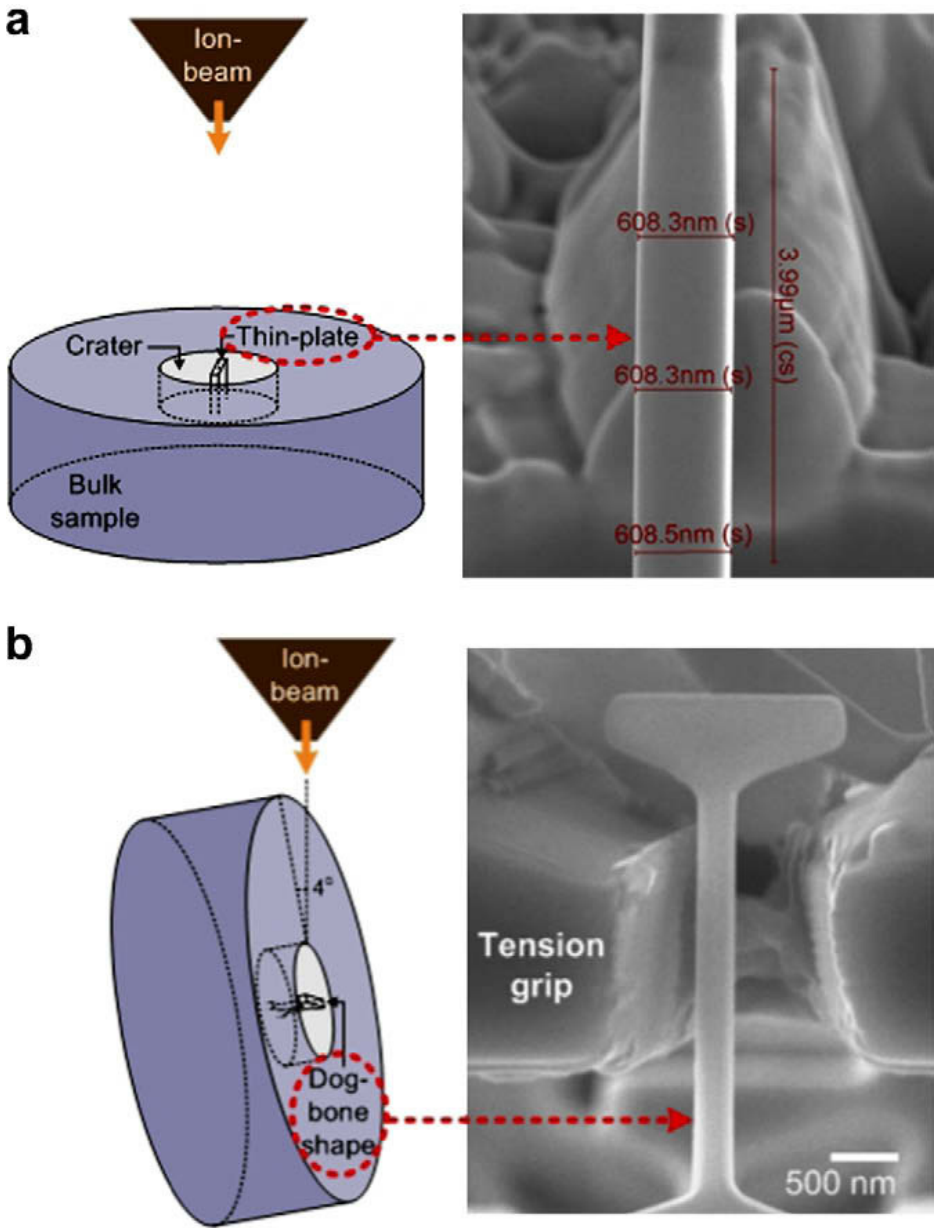

Figure 1.4: Procedure used by Kim et. al. [19] for making dog-bone-shaped tension sample: (a) side view of thin lamella and (b) tension sample. (Courtesy Kim et. al. [19])

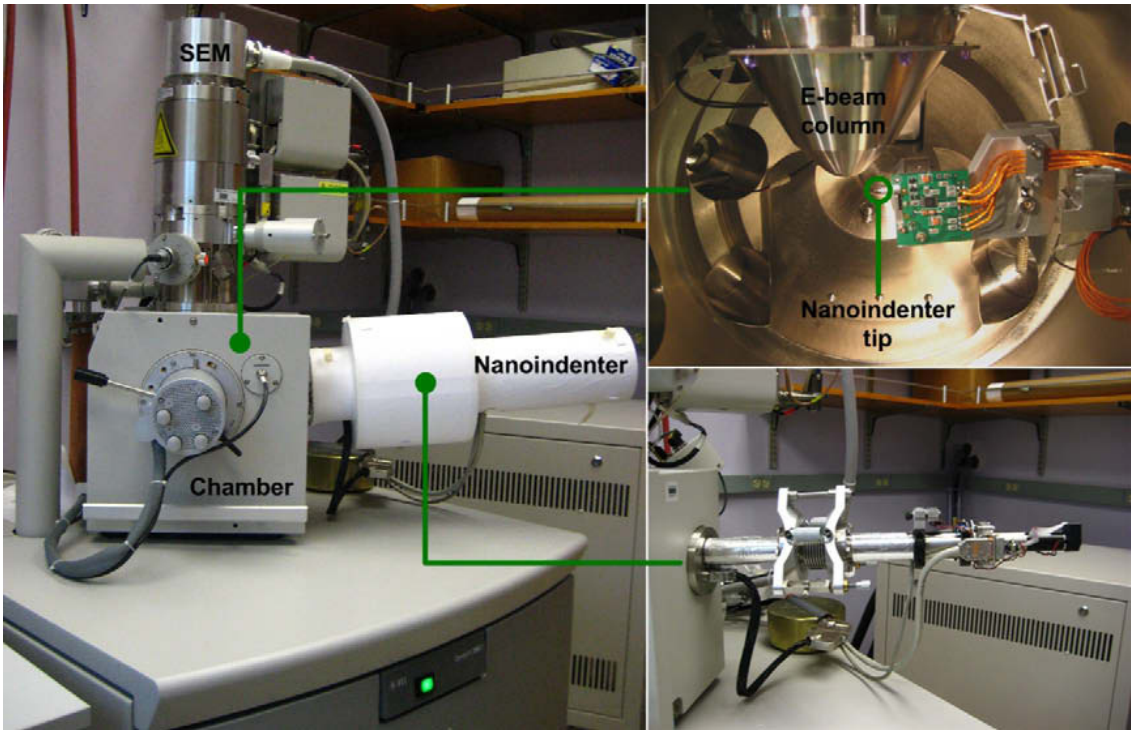

Figure 1.5: Pictures of the SEMentor (SEM + Nanoindenter) and the inside of chamber used by Kim et. al. [19]. (Courtesy Kim et. al. [19])

Recently Richter et. al. [20] used a nanoindenter for testing of Cu nanowhiskers in tensile mode (Fig. 1.6). E-beam assisted Pt deposition was used to grip the nanowhiskers.

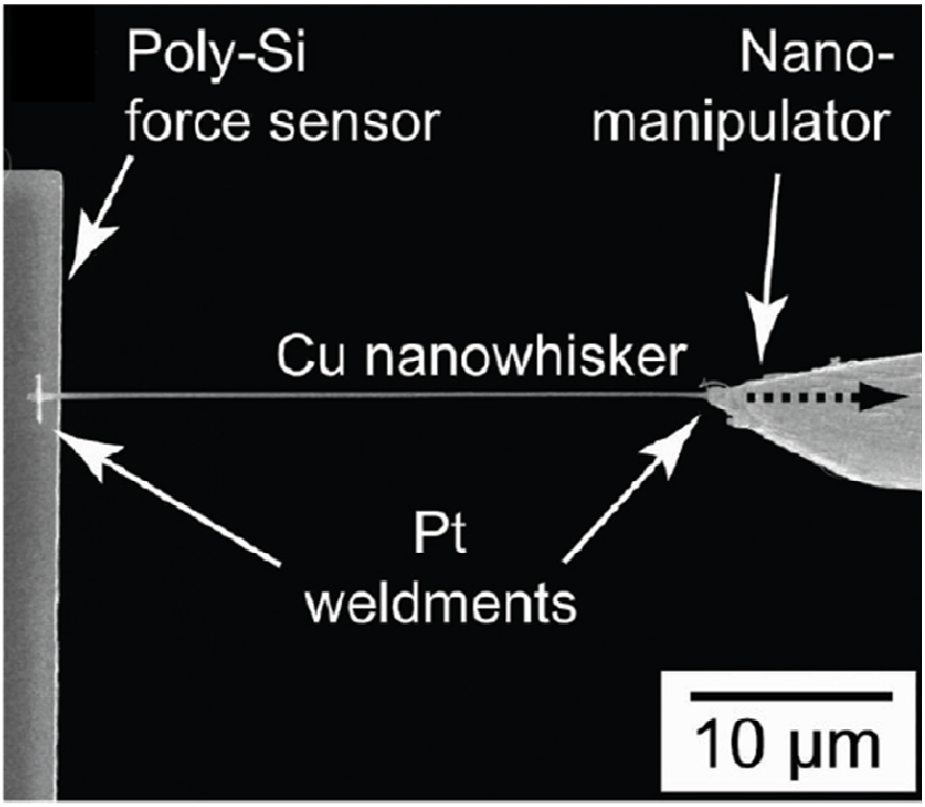

Figure 1.6: SEM micrograph of whisker mechanical testing configuration used by Richter et.al. [20]. (Courtesy Richter et. al. [20])

1.2.2 Integrated Nanoindenter - MEMS Based Techniques

Recently, Lu et. al. [21] used a novel technique with the integration of nanoindenter with MEMS based techniques. A MEMS device was used to convert the compressive force of a quantitative in situ SEM/TEM nanoindentor to tensile loading on a 1D nanostructure using a MEMS device (Fig. 1.7).

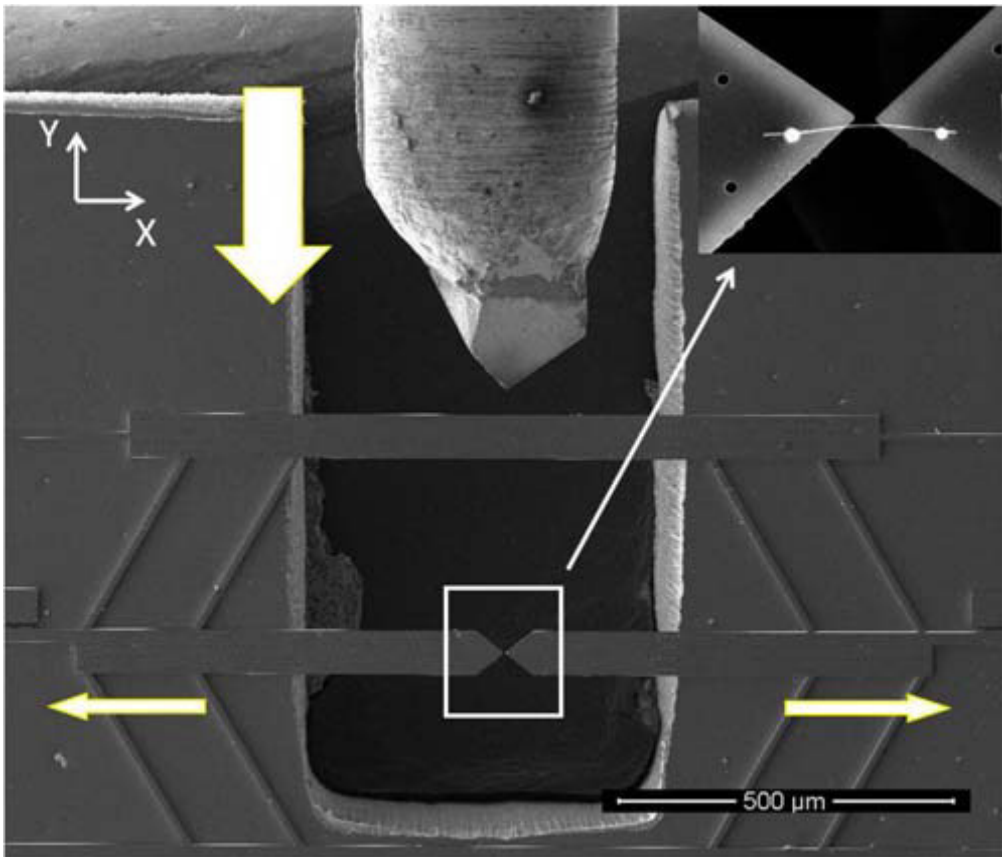

Figure 1.7: SEM image showing the geometry of the fabricated device and the nanoindenter tip. Arrows show the direction of movement of the top shuttle and sample stage shuttles upon load application. The inset shows a close up image of a mounted Ni nanowire sample (Courtesy Lu et. al. [21]).

A nanoindentor in a SEM/TEM was used to apply a vertical force (Y direction) on the top shuttle (Fig. 1.7). The vertical motion of the top shuttle is transformed into the horizontal (X direction) motion of the sample stage. The conversion factor which relates the force applied by the nanoindentor to the force acting on the sample was found using finite element analysis. However the process requires an iterative method to find the corrective parameters for the conversion factor based on the material to be tested. The authors suggested that the conversion factor for applied displacement can be obtained similarly or by direct imaging in the SEM. However this method relies heavily on finite element modeling and as the authors accept, a predetermined force conversion factor for samples

with relatively low Young's modulus would be inaccurate, an iterative procedure might be required.

Similar ideas of converting external compressive loading to tensile loading for specimen testing have been explored in the past for theta specimen development (Fig. 1.8). Quinn et. al. [22] suggested round or hexagonal rings compressed with a nanoindenter, thereby providing tensile loading to the specimen for testing of small scale materials.

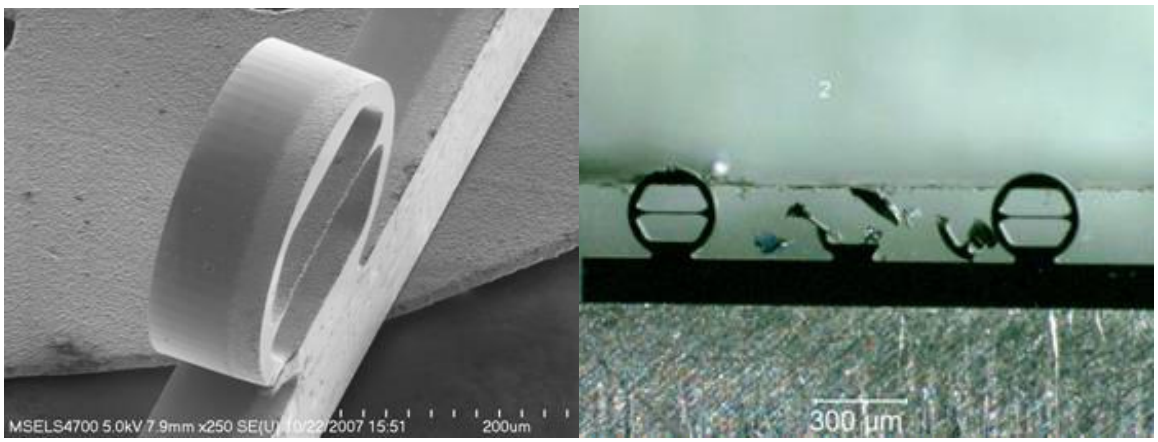

Figure 1.8: Left- shows a theta specimen, Right- a theta specimen being crushed due to excessive loading during testing*.

Previously, Haque et. al. [23] had also explored the idea of external actuation for a MEMS device for testing of thin films (see Fig. 1.9). A TEM straining gauge was used for actuation. The authors claimed a force resolution of 18.2 µN and a displacement resolution of 100 nm.

* Courtesy http://www.nist.gov/msel/ceramics/nanomechanical_properties/mems-and-nems-mechanical-reliability-measurements.cfm

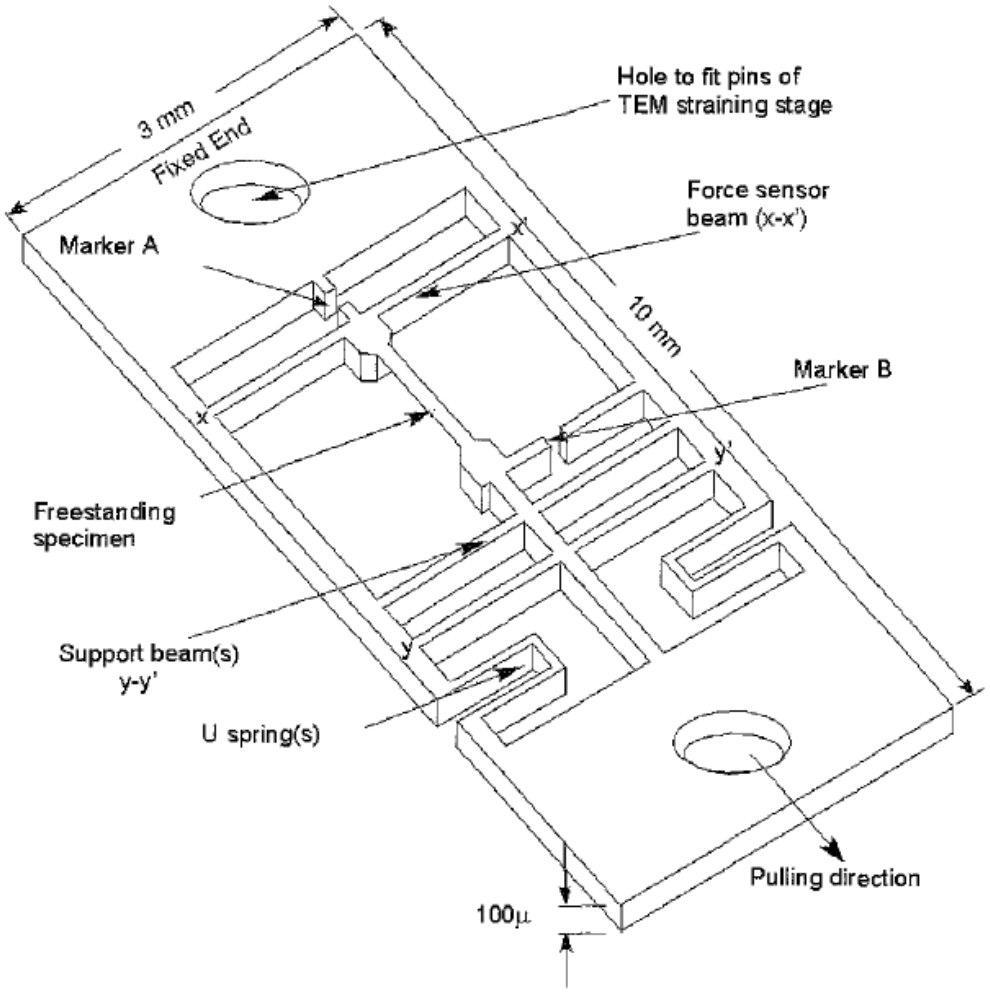

Figure 1.9: Schematic diagram of tensile testing chip used by Haque et. al. [23].

1.2.3 MEMS Based Techniques

MEMS based nanoscale testing systems include built in actuator systems and/or sensors as compared to methods discussed earlier (sections 1.2.1 and 1.2.2) in which the required loading for testing is provided externally. Recently, substantial research has been conducted in the development of MEMS based nanotensile testing systems due to various reasons. The compact size due to miniaturization makes them extremely suitable for

nanoscale testings. They can be used in various vacuum or environmental chambers as compared to nanoindentor/AFM based testing.

Broadly two types of actuator mechanisms have been actively researched in the past – electrostatic and thermal. Both have their own sets of advantages and disadvantages. Electrical actuators can be used for high frequency cyclic loading for fatigue testing of nanostructures unlike thermal actuators due to their relatively higher response time. However thermal actuators have the ability to apply much higher forces and displacements for the same actuator size as compared to electrostatic actuators. Furthermore electrostatic actuators typically require relatively high driving voltages for achieving reasonable actuation forces/deflections.

1.2.3.1 Electrostatic Actuation

Development of electrostatic actuators began on the principles of electrostatic force of attraction on the plates of a parallel plate capacitor (Fig. 1.10).

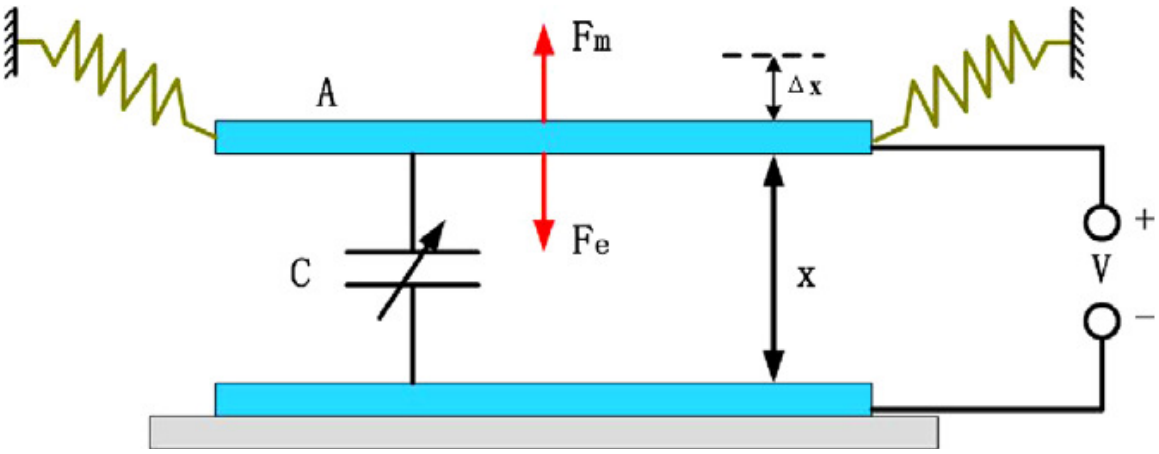

Figure 1.10: The traditional model of the variable parallel capacitor (Courtesy Zhang et. at. [24])

Several studies have been done on the stability and control of such electrostatic actuators [24-33]. However, theoretically, pull in of these plates occurs when the deflection of the

movable plate becomes one-third of the original air gap [25, 26]. Further, the instability and control issues of such parallel plate/beam based actuators led to the development of comb drive electrostatic actuators for nanoscale testing devices.

Naraghi et. al. [31] used an electrostatic comb drive actuator based MEMS device for testing nanofibers (Fig. 1.11). Application of bias voltage across the actuator causes attractive forces on the two sets of a comb drive resulting in the required force/motion. The authors reported a maximum achieved load of 30 μN for the optimized design.

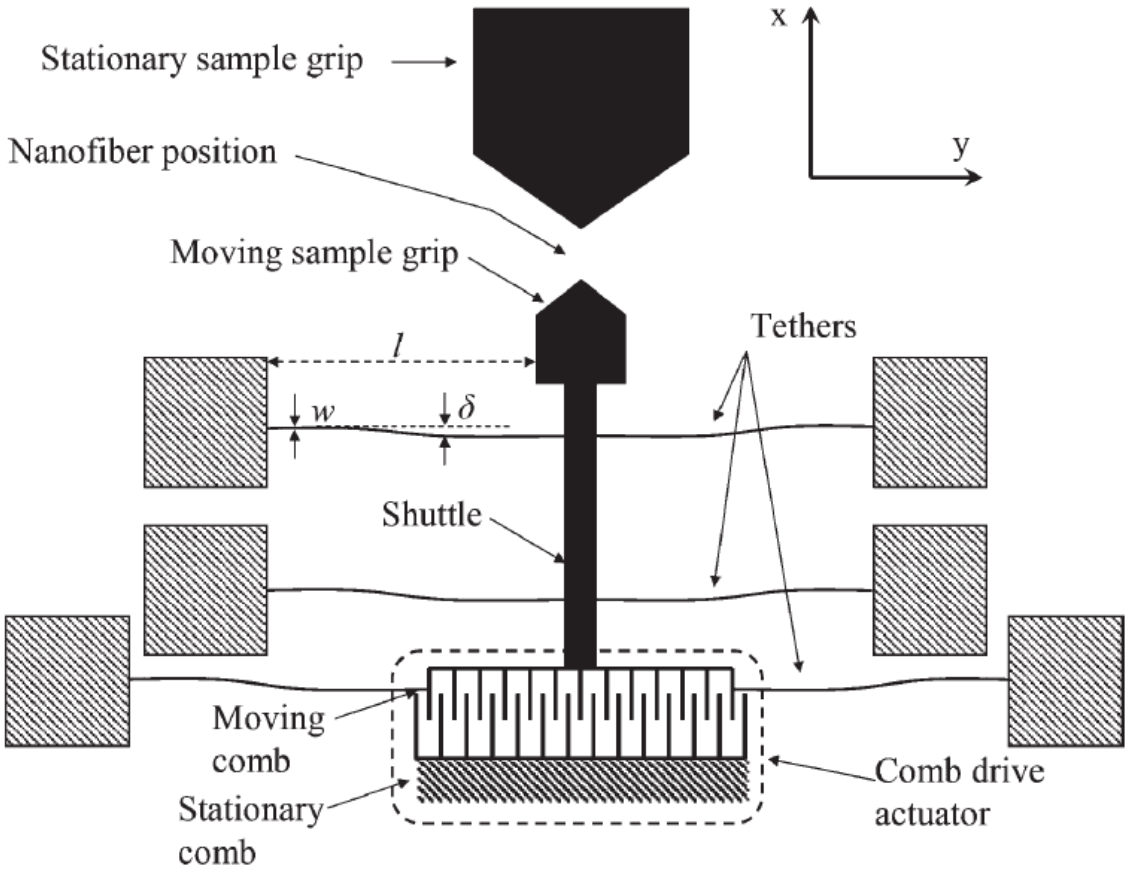

Figure 1.11: Schematic of a MEMS nanofiber testing platform with a comb drive actuator used by Naraghi et. al. [31].

Kiuchi et. al. [32] in 2007, also used an electrostatic comb drive actuator based MEMS device (Fig. 1.12) to study the mechanical behavior of carbon nanowires

(diameters ranging from 90 to 150 nm) deposited by FIB-CVD at room temperature. The actuator consisted of 1000, 3000 and 5000 sets of comb drives for different designs.

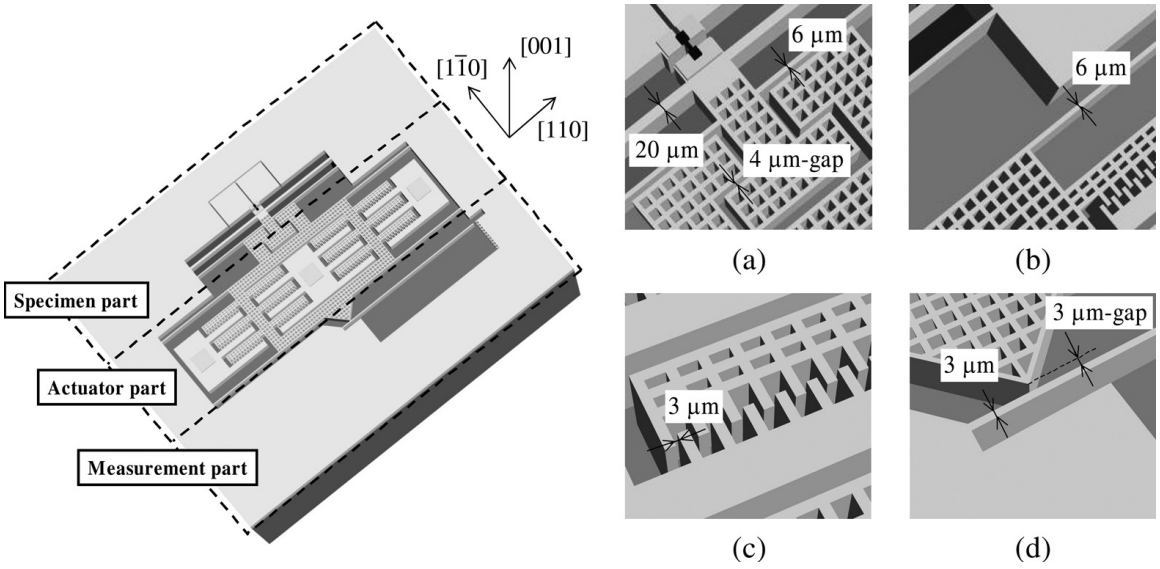

Figure 1.12: Schematic of the design layout for an EANAT. Details of: (a) specimen part suspended by a 20- and a 6-micron-wide beam; (b) a 6-micron-wide suspended beam of the actuator part; (c) electrostatic comb drive actuators; and (d) fixed end of cantilever of the measurement part. (Courtesy Kiuchi et. al. [32])

Sensing consisted of a cantilever beam which acted as a lever motion amplification system (Fig. 1.13). The motion of the actuator is amplified at the farther end of the beam which is then measured optically. An amplification factor of 91 was obtained for the designed cantilever. This amplification factor translated the 0.398 µm resolution of the CCD camera/microscope system at the farther end of the cantilever to 4.37 nm resolution for tensile displacements at the actuator. Failure of a nanowire resulted in a change in stiffness of the system and consequently a change in the slope of the load displacement curve. The authors claim a minimum resolution of 123 nN for the applied tensile load.

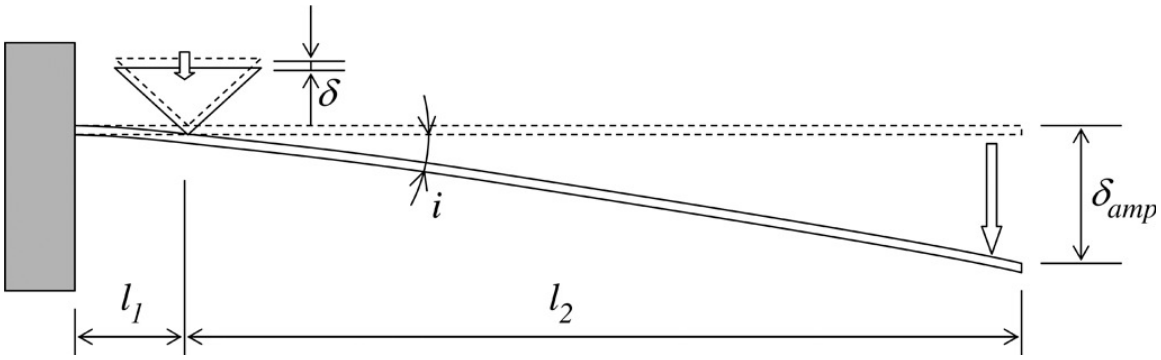

Figure 1.13: Schematic diagram of the cantilever used as a lever motion amplification system and located in the measurement part. (Courtesy Kiuchi et. al. [32])

Electrostatic comb drive actuators have shown the problem of pull in voltages, specifically highlighted at the end comb drives, which show a lateral pull in behavior at higher applied voltages due to unsymmetrical lateral force condition. Chen et. al. [33] suggested usage of thick end comb drives to mitigate this problem (see Figs. 1.14 and 1.15).

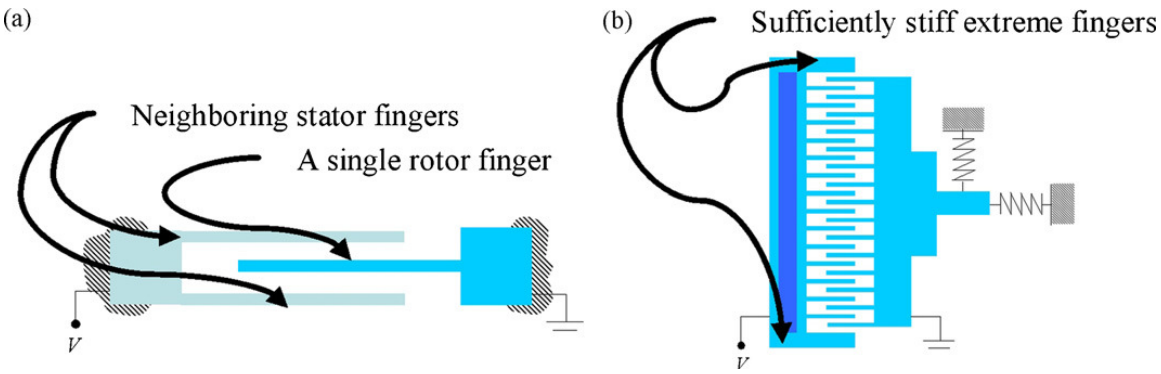

Figure 1.14: (a) A single rotor finger between two stator fingers, and (b) a comb-drive actuator with the sufficiently stiff first and last fingers. (Courtesy Chen et. al. [33])

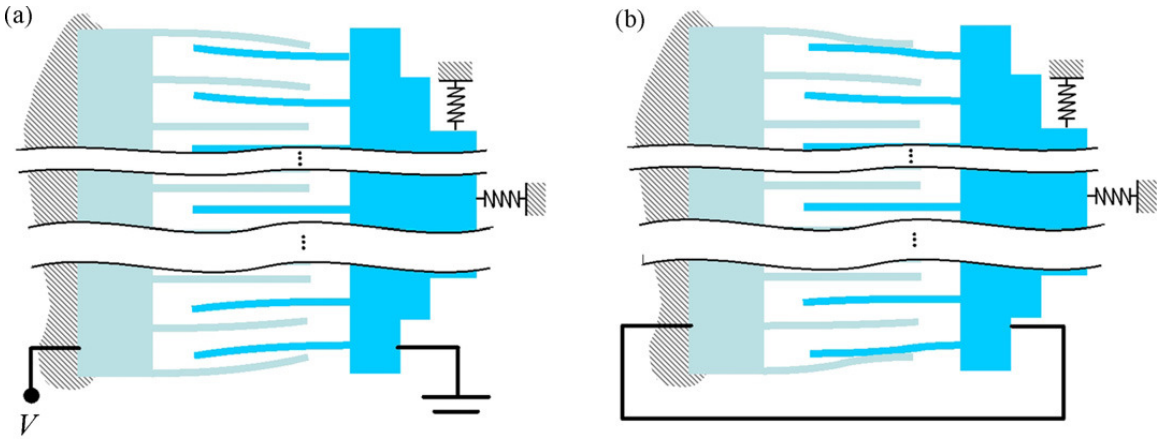

Figure 1.15: (a) Fingers are bent by the transverse electrostatic force when a comb-finger array is at the equilibrium state, and (b) some of the fingers contact to each other and lead to short circuit after side pull-in of individual finger happens. (Courtesy Chen et. al. [33])

1.2.3.2 Thermal Actuation

Thermal actuators work on the basic principle of Joule heating. When a potential difference is applied across conducting beams, current flow through it gives rise to Joule heating which in turn causes thermal expansion of the mentioned beams. This thermal expansion forms the principle for actuation and has been used extensively over the years for the development of various thermally actuated MEMS based systems [34-48].

Lu et. al. [44] in 2004 used this design principle for the development of thermally actuated MEMS devices and reported a deflection of 4 microns for an applied input power of 600mW for the designed devices (Fig. 1.16). The design involved a set of horizontal beams experiencing horizontal outward motion due to thermal expansion when a current flows through them (See Fig. 1.16 (b)). A pair of V-shaped beams attached to the horizontal beams transform the horizontal motion due to the thermal expansion to vertical deflection for nanoscale testing.

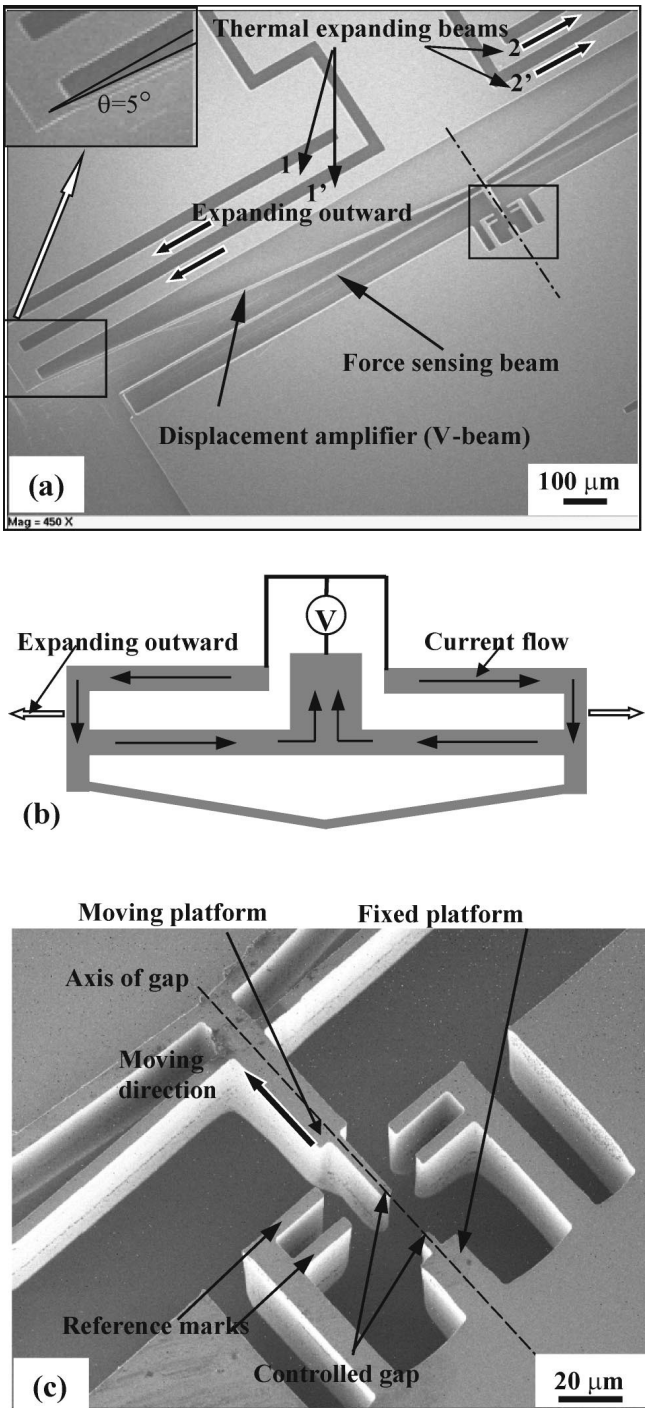

Figure 1.16: (a) SEM (Hitachi S-4500) image of the device. The thermal expansion beams 1-1' and 2-2', indicated by the arrows, are symmetric relative to the center line (dashed line) of the device. Beams 1 and 2 are 970 μm long, while beams 18 and 28 are 1000 μm long. The width of the beams is 50 μm. The thickness of the device Si layer is 130 μm. The upper left-hand side inset is a higher magnification image of the connection between the thermal expansion beams and V-shaped beams. (b) The current flow during actuation. (c) The magnified central gap region. (Courtesy Lu et. al. [44])

Varona et. al. [46] investigated another possible design for thermal actuators. It consisted of sets of symmetrical V-shaped beams anchored at both ends, which get heated due to a current flow when a potential difference is applied across them. Joule heating results in thermal expansion of beams which in turn due to symmetry, results in deflection along the symmetric axis (Figs. 1.17 and 1.18).

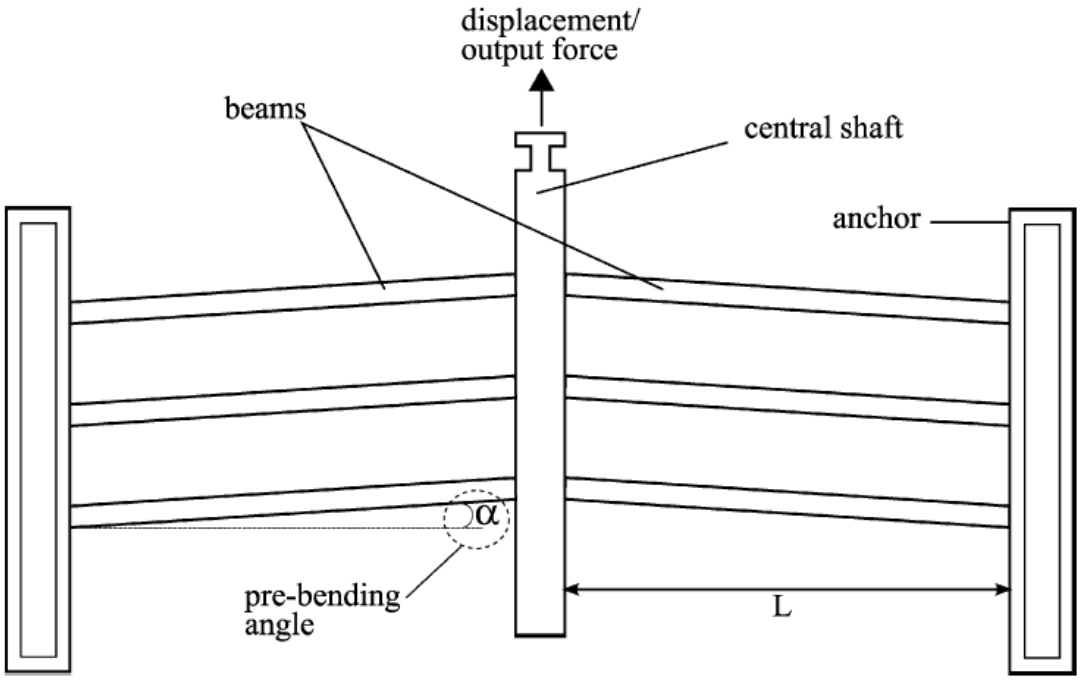

Figure 1.17: Another design for a thermal actuator. (Courtesy Varona et. al. [46])

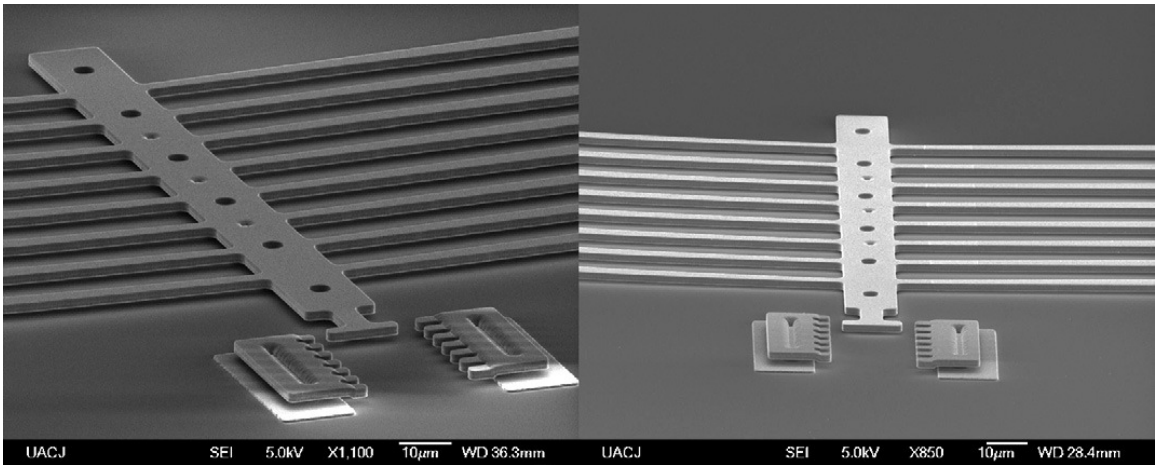

Figure 1.18: SEM images of the thermal actuator fabricated by Varona et. al. [46]

Similar designs of thermal actuators have been used extensively by several researchers for the development of thermally actuated MEMS based nanoscale testing devices [46-48]. However several of the above discussed devices lacked a well developed high precision capability for independent load-deformation measurements for nanoscale testing.

Zhu et. al. [47, 48] used a similar actuator (Fig. 1.19) with the addition of an inbuilt capacitance based sensing module for precise load measurements. The authors addressed the design and optimization of such MEMS devices and reported the device being capable of providing tens of milli-Newton force and a few microns deflection depending on the design.

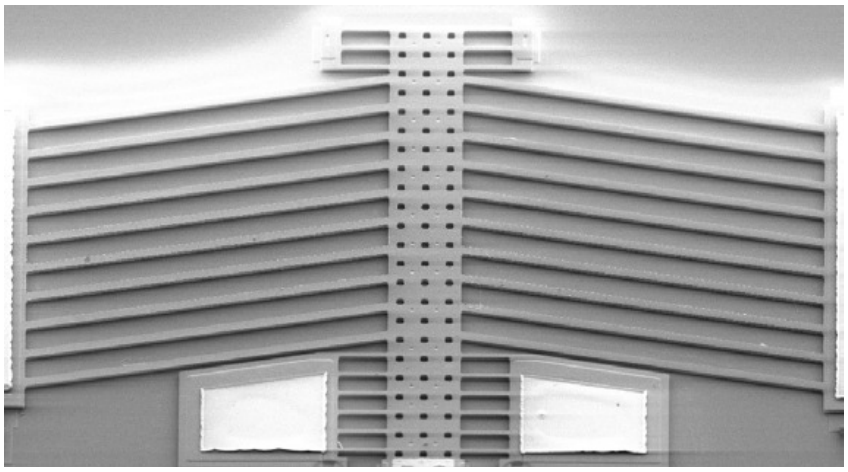

(a)

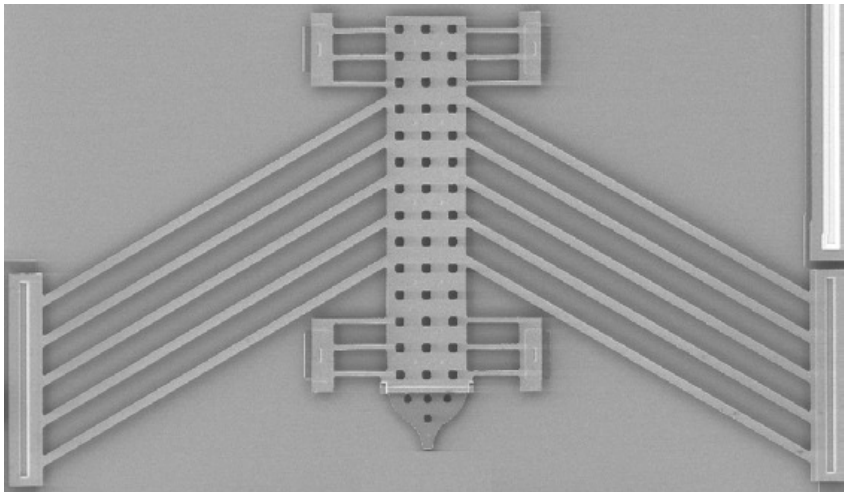

(b)

Figure 1.19: Two types of thermal actuators for used by Zhu et. al. [47, 48] for testing various types of nanostructures: (a) ten pairs of thermal beams with a beam angle of 10 degrees and (b) five pairs of thermal beams with a beam angle of 30 degrees. (Courtesy Zhu et. al. [47, 48])

The MEMS based testing system consisted of a thermal actuator and a capacitive load sensor separated by a specimen gap (Fig. 1.20). The authors performed an extensive study of these devices using multi-physics simulations. The load applied on the specimen was measured using the deflection of the load sensor with a known stiffness. The stiffness of the load sensor was determined by finite element analysis which reportedly was in good agreement with the stiffness determined by resonating the structure. The

authors claim a maximum possible displacement resolution of 3 nm and a force resolution of 145 nN using these devices.

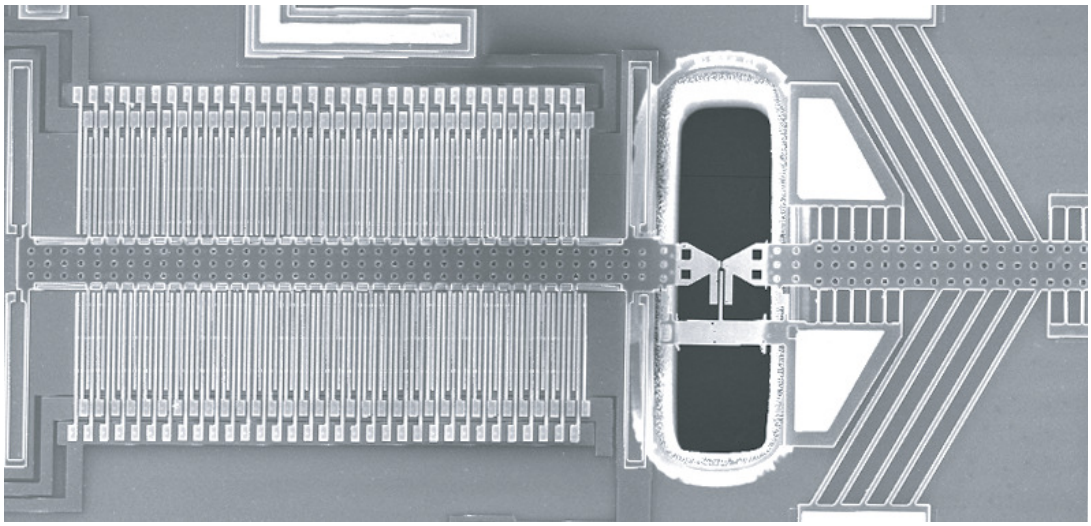

Figure 1.20: MEMS based nanoscale testing device used by Zhu et. al. [47, 48]. (Courtesy Zhu et. al. [47, 48])

1.3 Discussion of Nanoscale Testing Methodologies

AFM based techniques have been used extensively in the past for determination of mechanical properties of nanoscale materials. However there are certain limitations for nanoscale testing using such methods. Most of these techniques are applicable for bending tests as compared to more desirable tensile loading tests where the specimens are exposed to a uniform tensile load across the cross-section as compared to bending tests. Another limitation imposed due to the testing methodology is the inability to perform such tests in various controlled environments and consequently the environmental effects on materials cannot be directly determined.

Furthermore most of the AFM methods involve positioning a nanowire across a pore or a trench. In general these methods suffer from the complication involving friction

effects between nanowire and substrate. Use of material deposition to clamp the nanowire can lead to leakage of pinning material causing error in the length of the nanowire and consequently in the measured elastic modulus which shows a cubic length dependency further amplifying the errors. Also despite the high force and displacement resolution of AFM, the errors in the measurements of nanowire dimensions (4%) are amplified and result in much higher errors in the calculated Young's modulus values (40%) [10].

For tests involving determination of yield stress or strength using nanoindenter/AFM in bending mode, it may be difficult to establish whether the failure is due to the wire or the contact between the tip and nanowire and hence causes reliability concerns regarding the observed properties.

Nanoindentor based methods for uniaxial tensile testing promise much higher resolution as compared to MEMS based sensing. However the major disadvantage still remains the inability to study the environmental effects on material properties of nanostructures (similar to AFM based techniques). Furthermore these methods are not suitable for fatigue studies.

Hence the requirement of MEMS based system for nanoscale testing gains further prominence. Due to the compact size and inbuilt actuation mechanism, such devices can be used for testing in various environments. Further, several of the TEM/AFM based methods and even certain MEMS based methods discussed lack the ability for independent simultaneous load-displacement capability for nanoscale testing. This emphasizes the incorporation of a sensing mechanism in the MEMS devices for precise force and displacement measurements which would also reduce the use of expensive equipment time (SEM/TEM) during testing itself.

Table 1.1 gives a brief comparison of the aforementioned categories of nanoscale testing techniques.

Table 1.1: Comparison of state of the art nanoscale testing techniques.

Technique	Mode	Resolution	Pros	Cons
AFM	Bending	G ~ 40%	------	Tests not possible in environmental chambers
Nanoindenter	Tensile / Bending	Disp. < .01nm Force ~ 1nN	High resolution	Tests possible only in SEM/TEM chambers
MEMS	Tensile	Disp. ~ 5nm Force ~150nN	Tests possible in environmental chambers.	Lower resolution as compared to nanoindenter.

1.4 Motivation for Study

With the rapidly developing technologies, nanoscale materials have shown promising applications (see Section 1.1) in various fields like nanoelectronics and nanoelectromechanical systems (NEMS). However for any such applications it becomes essential to understand the behavior of materials at nanoscales. The strength of nanoscale monocrystalline metals has been shown to be significantly higher than their bulk counterparts [10, 11, 15, 16]. Furthermore several interesting properties of materials are highlighted at the nanoscale [2, 3, 4, 8, 10, 11]. Surface effects like surface tension, oxidation layers, surface roughness etc. play a much more significant role due to high surface to volume ratio [10-16], which modifies the material behavior resulting in a size effect on material properties [15]. Due to the high unpredictability and absence of sufficient understanding of such effects, it is not always possible to extrapolate nanoscale behavior from bulk properties. Hence the requirement of a testing system to study these

material properties gains much more prominence. Even though several methodologies have been researched in the recent past for the development of such techniques, the capability of nanoscale tensile testing still remains a challenge. The methods developed lack significant precision in the ability to perform independent load-displacement measurements simultaneously and at various environments. The study aims at the development and characterization of a MEMS based nanotensile tester and a proper methodology for testing of 1-D nanostructures and consequently use these devices for investigating nanoscale material behavior.

CHAPTER 2

MEMS NANOTENSILE TESTER: OPERATION AND CHARACTERIZATION

This chapter deals with the development and extensive characterization of a MEMS thermal nanotensile tester (see Fig. 2.1) for testing of 1-D nanostructures in tensile mode. The devices developed involve thermal actuation to provide tensile loading (refer to Chapter 1 for various actuation mechanisms) to the specimen. The sensing mode involves a capacitive load sensor integrated in the MEMS device. Different designs of the MEMS Nanotensile tester developed are discussed next.

2.1 Principle of Operation

The MEMS nanotensile tester primarily consists of three units:

1. Actuator (thermal) with heat sink
2. Nanowire gap
3. Load Sensor (capacitive sensing)

The various units of the MEMS nanotensile tester are shown in Fig. 2.2.

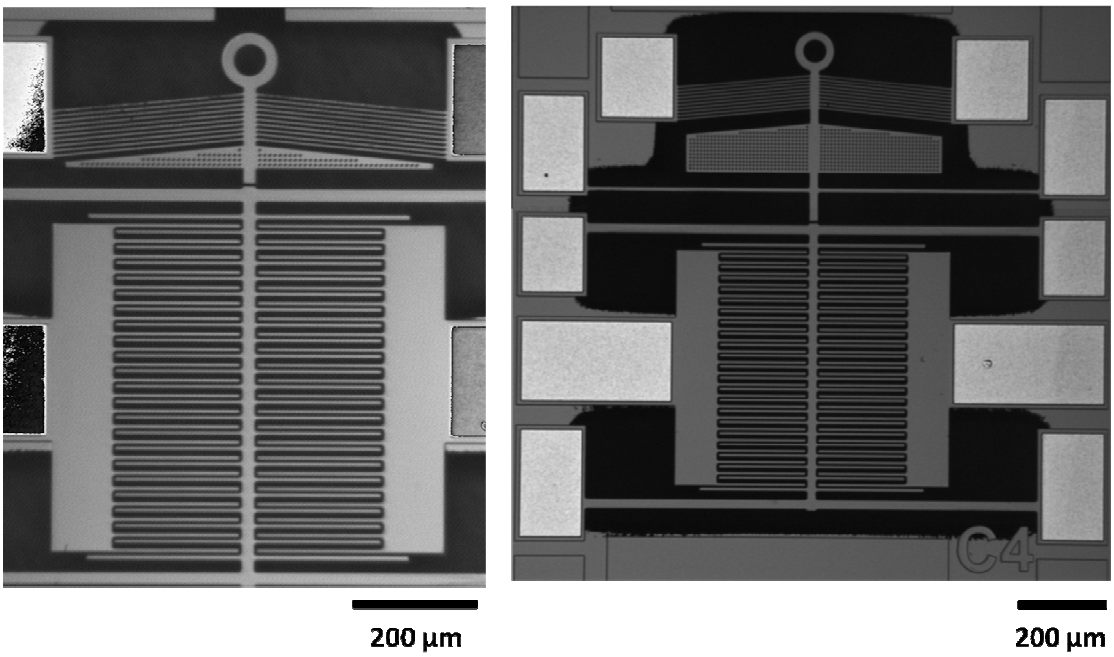

Figure 2.1: Optical images of MEMS Nanotensile tester – two different designs were developed and studied (Left: SOIMUMPs24, Right: SOIMUMPs27).

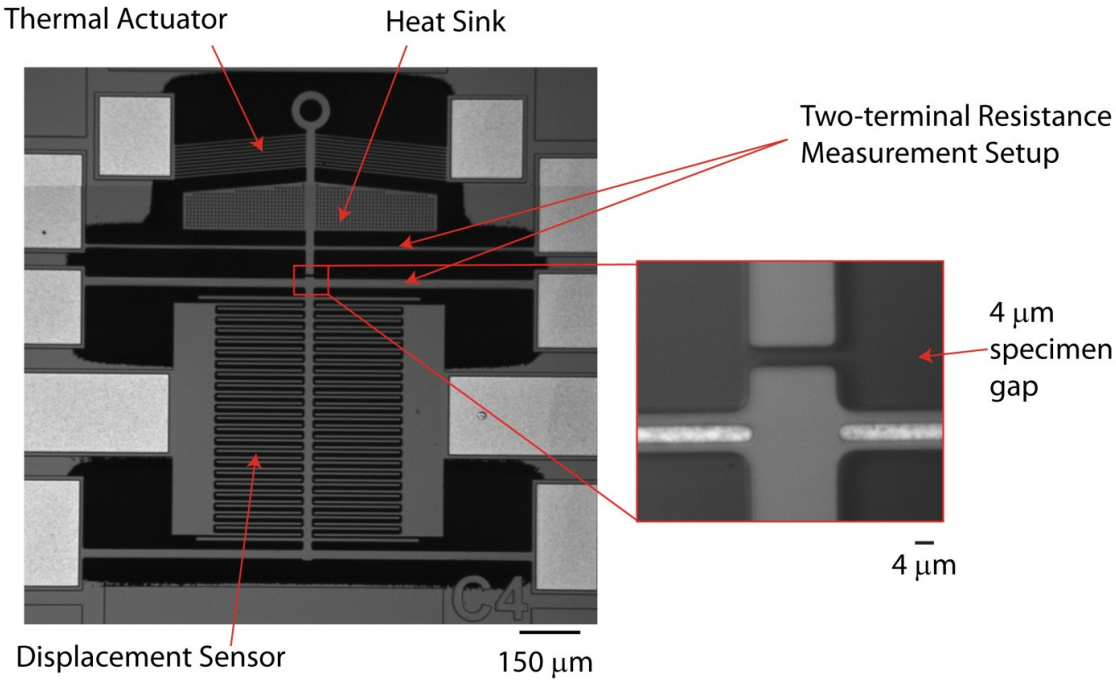

Figure 2.2: Specimen gap and the various parts of the MEMS nanotensile tester (SOIMUMPs27).

2.1.1 Actuator

The thermal actuator provides the necessary loading for tensile testing of the nano-specimens. A potential difference applied across the V-shaped symmetric actuator beams (Fig. 2.3), causes a current to flow through the actuator. This results in a temperature increase in the actuator beams due to Joule heating, which in turn causes the thermal expansion of these beams. Consequently a net displacement of the actuator is obtained (due to symmetry) leading to tensile loading on the specimen. The thermal actuator is capable of providing very large tensile loads (typical value - 400 μN) to the specimen placed across the specimen gap (Fig. 2.2).

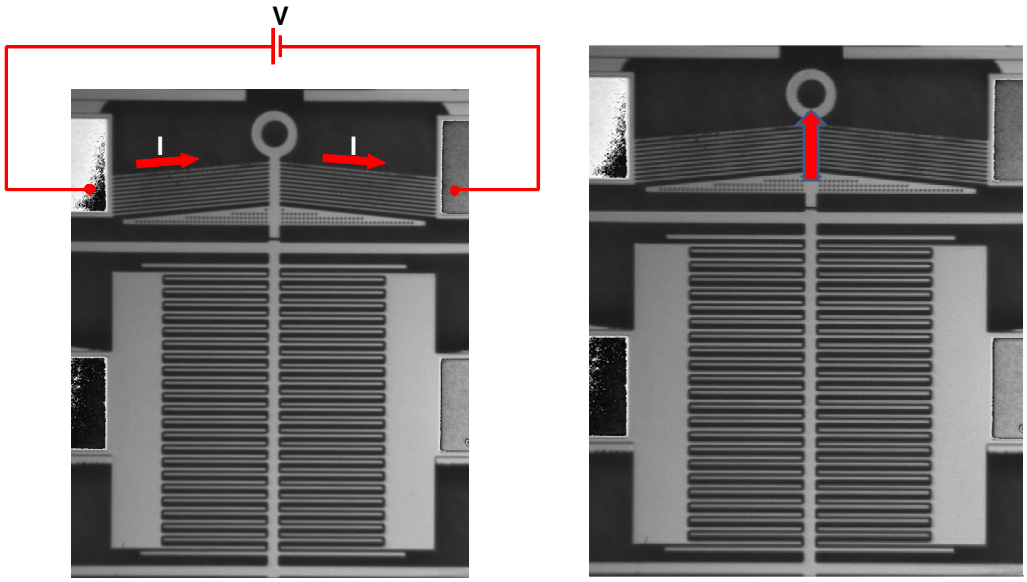

(a) (b)

Figure 2.3: Illustration of the principle of operation for the thermal actuator (design shown in the figure is SOIMUMPs24) (a) Applied potential difference (V) resulting in a current flow through the V-shaped actuator beams (b) Deflection direction of the actuator in the device plane due to thermal expansion.

2.1.2 Specimen Gap

A 4 micron gap (see Figs. 2.2) separating the actuator and load sensor is provided for the placement of nanostructures. The specimen is clamped on both sides of the gap using Pt deposition. The manipulation and placement procedure will be discussed in Chapter 3.

2.1.3 Load Sensor and Capacitive Sensing

The primary function of the load sensor is to measure the applied force on the specimen being tested. The force applied on the sample and consequently stress is determined by the deflection of the load sensor with a known stiffness (four stiffness beams that contribute to the load sensor stiffness are shown in Fig. 2.4).

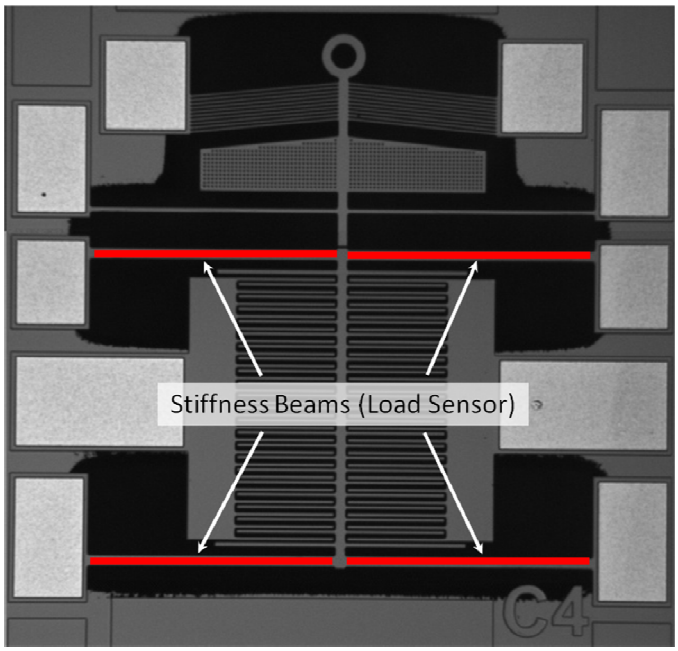

Figure 2.4: Optical image of the four stiffness beams contributing to the load sensor stiffness.

The load sensor consists of several pairs of comb-like structures which act like parallel plate capacitors and hence contribute to the capacitance of the load sensor. This load sensor capacitance depends on the gap (D) between these combs (see Fig. 2.5). The deflection of the load sensor in the vertically upward direction (refer Fig. 2.5) due to the applied force, causes a reduction in the gap (D) between these combs. Since the capacitance for a parallel plate capacitor varies inversely with the gap between the capacitor plates, this results in an increase in the load sensor capacitance. This capacitance change is measured and used to determine the load sensor deflection and consequently the applied force and specimen elongation (measured as the difference of actuator and load sensor deflections).

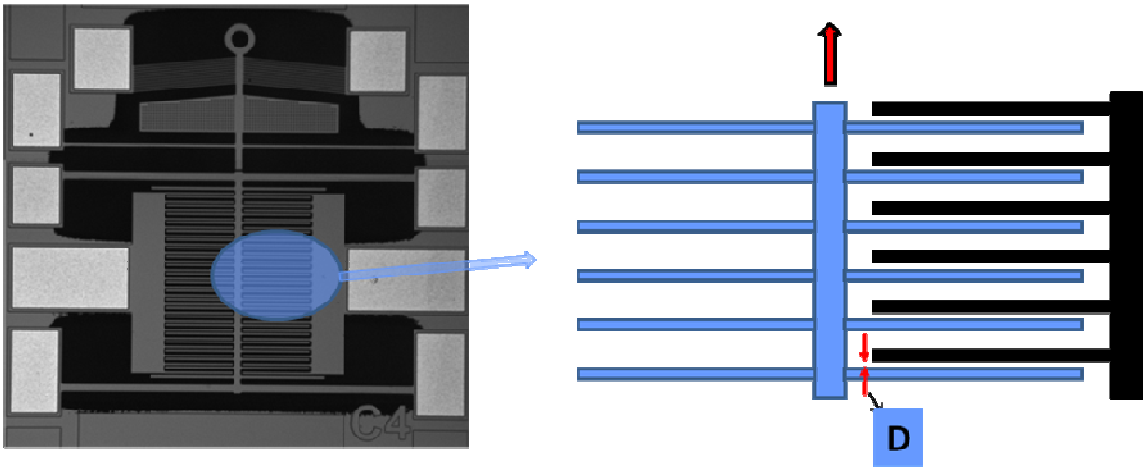

Figure 2.5: Illustration of the sensing module for the device. Deflection of the load sensor causes a change in capacitance of the parallel plate capacitor which is measured using an external circuit.

The capacitance for the load sensor is given by

$$C = k\varepsilon_0 nA\left(\frac{1}{d_1 - x} + \frac{1}{d_2 + x}\right)$$

Where ε_0=8.854x10^{-12} F/m is the permittivity of free space, k is the relative permittivity of the dielectric material (k~1 for air), A is the overlapping area of a comb structure, n is

the number of comb structures, d_1 and d_2 are the initial gaps between the comb structure (d_1 = 4 µm, d_2 = 9 µm), and x is the deflection of the load sensor. The capacitance change for change in gap (x) i.e. load sensor deflection has been shown in Fig. 2.6 (for one side sensor only).

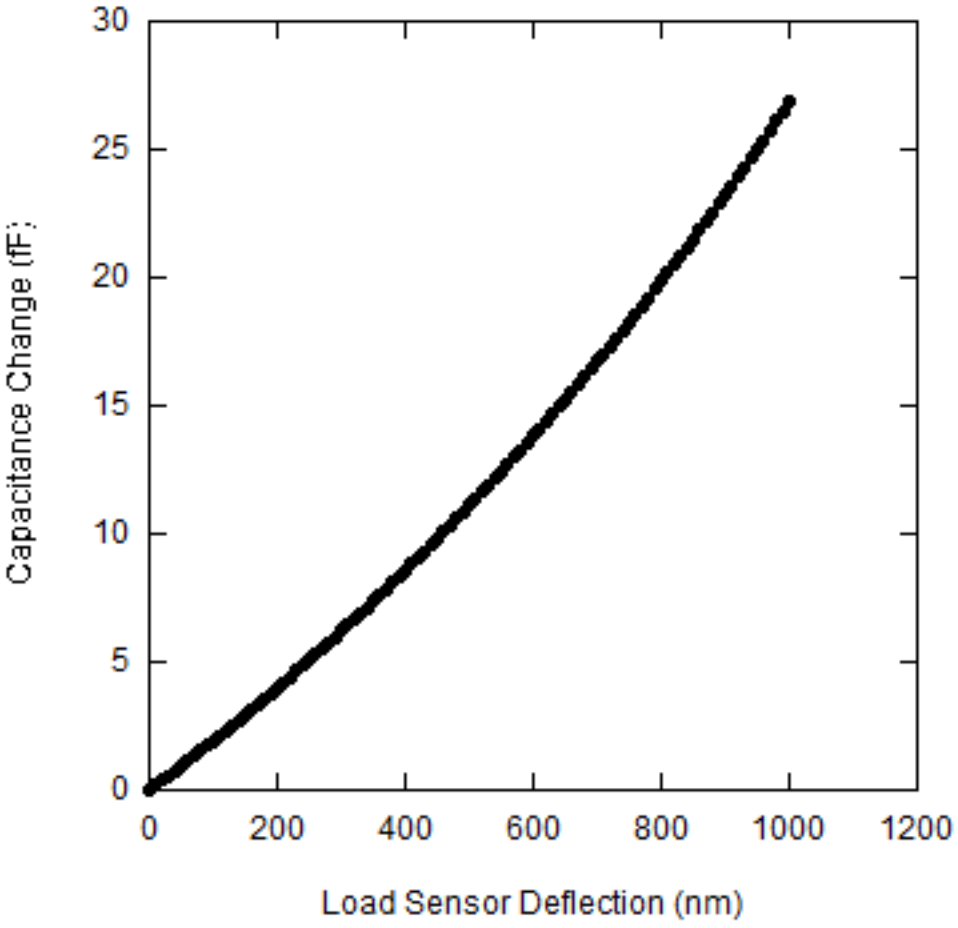

Figure 2.6: Expected capacitance change variation with load sensor deflection for the developed devices (only one side of sensor was used for the calculations).

2.2 Governing Equations

The governing equations of the nano-tensile testers are derived based on the lumped mechanical model shown in Fig. 2.7:

$$X_A = X_S + X_{LS} \tag{2.1}$$

$$F = K_{LS}X_{LS} = K_S X_S \tag{2.2}$$

Where X_A is the actuator deflection, X_S is the elongation of the specimen, X_{LS} is the deflection of the load sensor, F is the force applied on the specimen and the load sensor, K_{LS} is the load sensor stiffness and X_S is the specimen stiffness.

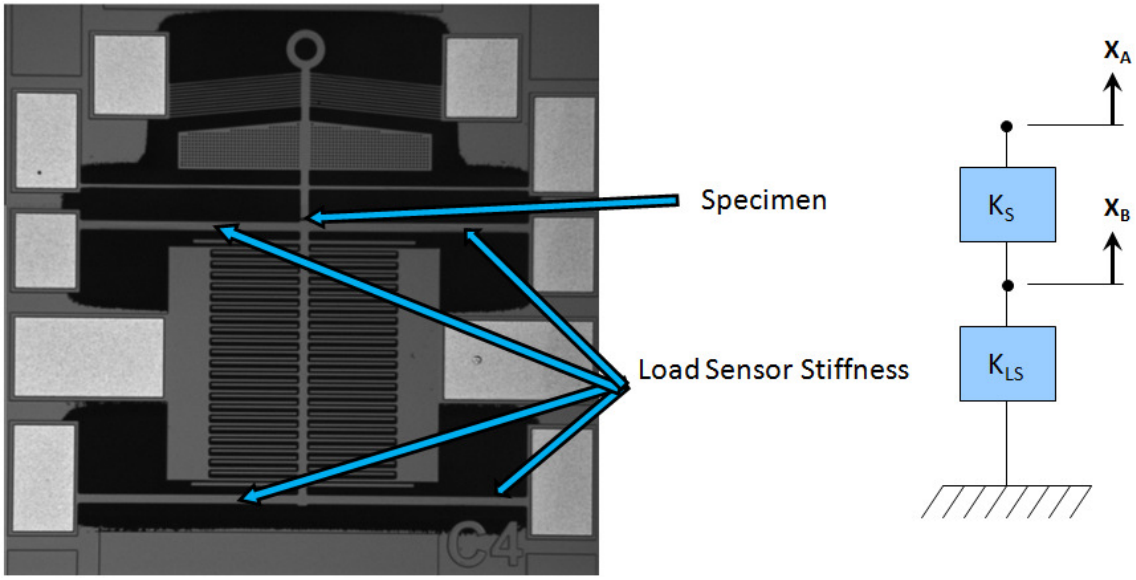

Figure 2.7: Illustration of the lumped mechanical model of the MEMS nanotensile tester.

A proper tensile test consists of measuring the elongation of the specimen (X_S) and the force applied ($K_S X_S$) throughout the test. The area of the nanowire (A_S) can be measured to calculate the applied stress ($K_S X_S/A_S$). The thermal actuator has a much higher stiffness (see Section 2.8) as compared to the load sensor and imposes a fixed deflection (*typical values may lie between 0-1 micron*) based on the applied voltage. The

stiffness of the load sensor (K_{LS}) can be determined using finite element analysis. In a typical tensile test, X_A is known (for a particular applied voltage X_A can be obtained using optical calibration) and X_{LS} is measured using capacitive sensing. X_S and $K_S X_S$ can then be calculated using eqs. (2.1) and (2.2). This would provide the force and consequently the applied stress. The elongation in the specimen (and consequently the strain) can be calculated by the difference in actuator and load sensor deflections (X_A-X_{LS}).

2.3 Device Geometry and Fabrication

The primary structural layer for the MEMS devices consists of 10 micron thick monocrystalline doped silicon and forms the various components of the nanotensile tester. Two designs (SOIMUMPs24 and SOIMUMPs27) were used. The load sensor and the thermal actuator beams are identical for both designs. However the SOIMUMPs27 consists of a larger heat sink (see Fig. 2.8) as well as an extra set of beams for two point resistance measurements across the specimen (Fig. 2.2).

The thermal actuator consists of 10 pairs of beams inclined at 5 degrees. This angle determines the net deflection of the actuator due to the thermal expansion of the beams. The heat sink (Fig. 2.2) is located between the actuator beams and the specimen gap. The heat sink is designed to minimize the temperature increase of the structural layer near the specimen.

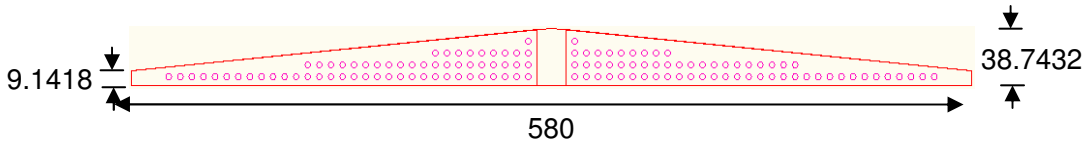

(a) Heat sink for SOIMUMPs24

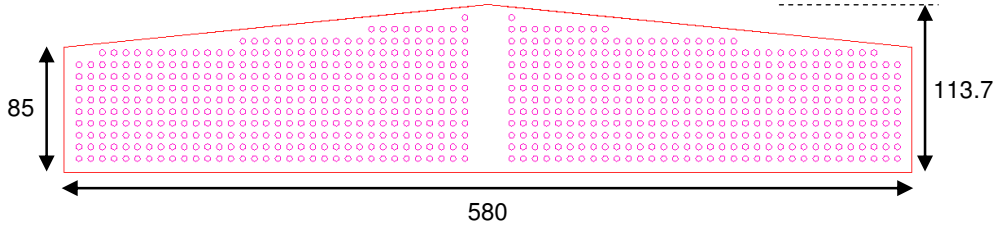

(b) Heat sink for SOIMUMPs27

Figure 2.8: Dimensions of the heat sink (all dimensions in microns).

The four stiffness beams (Fig. 2.4) contribute to the stiffness of the load sensor. Three different types of stiffness beams with widths 4, 9 and 21 microns, constituting stiffness of 3.4, 38.8 and 480.8 N/m respectively (see Section 2.8) were fabricated (for both SOIMUMPs24 and SOIMUMPs27). For capacitive sensing, the load sensor consists of 22 pairs of combs on each side of the symmetry axis. These combs act as parallel plate capacitors. However the combs are offset by 2.5 microns which increases the sensitivity of the capacitance measurements for small deflections.

Some devices of each design were fabricated such that no gap was provided for the specimens between the actuator and the load sensor i.e. the actuator and load sensor are structurally connected for such devices. In this case, all the deflection provided by the actuator goes to the load sensor. Such devices are termed as Calibration devices throughout the discussion. In some devices epoxy glue was applied on the specimen gap so as to structurally connect the actuator to the load sensor (Fig. 2.9). However due to the non conductive nature of the epoxy glue, electrical isolation is achieved between the actuator and load sensor.

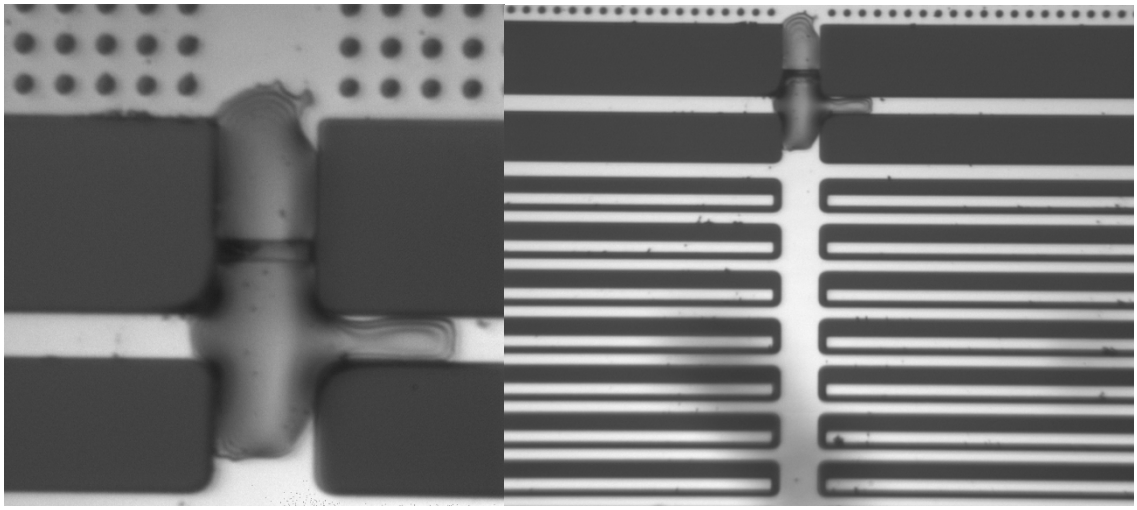

Figure 2.9: Epoxy glue applied in the gap to glue the actuator and the sensor together.

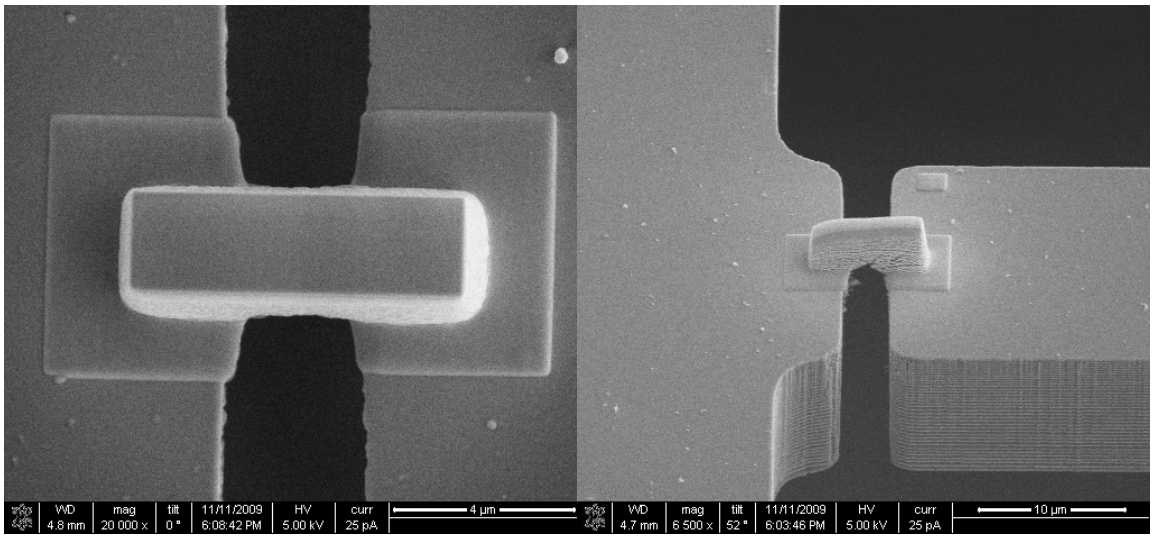

Figure 2.10: Platinum bridge deposited across the specimen gap (Left: Top view, Right: View at 52 degrees to the device plane)

Another technique used to connect the actuator and the load sensor was using Pt deposition (using Focused Ion Beam) to form a bridge between the actuator and load sensor (Fig. 2.10). This connects the actuator and load sensor structurally as well as electrically. If electrical connectivity is to be avoided, Pt micro-bridge is deposited after deposition of insulating oxide coating using ALD or application of insulating epoxy glue.

The developed MEMS nanotensile testers were fabricated with the SOIMUMPS process (MEMSCAP*). This process relies on bulk micromachining of a SOI (Silicon-On-Insulator) wafer.

The process uses a 100 mm n-type double side polished silicon-on-insulator (SOI) wafer as the starting substrate consisting of the following layers:

(a) Top Silicon layer: thickness 10 ± 1 µm

(b) Intermediate oxide layer: thickness 1 ± 0.05 µm

(c) Handle wafer/substrate: thickness 400 ± 5 µm

The surface of the top silicon layer is doped using PSG (phosphosilicate glass) deposition and annealing. A pad metal layer consisting of 20 nm chrome and 500 nm gold is deposited to form the various metal pads for making external electrical connections. Deep Reactive Ion Etching (DRIE) is used to etch the Silicon layers with the top 10 µm silicon forming the structural layer for the developed MEMS devices. Wet oxide etch as well as vapor phase HF etch is used to selectively remove the middle oxide layer.

The 10 micron thick structural layer of the devices consists of monocrystalline doped Si and is electrically isolated from the substrate with a 1 micron thick oxide layer. The mechanical and electrical parameters of SOIMUMPs process layers are listed in Table 2.1.

---

* http://www.memscap.com/mumps/documents/SOIMUMPs.dr.v5.pdf

Table 2.1: Mechanical and electrical parameters of SOIMUMPS process layers

Film	Thickness(microns)			Sheet Resistance (ohm/sq) or Resistivity (ohm-cm)		
	Min.	Typ.	Max.	Min.	Max.	Comments
Pad Metal	0.47	0.52	0.57	0.045	0.065	Ohm/sq
Silicon	9	10	11	15	25	Ohm/sq (N-type at surface post doping)
				1	10	Ohm-cm (N-type)
Oxide	0.95	1.00	1.05	N/A		
Substrate	395	400	405	1	10	Ohm-cm (N-type)

2.4 Actuator Characterization

2.4.1 Experimental Setup

Each die obtained from MEMSCAP (each die consists of several MEMS devices – see Fig, 2.11) was glued on to a ceramic IC package which was then used to make electrical contacts with the device. Contact pads of the MEMS device were wire bonded to the IC package which was then connected to the driving source. Agilent 3649a was used as the power source to give the required driving voltage to the actuator.

A DC voltage was applied to the actuator pads of the nanotensile tester and the corresponding deflection of the actuator was measured using an optical microscope system in air. A magnification of 100X (pixel size - 46 nm) was used for optical gap change measurements. Also the current flowing through the actuator was recorded (using Agilent 3649a itself).

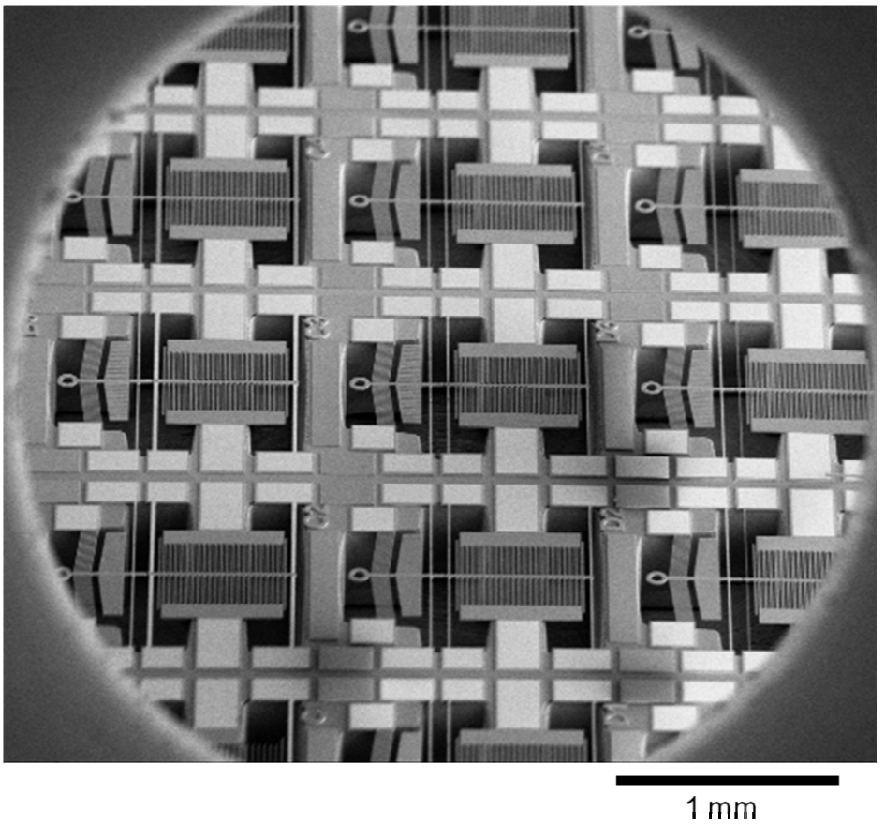

Figure 2.11: SEM image of various devices on a single die.

2.4.2 Sub-diffraction Limit Optical Measurements Principle

Diffraction is known to limit the accuracy of optical measurements to a spatial resolution comparable to the wavelength of light being used [49, 50, and 51]. However, the following method was able to measure the gap ***change*** with accuracy below the diffraction limit. Typically, an intensity varying diffraction pattern is obtained near an edge which optically limits the spatial resolution to the order of wavelength of light being used. However in our case keeping the intensity of light constant, we set a threshold in the intensity variation (see Figs. 2.12 and 2.13) which determines the position of an edge of the gap where the nanowire is to be placed (or the edge of a load sensor comb for a calibration device). Since the actual gap (~4 μm) is much higher than the diffraction

limit, the stationary or the load sensor edge of the gap (or an edge of a corresponding fixed comb structure for a calibration device) does not affect the intensity variation due to the diffraction profile at the other edge of the gap (the moving actuator edge). As the driving voltage is increased, the actuator gap edge moves away, increasing the gap. However the intensity profiles at the gap edges due to diffraction remain the same. Consequently the shift of the threshold intensity point of the moving edge profile is the same as the shift of the actual edge location. Hence, even though the intensity threshold does not determine the actual position of the edge accurately, the change in gap determined by the shift in this intensity threshold edge is highly accurate to the pixel resolution, giving us highly accurate measurements optically which would otherwise not be possible. This is further improved by increasing the intensity of incident light significantly, causing near saturation in the optical imaging system causing a sharp contrast in the intensity variation in the near edge region making it easier and accurate to make the measurements.

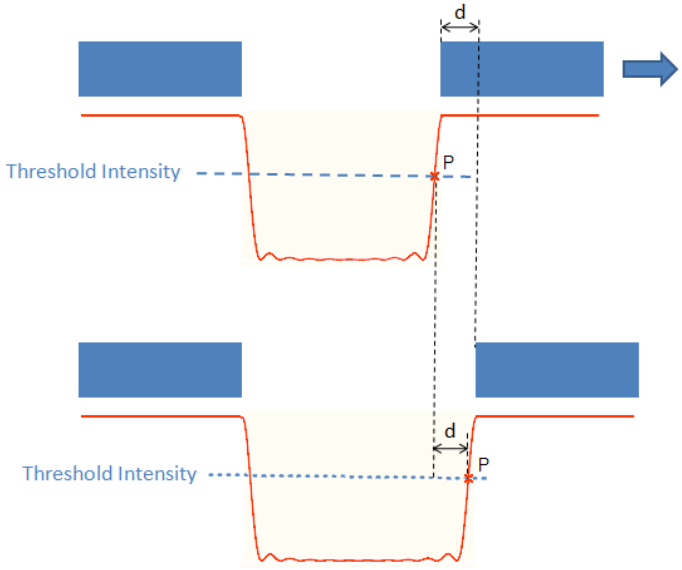

Figure 2.12: An illustration of the intensity profiles due to diffraction at the edges. Note that a shift in the actual edge location causes an equal shift in the edge diffraction profile and consequently an equal shift in the position of point P.

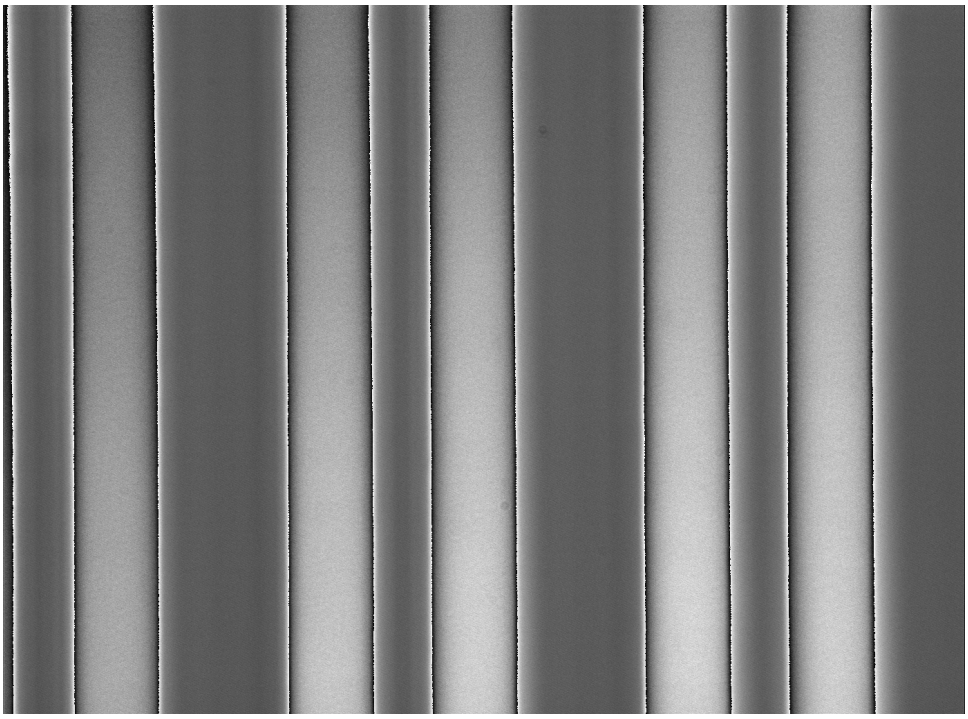

(a)

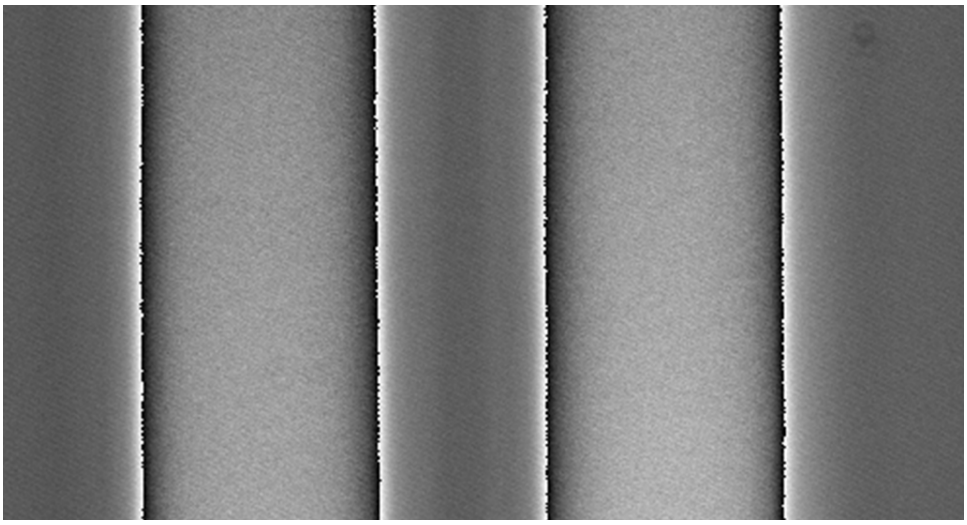

(b)

Figure 2.13: Image of the load sensor comb structures for a Calibration device used for optical calibration. The dark vertical lines represent the threshold intensity profile for the edges. The relative shift in these is used to calculate the deflection. The pixel level resolution claimed can be observed in the highly magnified image (b).

2.4.3 Results

The current flowing through the actuator for different applied voltages was recorded for the MEMS devices in air. A fairly linear dependence is obtained up to 2V applied driving voltage above which non-linear temperature effects become more prominent (see Fig. 2.14).

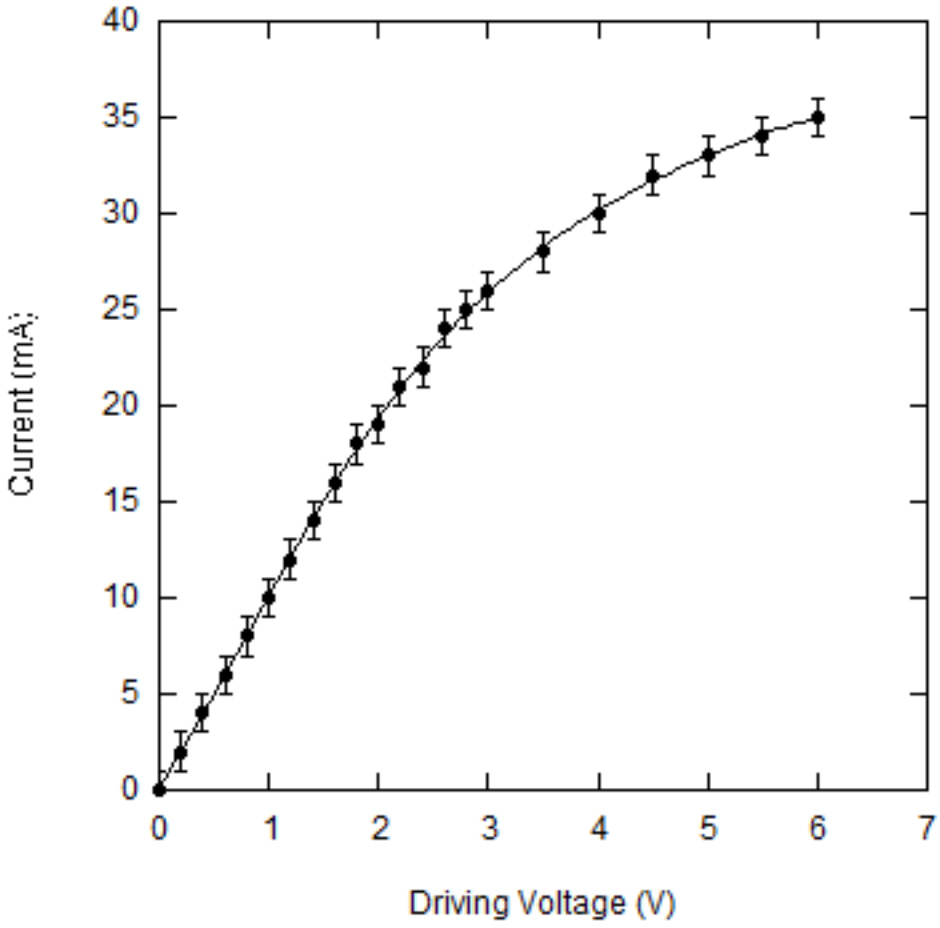

Figure 2.14: Variation of current flowing through the actuator with the applied driving voltage measured experimentally.

The actuator deflection was measured optically for various applied driving voltages for both SOIMUMPs24 and SOIMUMPs27 designs (see Fig. 2.15 and 2.16).

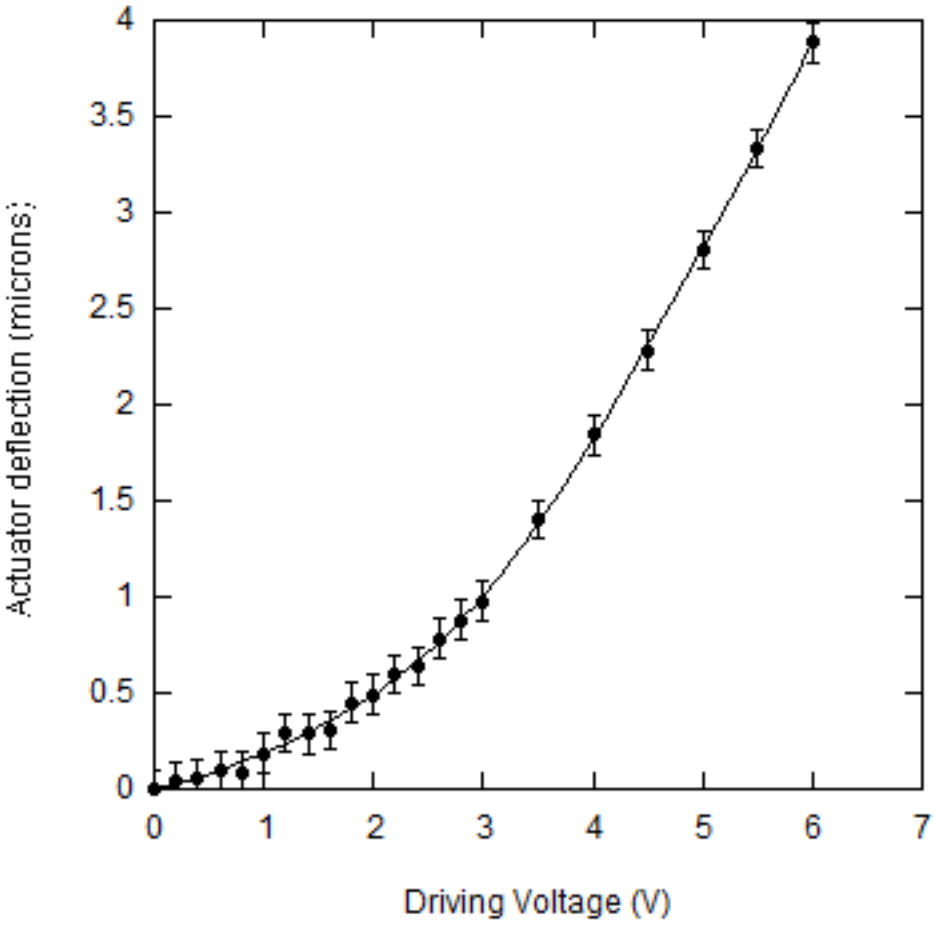

Figure 2.15: Actuator deflection (measured optically) variation with driving voltage (0-6V) in air for SOIMUMPs24 device.

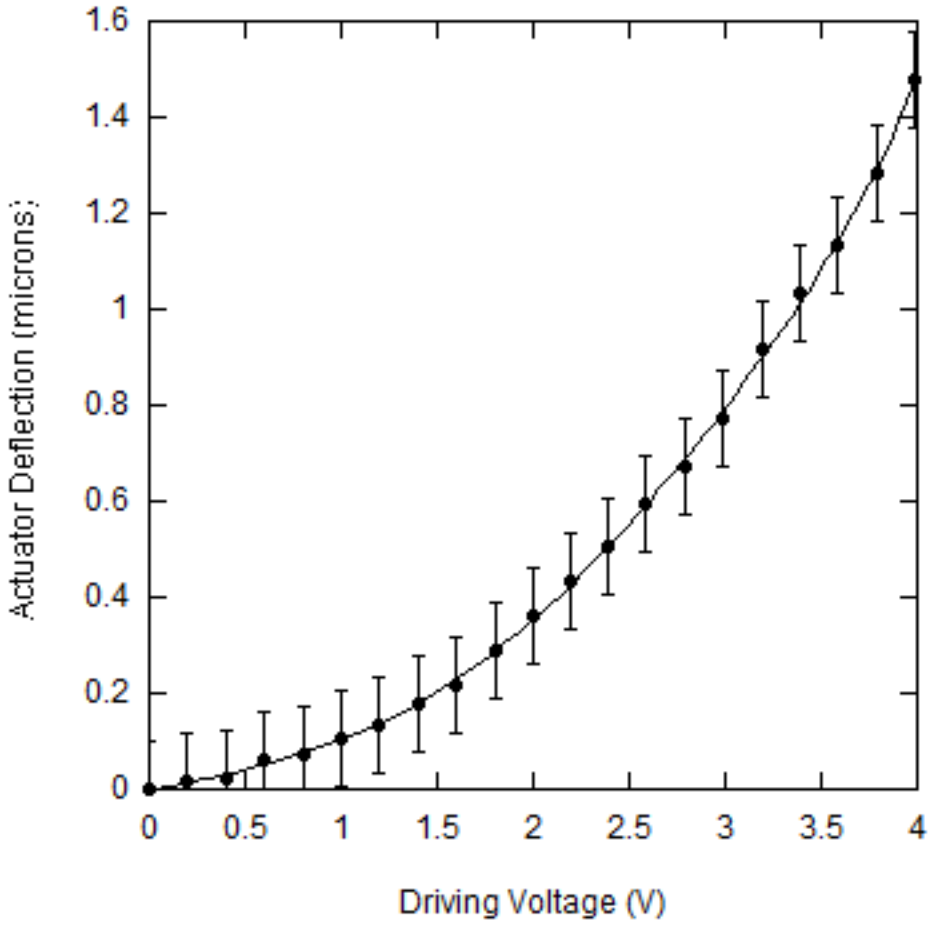

Figure 2.16: Actuator deflection (measured optically) variation with driving voltage in air for SOIMUMPs27 calibration device.

The deflection is greater in SOIMUMPs27 as compared to SOIMUMPs24 (Fig. 2.17). This effect can be attributed to the increased heat sink size and additional stiffness beam in the actuator which results in lower temperatures for the same applied driving voltage and hence lesser deflection.

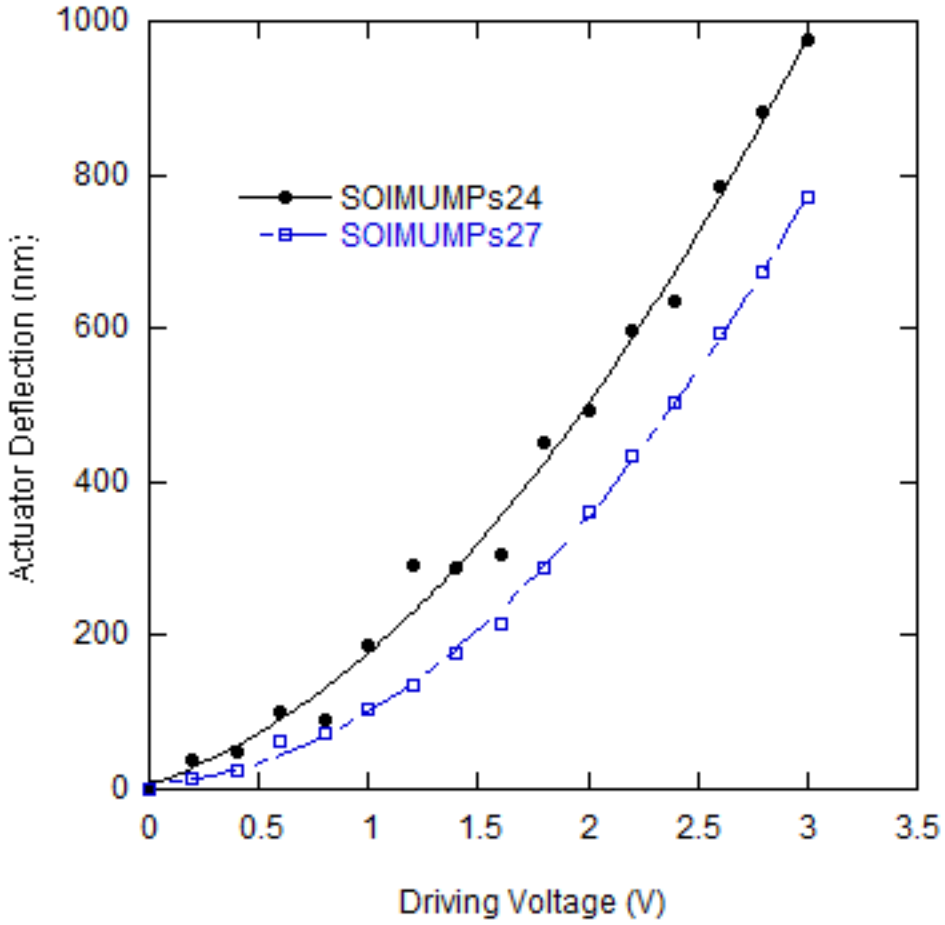

Figure 2.17: Gap change with driving voltage compared for both SOIMUMPs24 and SOIMUMPs27. Two devices for each of the designs were used for optical calibration, and repeatable results were obtained. Furthermore, no significant measurable difference in deflection was observed between normal and calibration devices.

2.5 Thermal Characterization

The objective of this characterization was to measure the temperature profile near the nanowire as well as actuator beams. High temperatures near the specimen may damage the nanowires being tested. Furthermore high temperatures of the actuator beams may result in their deterioration affecting the reusability of the devices as well as tests

conducted over long time periods. Infra-Red microscopy as well as Micro-Raman spectroscopy was conducted to measure the temperatures.

2.5.1 Infra-Red (IR) Measurements

Infrared microscope was used to find out the temperatures achieved in the actuator as well as near the specimen gap for SOIMUMPs24. The various temperature profiles obtained using IR microscope are shown in Fig. 2.18 and 2.19.

However several studies have showed that silicon (and semiconductors in general) can be transparent to the infra-red radiations and hence these profiles may also reflect the IR signatures of the substrate below the thermal actuator [52]. Hence Raman Spectroscopic measurements were also performed to obtain more representative temperature information for the devices used (see section 2.5.2).

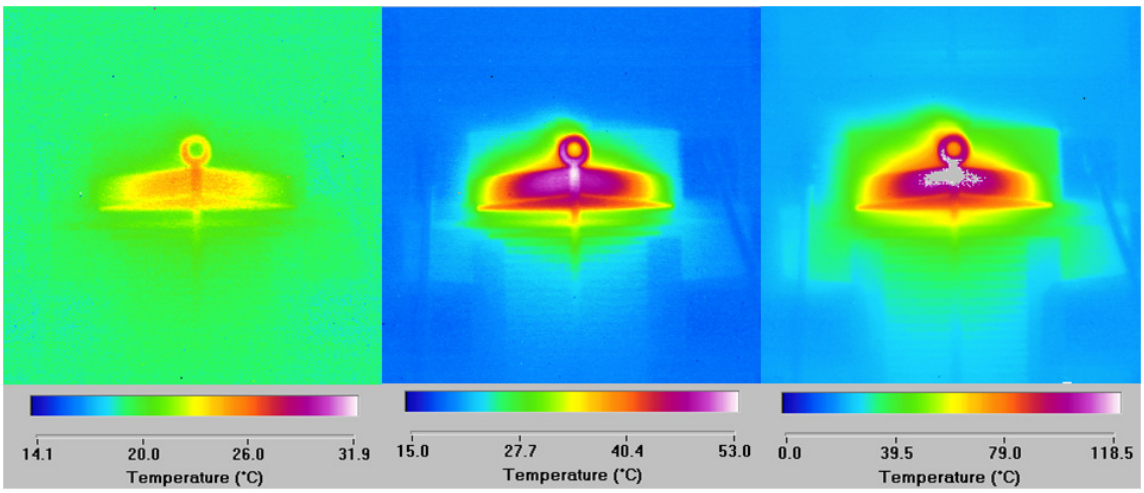

1 V , 11 mA 2 V , 20 mA 3 V , 27 mA

Figure 2.18: Temperature profiles obtained using IR microscope for 3 different driving voltages.

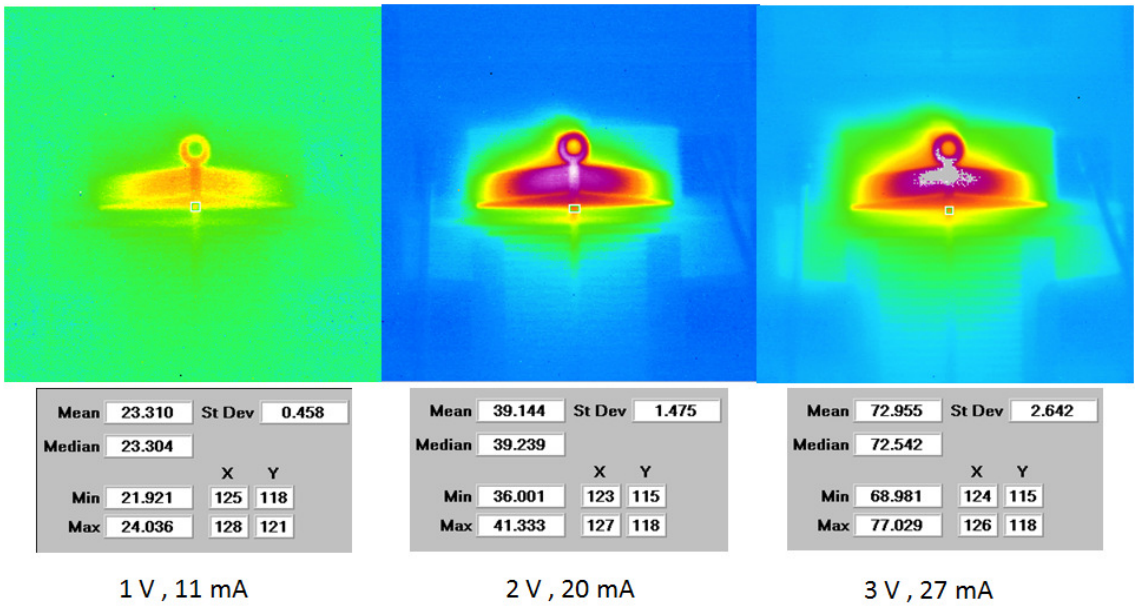

1 V , 11 mA 2 V , 20 mA 3 V , 27 mA

Figure 2.19: Temperatures near the nanowire for three different driving voltages using IR microscope. The data sets show the temperature variation near the specimen gap.

2.5.2 Micro-Raman Spectroscopy

Micro-Raman measurements were made to determine the temperatures achieved for varying driving voltages at different locations (see Figs. 2.20 and 2.21) of the device including regions near the specimen (refer Appendix A).

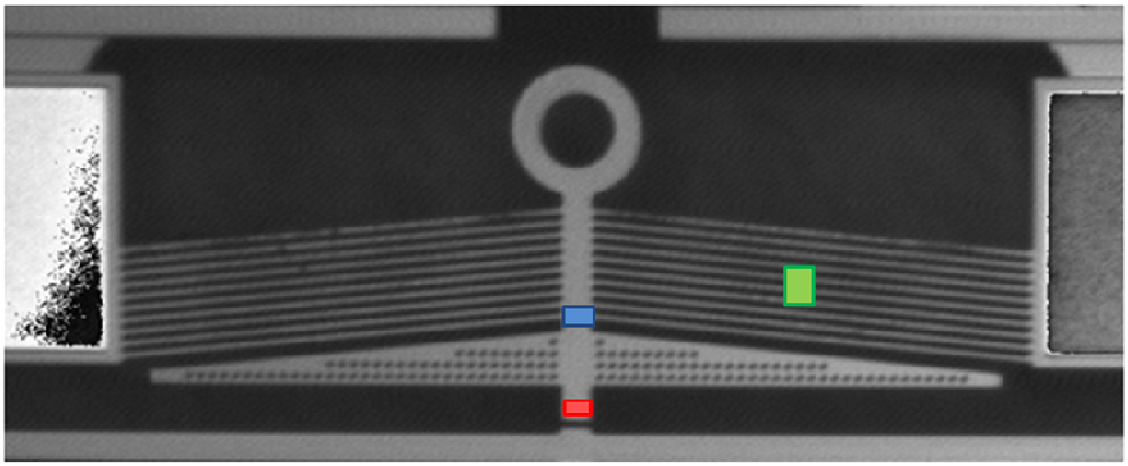

Figure 2.20: Various locations where the temperature was measured using Micro-Raman spectroscopy (Red – Near Specimen, Blue – Before HS (Heat Sink), Green – Beam Middle).

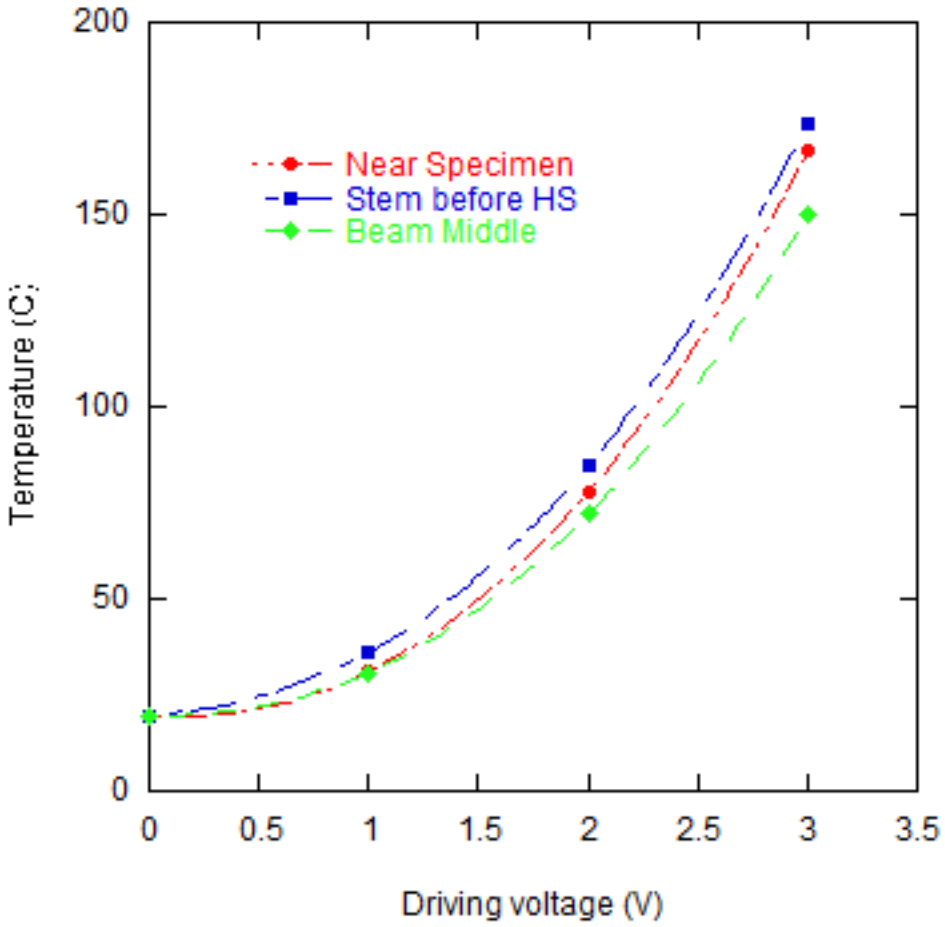

Figure 2.21: Temperatures at different locations (refer Fig. 2.20 for location nomenclature) and varying driving voltages/currents for a SOIMUMPs24 MEMS device obtained using Micro-Raman measurements.

2.5.3 Micro-Raman Vs Infra-Red (IR)

Temperatures achieved at various locations of the MEMS nanotensile tester measured through IR and Raman spectroscopy were found to be different (Fig. 2.22). Raman temperatures were found to be significantly higher as compared to those measured using IR. The significant difference can be attributed to the fact that silicon is transparent to IR radiations and hence the calculated temperatures include the signatures of the substrate

below the device and not just the device [52]. Hence micro-Raman measurements show a more promising representation of the device temperatures and were used for device characterization.

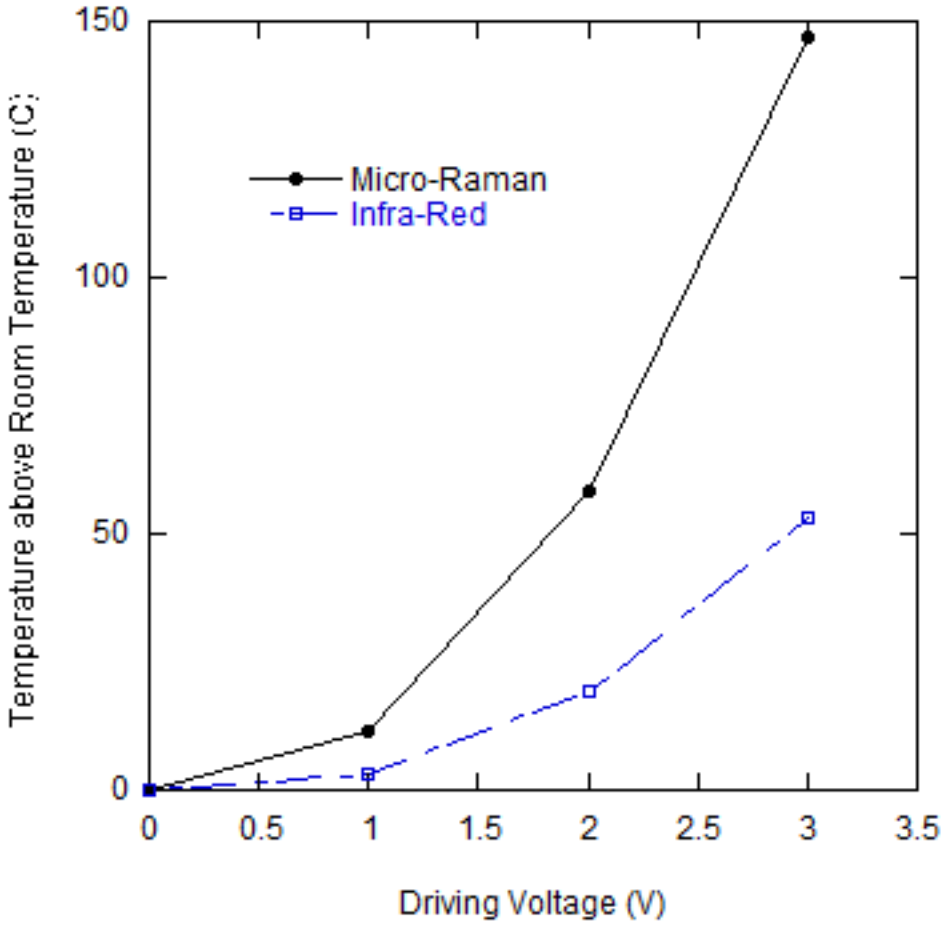

Figure 2.22: Comparison between the IR and Raman measurements. The plot shows the temperature increase measured near the specimen location for the same device for different applied driving voltages.

2.5.4 SOIUMUMPs24 Vs SOIMUMPs27

Micro-Raman measurements [53] were done for the two device designs to compare the temperatures achieved near the specimen location (refer Table 2.2, Figs. 2.23 and 2.24) for various applied driving voltages.

Table 2.2: A comparison of the temperatures near the specimen for various driving voltages, for the two device designs SOIMUMPs24 and SOIMUMPs27.

Device	**Driving Voltage(V)**	**Temp [ºC]**
SOIMUMPs24	0	19.8
SOIMUMPs24	1	31.6
SOIMUMPs24	2	70.7
SOIMUMPs24	3	142.8
SOIMUMPs27	0	19.8
SOIMUMPs27	0.5	24.0
SOIMUMPs27	1	32.3
SOIMUMPs27	1.5	42.1
SOIMUMPs27	2	54.6
SOIMUMPs27	2.5	76.2
SOIMUMPs27	3	101.9

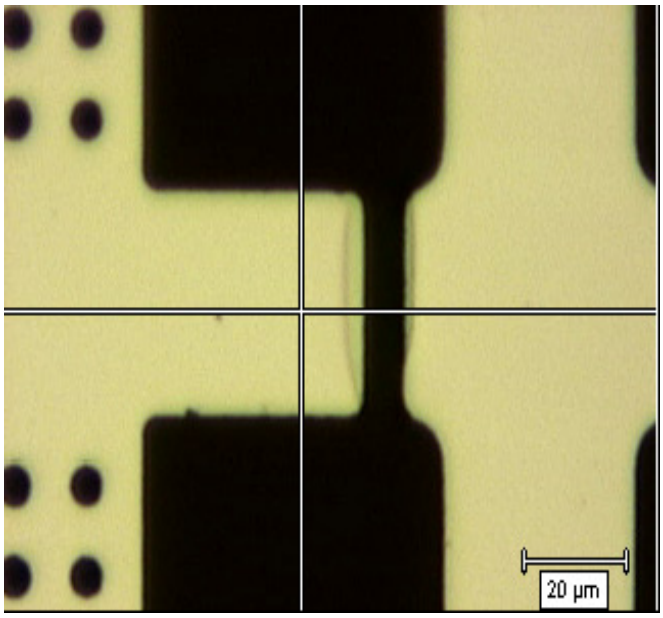

(a)

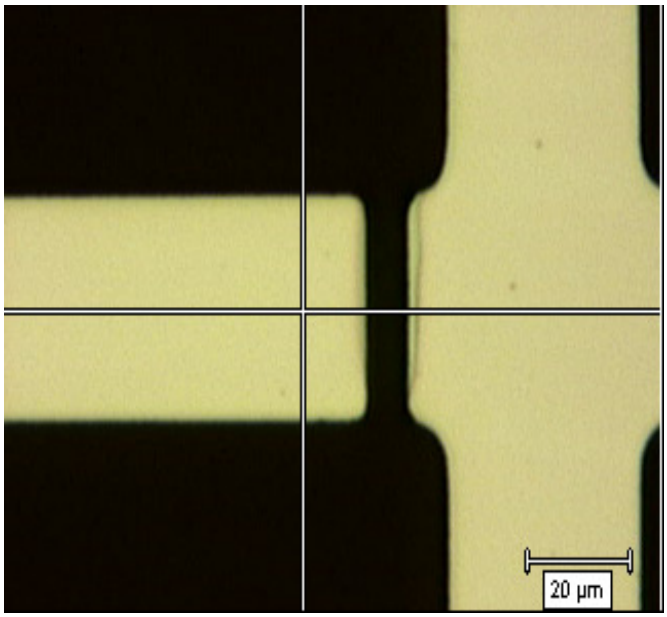

(b)

Figure 2.23: Location on the two devices where Raman measurements were made (a) SOIMUMPs24, (b) SOIMUMPs27.

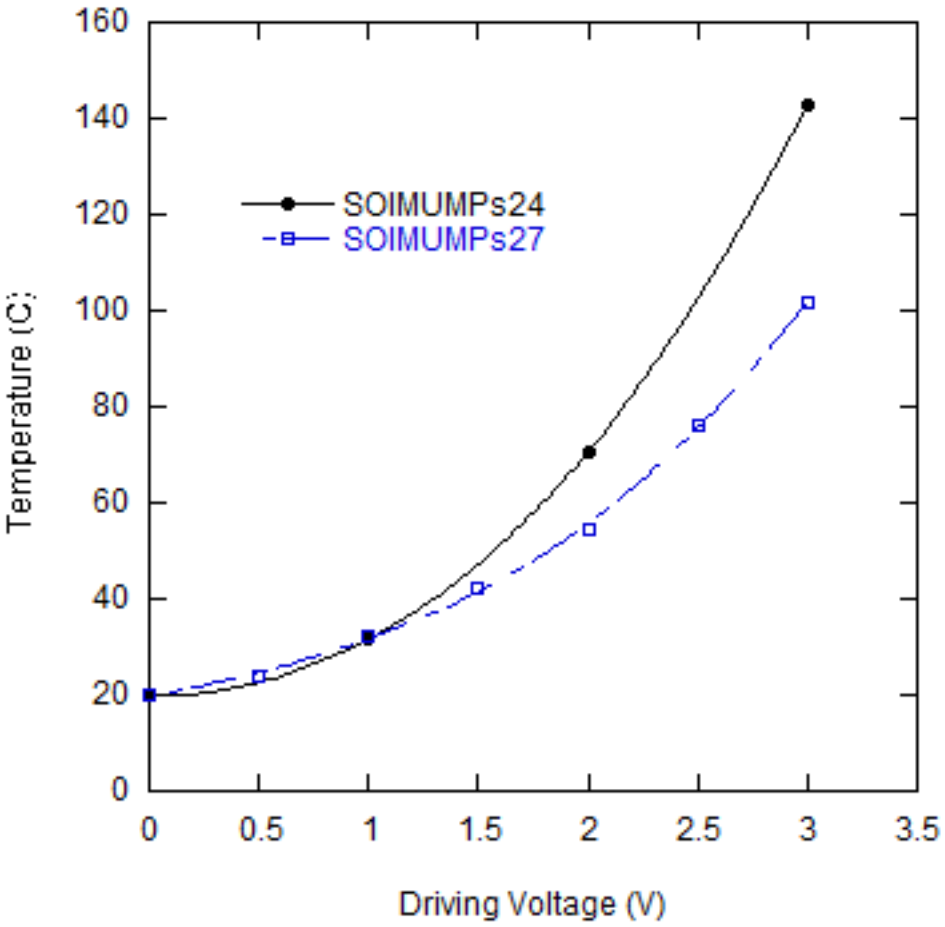

Figure 2.24: Variation of temperature (near the specimen location) with driving voltage for the two designs measured using Micro-Raman.

The temperatures achieved near the specimen were found to be lower for SOIMUMPs27 design as compared to SOIMUMPs24 (Fig. 2.24). This effect can be explained due to the presence of a larger heat sink and extra set of beams near the specimen location for SOIMUMPs27 (refer Section 2.3). This also results in a decrease in actuator deflection for the same driving voltage (see Fig. 2.17).

2.6 Load Sensor Stiffness Characterization - Resonance Method

The method uses the principle of electrostatic force of attraction between two capacitor plates when a potential is applied across the capacitor. The combs of the load sensor form the capacitor plates and when a voltage is applied across the load sensor, these combs experience an electrostatic attractive force. This force was used to apply a periodic force on the load sensor, which was forced to resonate, and the resonant frequency obtained was used to determine the load sensor stiffness.

2.6.1 Experimental Setup

A sinusoidal voltage of amplitude 62V was applied across pads 1 and 2 (Fig. 2.25) for a 9 µm load sensor stiffness beam. The resulting amplitude of vibrations of the load sensor was measured optically from the blur observed (Fig. 2.26) due to the load sensor oscillations. 100X magnification (pixel size - 46 nm) was used to capture the images. Agilent 33220A waveform generator was used along with AVTECH-110G high voltage amplifier to provide the required voltage.

The frequency of the applied voltage was varied and the corresponding amplitude of load sensor oscillations was measured. The peak of the amplitude-frequency curve (Fig. 2.27) corresponds to the resonant frequency of the load sensor.

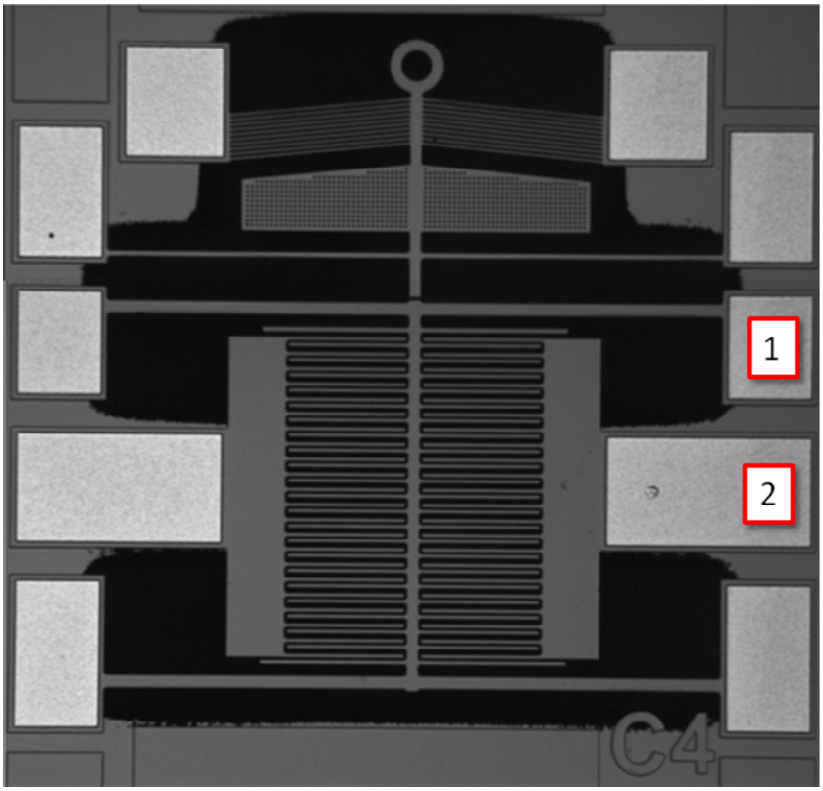

Figure 2.25: Illustration of the configuration for resonance measurements. A sinusoidal voltage of amplitude 62V was applied across pads 1 and 2 shown in figure.

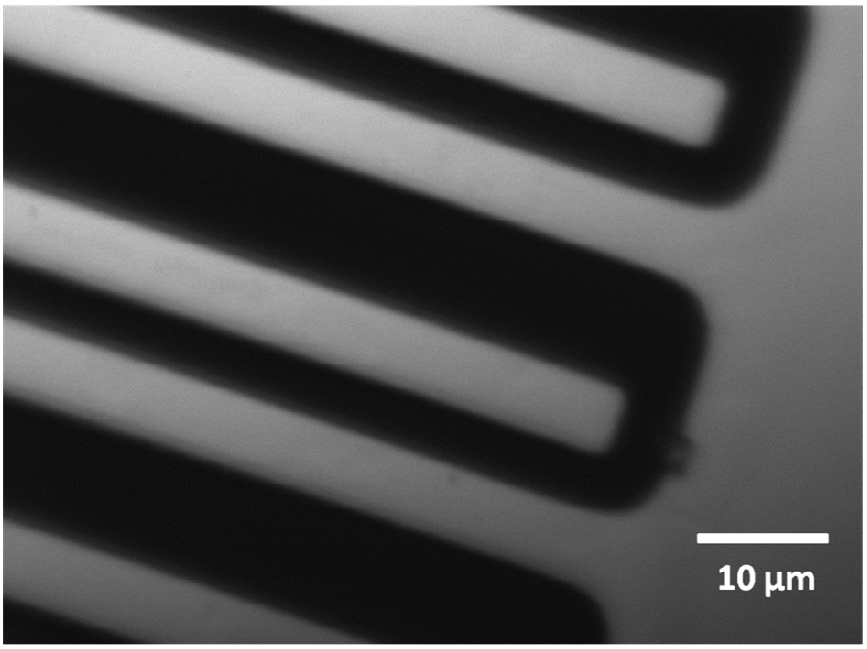

(a)

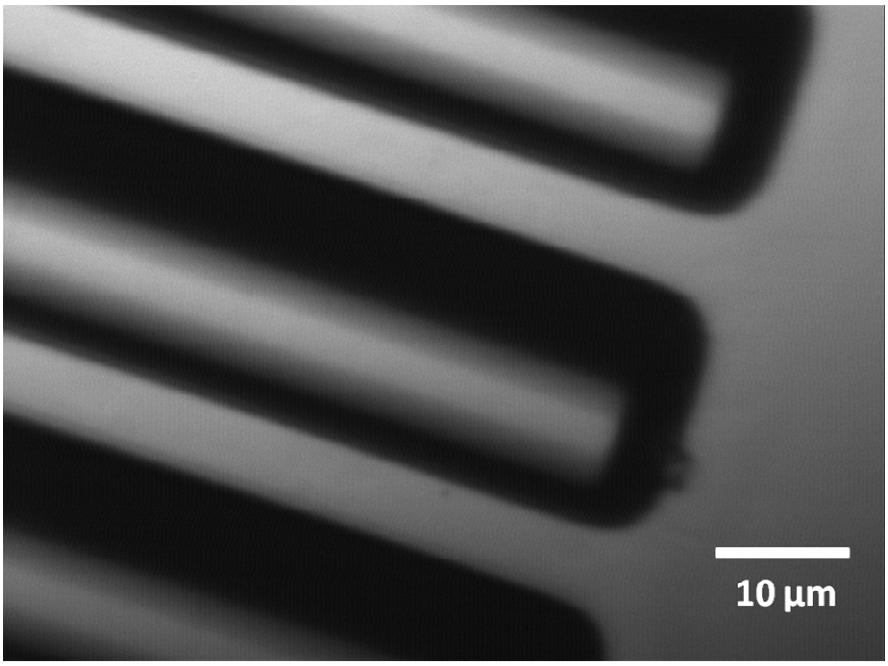

(b)

Figure 2.26: Optical image of the load sensor comb structures (a) When no voltage is applied (b) At resonance. The blur observed in (b) was used to measure the oscillation amplitude.

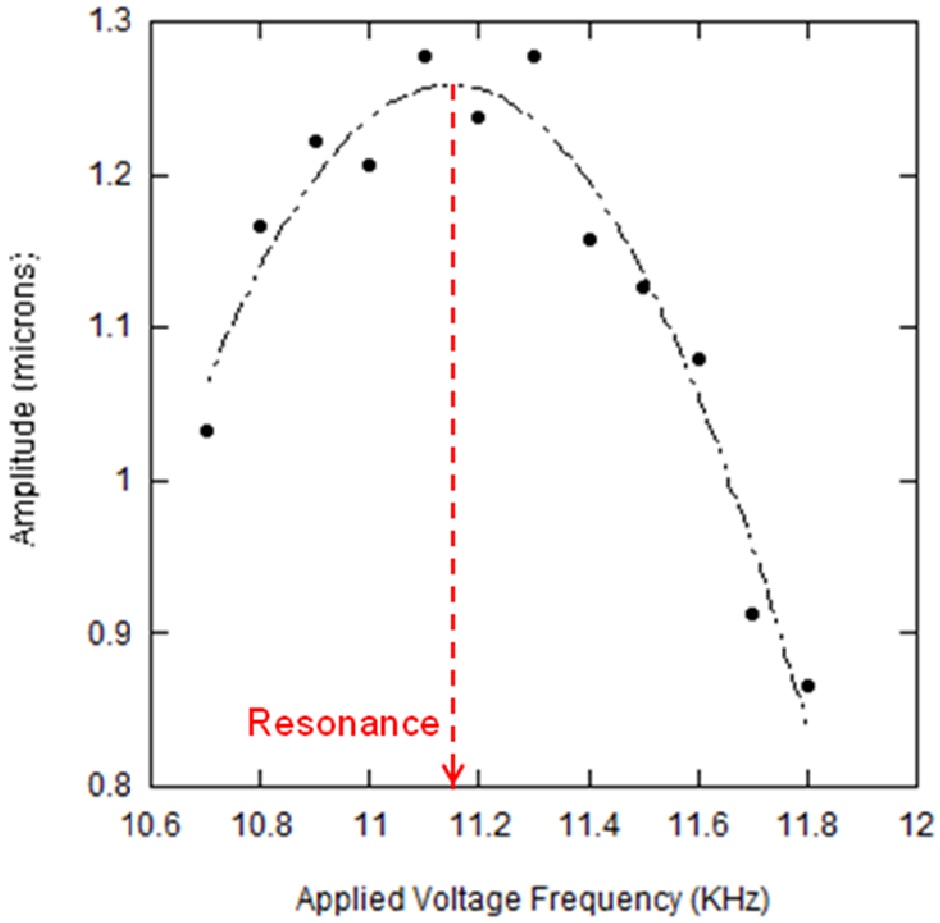

Figure 2.27: Amplitude of load sensor Vs frequency of applied waveform for 9 µm load sensor stiffness beam. The peak amplitude corresponds to the resonant frequency of the load sensor.

The maximum amplitude of vibration corresponds to 11.147 KHz frequency of applied waveform. Since the frequency of the applied force is twice the frequency of the applied sinusoidal waveform, the resonant frequency of load sensor = 2 x 11.147 = 22.29 KHz.

2.6.2 Load Sensor Stiffness Calculations

An accurate analytical expression for the resonant frequency is given by (refer Tang et. al. [54])

$$f_r = \frac{1}{2\pi}\left[\frac{K_{sys}}{M_S + 0.3714M_B}\right]^{1/2} \tag{2.3}$$

Where K_{sys} is the system stiffness, M_S is the mass of movable shuttle and M_B is the mass of supporting beams.

The load sensor stiffness is calculated from

$$K = (2 \pi f_r)^2 (M_S + 0.3714M_B) \tag{2.4}$$

Density of Si used was 2329 kg/m^3 [55].

For 9 µm load sensor stiffness beams: Using f_r = 22.29 (refer Section 2.6.1), K_{sys} = 35.57 N/m

However for more accurate load sensor stiffness results, the resonance tests must be done in vacuum (as compared to the tests in air as described above) [56].

2.7 Electrical Sensing

2.7.1 Resistive Sensing

2.7.1.1 Setup

The SOIMUMPs27 design includes the possibility of 2-point resistance measurements across a conductive specimen. Pads 1 and 2 (see Fig. 2.28) were used to make the 2-point resistance measurements and this technique was used to detect failure of a conductive specimen during tensile loading. Theoretically, the failure of a conductive specimen would result in an infinite resistance measured across pads 1 and 2. Resistance measurements were made using Agilent 34420A NanoVolt, Micro-Ohm Meter.

2.7.1.2 Results

A Pt microbridge was deposited using FIB (Focused Ion Beam) and was further cut to form a sharp notch to assist failure (see Fig. 2.29). This was used to verify the working principle behind failure detection. An incremental loading was done and consecutive resistance measurements were made to detect failure. A very large resistance increase resulting in resistance overload was observed at the failure point (see Fig. 2.30) which was verified optically.

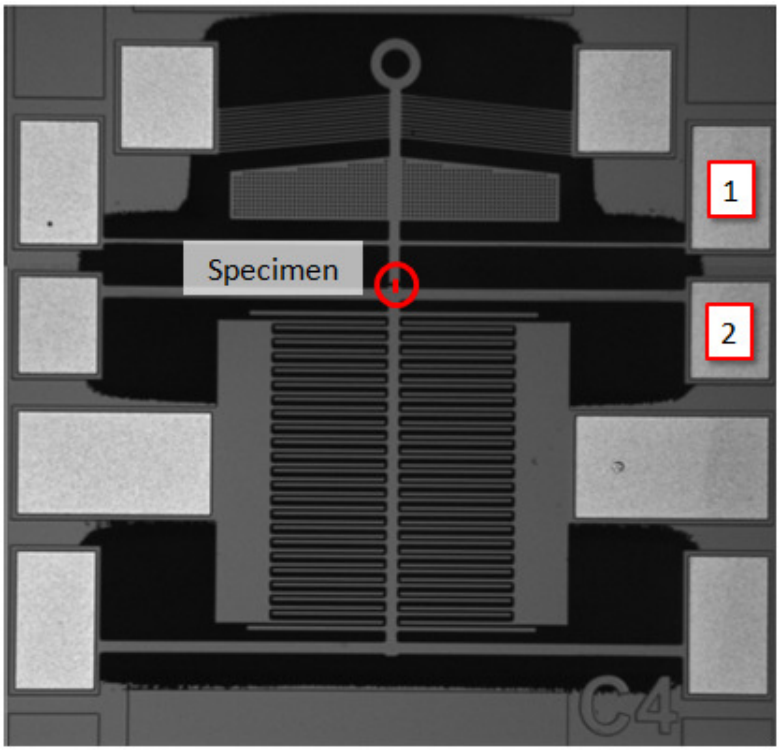

Figure 2.28: The configuration for 2-point resistance measurements done across pads 1 and 2.

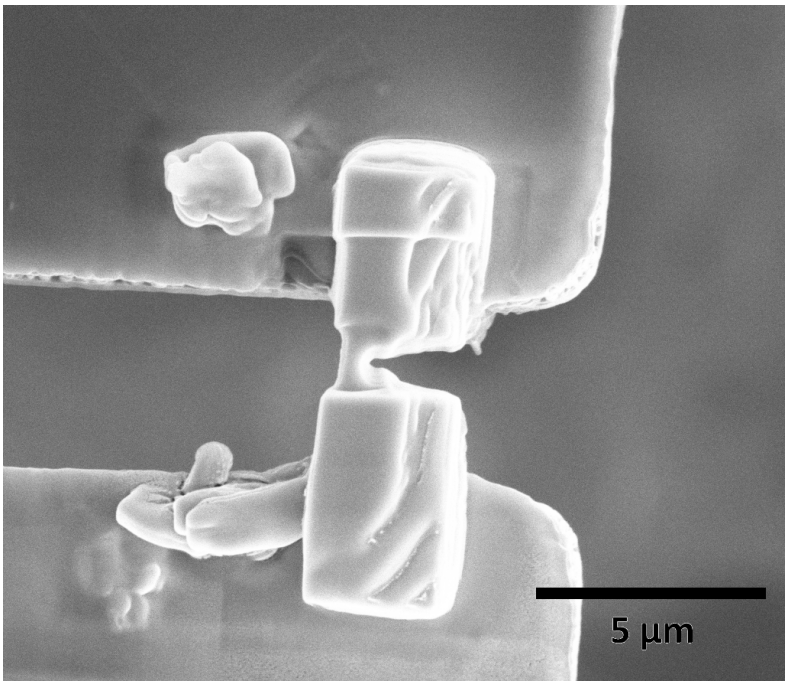

Figure 2.29: Notched Pt microbridge used for verification of failure detection principle.

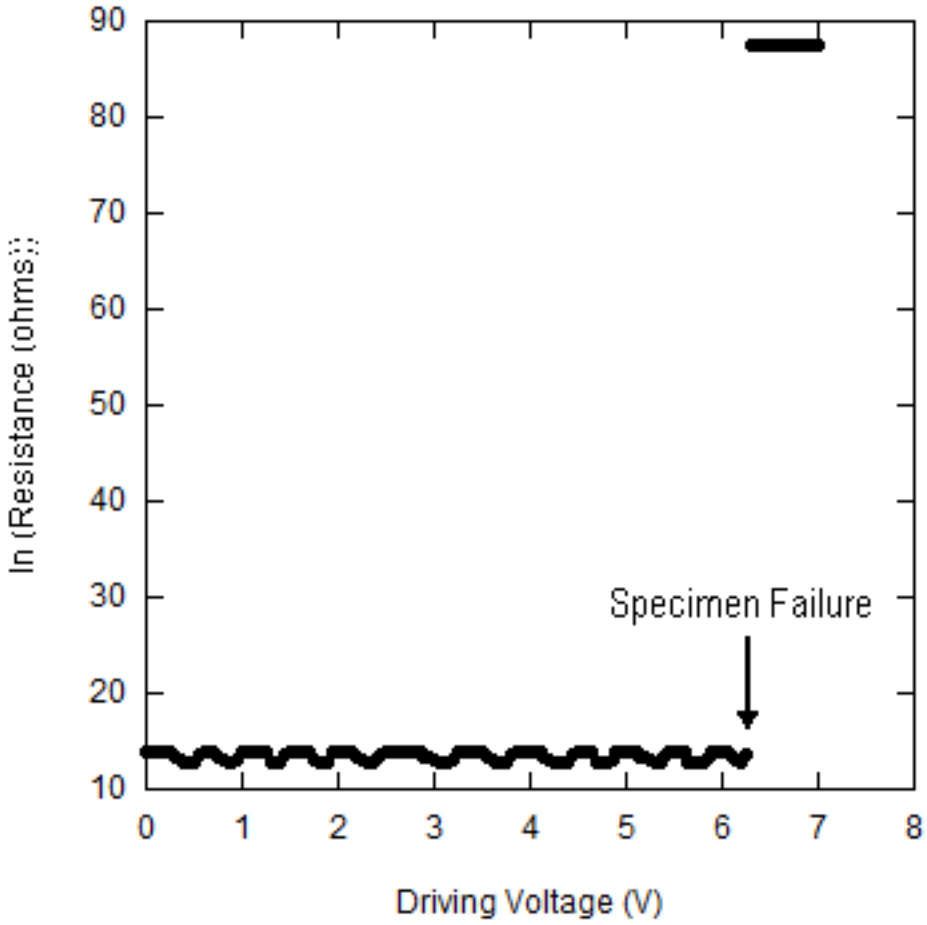

Figure 2.30 : Failure detection using resistive sensing. The plot shows the sudden increase in resistance (semi-log) measured across the specimen at failure. Theoretically an infinite resistance should be achieved at specimen failure.

However resistive sensing can be used only to detect failure and consequently calculation of failure stress for a specimen. It is unable to provide direct strain measurements for the specimen; consequently properties like Young's modulus or stress strain curves cannot be directly determined using resistive sensing. Furthermore, the current flowing through the nano-specimen for resistive measurements should be minimized to prevent Joule heating and consequent degradation of the nano-specimen.

2.7.2 Capacitive Sensing

For a tensile test, to determine the load sensor deflection and consequently force and specimen elongation, a relationship between capacitance change and load sensor deflection has to be established. Hence characterization of capacitance sensing becomes extremely important.

2.7.2.1 Experimental Setup

Each die obtained from MEMSCAP was glued on to a ceramic IC package which was then used to make electrical contacts with the device. An Agilent 3649a power source was used to give the required voltage to the actuator. Contact pads of the MEMS device were wire bonded to the IC package which was then connected to the driving source and the sensing circuit (Fig. 2.31). The MS3110 chip (Irvine Sensors, Inc.) was used to measure the capacitance change. The MS3110 basically works in differential mode (refer Fig. 2.32). It senses the capacitance change between two capacitors resulting in an output proportional to the capacitance change. If one of these capacitances is kept fixed, the capacitance change for the other capacitor can be calculated. The capacitance being measured (load sensor) is connected to either CS1IN or CS2IN (see Fig. 2.32) and chip capacitances CS1 and CS2 are initially selected such that $CS1_T \sim CS2_T$. Any change in the capacitance being measured causes a change in $CS1_T$ or $CS2_T$ and consequently results in a change in the net charge flow to the charge amplifier consequently causing a change in the output voltage. The expression for the output voltage is given by

$$V_0 = GAIN * V2P25 * 1.14 * (CS2_T - CS1_T)/C_F + VREF \quad (2.5)$$

Where V_0 is the output voltage

GAIN = 2 or 4 V/V nominal

V2P25=2.25V

$CS1_T$=CS1IN+CS1

$CS2_T$=CS2IN+CS2

VREF=2.25V

C_F is the Feedback capacitor

The capacitance change for the load sensor can then be calculated from this change in the output voltage (V_0). The amplification factor for the output is determined by the feedback capacitor (C_F) (lower the C_F, higher is the amplification factor). The connections from MS3110 were soldered directly to the ceramic package and the complete setup was enclosed in a Faraday cage for noise reduction.

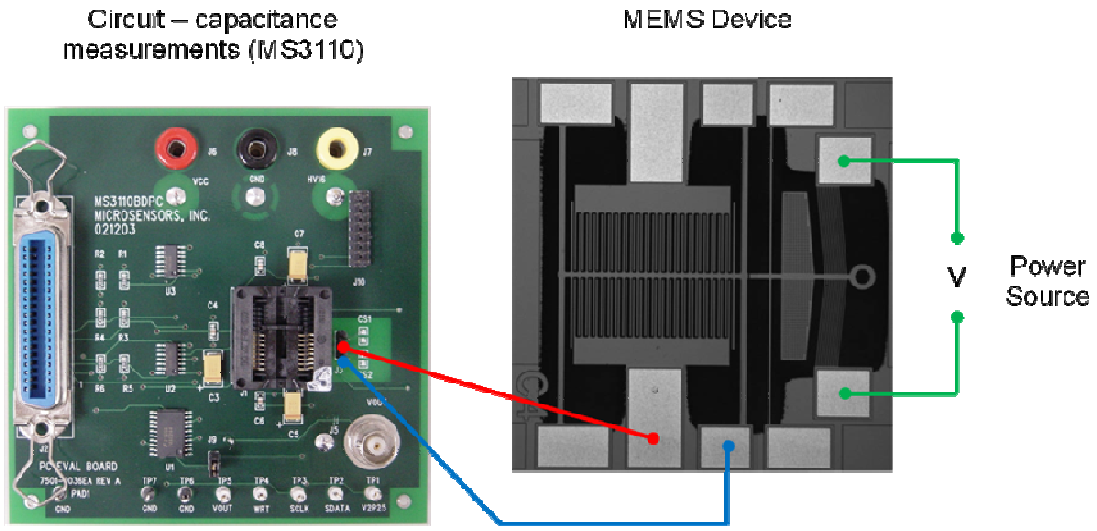

Figure 2.31: An illustration of the experimental setup (capacitive sensing). The setup is enclosed in a Faraday cage for noise reduction. The red and blue wires connect the device pads to CSCOM and CS2 respectively of MS3110.

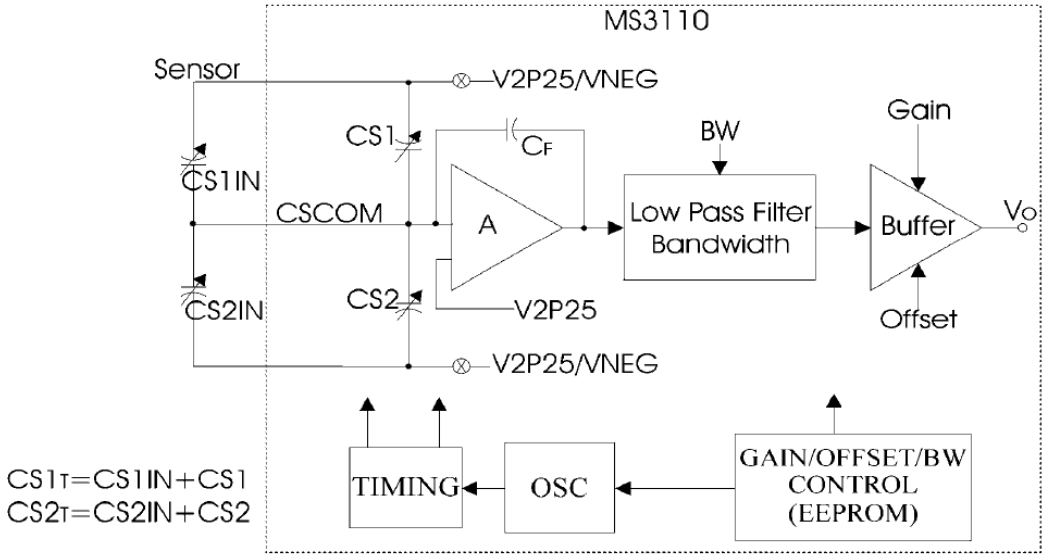

Figure 2.32: MS3110 functional diagram (where V2P25=2.25V, VNEG=0, V0 is the output voltage, C_F is the feedback capacitance and determines the amplification). The capacitance to be measured can be connected either as CS1IN or CS2IN)

The driving voltage was applied in incremental steps and corresponding capacitance change due to load sensor deflection was measured. Sensing requires the use of filters and data averaging for noise reduction in the output signal for high precision measurements. Hence, after each incremental step in voltage, 2000 data points for output voltage (V_0) were captured at 1 KHz frequency which were then analyzed for noise reduction. Concerns regarding acquisition rates and voltage step size on noise levels, repeatability, reliability and precision of measurements have been addressed in Appendix B.

Tests were done for calibration as well as regular devices with various configurations (glued devices, Pt microbridge).

2.7.2.2 Capacitive Characterization

2.7.2.2.1 Calibration Device

For a calibration device, the whole of actuator deflection goes to the load sensor and hence the capacitance change should represent the applied deflection. Since for an applied driving voltage, the deflection is known using optical calibration (section 2.4), a direct correlation between applied deflection and capacitance change would be obtained. Driving voltage was applied in incremental steps and the respective capacitance change was measured (see Fig. 2.33).

However for a calibration device, the actuator is not electrically isolated from the sensing component and consequently an influence of the actuator driving voltage on the sensing output obtained was suspected. Consequently a method to electrically isolate the actuator and sensing modules for characterization was investigated (section 2.7.2.2.2).

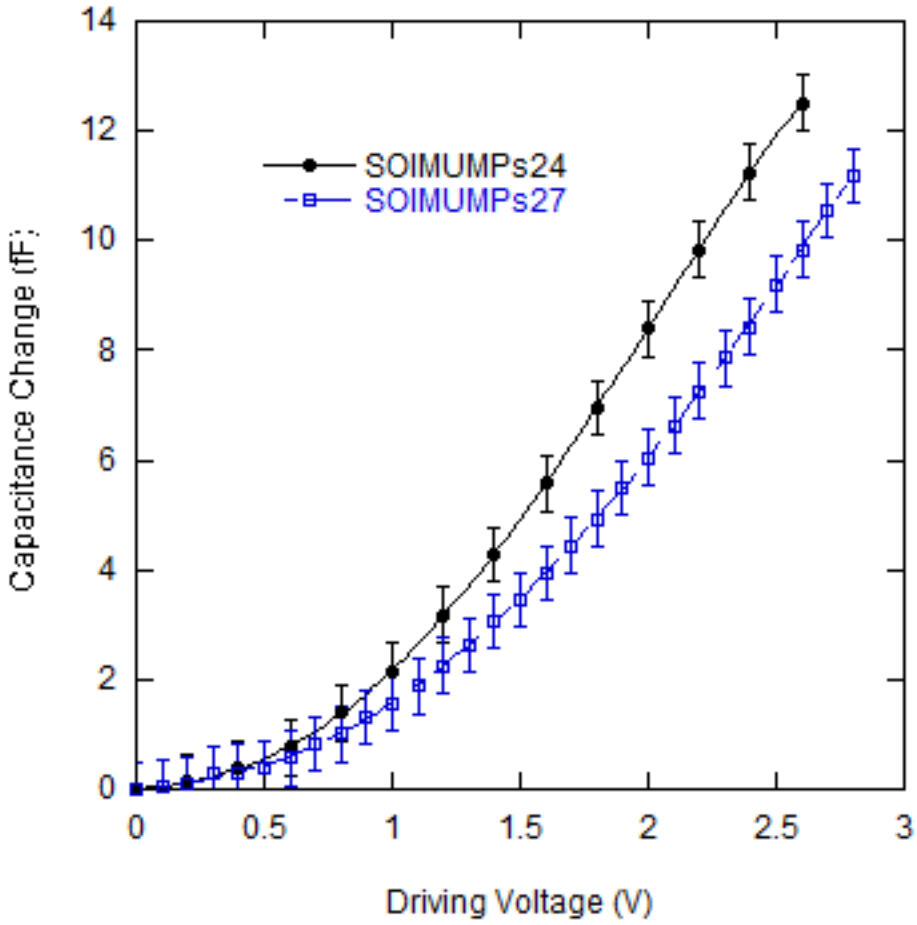

Figure 2.33: Variation of capacitance change with driving voltage for calibration devices for both SOIMUMPs24 and SOIMUMPS27 designs.

2.7.2.2.2 Glued Device

Epoxy non-conductive glue was applied on the specimen gap of non-calibration devices so as to mechanically glue the actuator and the sensor while maintaining electrical isolation of the sensing from the actuator driving voltage. Optical verification was performed to ensure that all the actuator deflection went into the actuator and not the glue. Deflections for a calibration device and a glued device with 9 micron load sensor stiffness beams were measured optically for an applied actuator deflection of 1.5 microns

and no measurable difference was observed. Hence all the actuator deflection was reflected as load sensor deflection and consequently a valid capacitance characterization could be performed using glued devices.

Capacitance change measurements were made for two different glued SOIMUMPs24 devices which showed very good reproducibility (see Fig. 2.34). Refer Appendix B for detailed discussions on repeatability and reliability of measurements.

Capacitance change with driving voltage was also compared for SOIMUMPs24 and SOIMUMPs27 glued devices. For the same applied driving voltage, a lower capacitance change for SOIMUMPs27 was observed (Fig. 2.35). This can be attributed to the lower actuator and consequently load sensor deflections for SOIMUMPs27 design as compared to SOIMUMPs24 (Fig. 2.17).

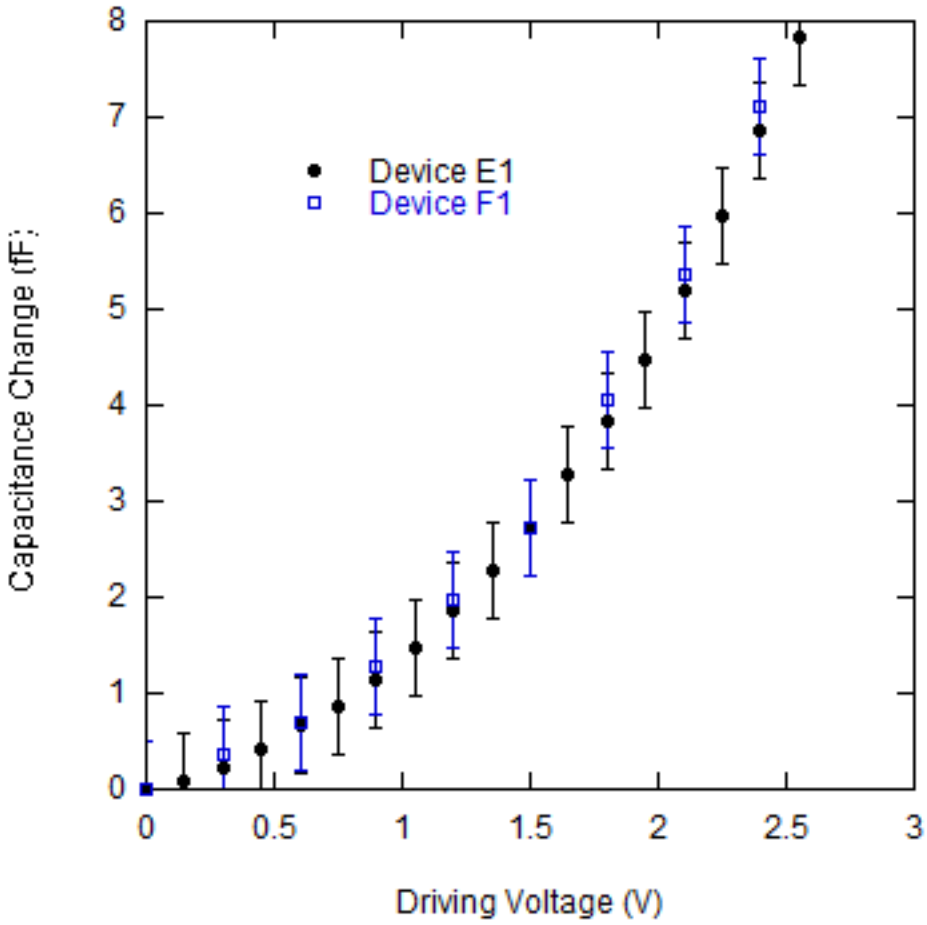

Figure 2.34: Capacitange change variation with driving voltage for two different glued SOIMUMPs24 devices.

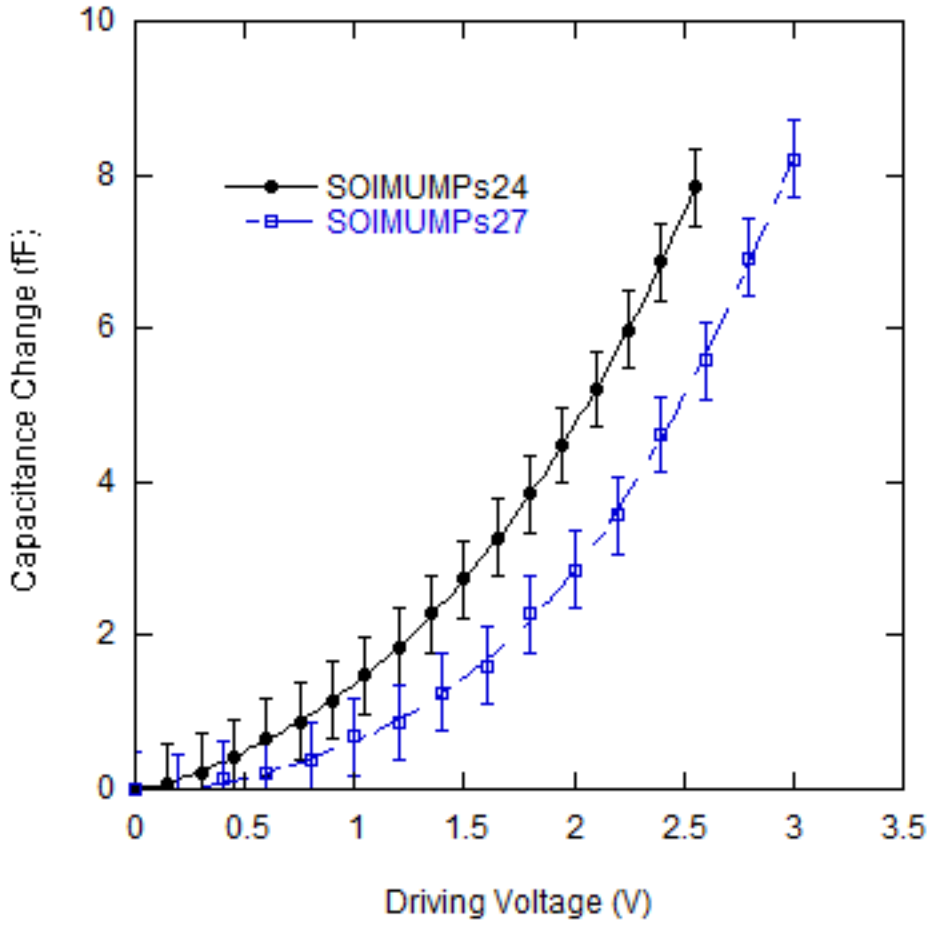

Figure 2.35: Comparison of capacitance change variation with driving voltage for SOIMUMPs24 and SOIMUMPs27 glued devices.

2.7.2.2.3 Effect of Actuator Interference in Sensing and Verification of Glue Insulation

Further investigation was done regarding the interference of actuation voltage in the sensing component and to verify the epoxy glue insulation properties. A SOIMUMPs27 device was used without any specimen or glue across gap. The capacitance change was measured for varying driving voltages for the device. As expected, no capacitance change was observed; in the absence of any specimen, load sensor does not experience any deflection and consequently no capacitance change is observed. However electrically

connecting both sides of the gap (see Fig. 2.36, pads 1 and 2 are electrically connected), results in a significant capacitance change with driving voltage even in the absence of actuator deflection (Fig. 2.37). So, the actuator and sensing must be electrically insulated for reliable capacitance change measurements.

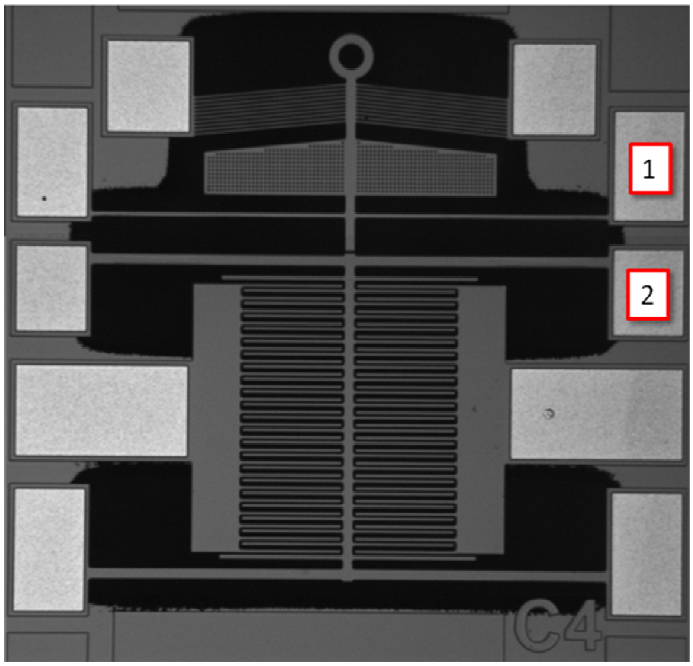

Figure 2.36: Pads 1 and 2 of SOIMUMPs27 that electrically connected for investigating electrical interference in sensing due to actuator.

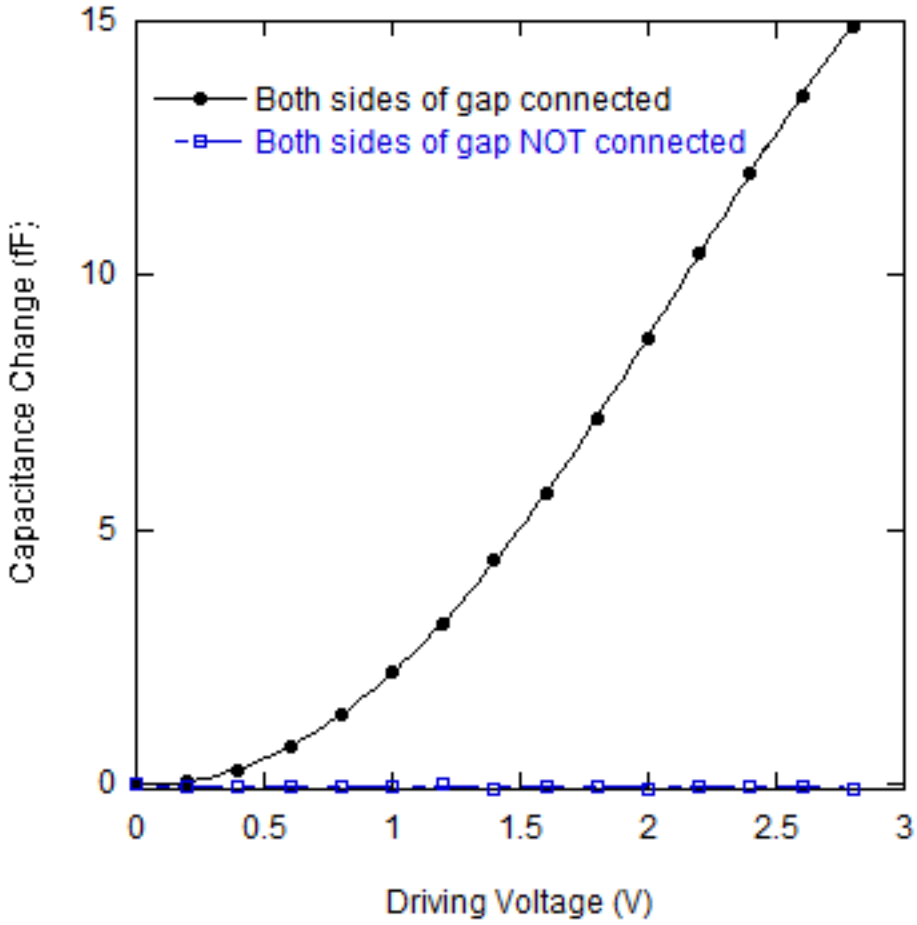

Figure 2.37: The effect of electrical interference in sensing from the actuator. Capacitance change was measured with varying driving voltages for a SOIMUMPs27 device (without any specimen or glue across gap) upon electrically connecting both sides of the gap. Ideally no capacitance change should be measured (in absence of electrical interference from actuator).

Since the driving voltage in the actuator causes interferences in the sensing component resulting in erroneous capacitance change measurements, it becomes extremely important to verify the electrical insulation of the epoxy glue used. This is to ensure that the capacitance change measured is in fact due to the load sensor deflection only and not due to applied driving voltage.

A glued SOIMUMPs24 device was used for verification of electrically insulating properties of epoxy glue. Instead of a potential difference across the actuator beams, a

bias voltage was applied to only one of the actuator pads to study the effect of this varying bias actuator voltage on sensing. Since no potential difference across the actuator beams is applied, no current flows though the actuator beams, and consequently no actuator and load sensor deflections are achieved. In the absence of electrical interference from the actuator, no capacitance change should be obtained due to the absence of load sensor deflection. No capacitance change was observed with varying bias voltage to actuator (Fig. 2.34) thus verifying the electrical insulation achieved using epoxy glue. Hence, the capacitance change obtained using glued devices can be safely considered to be a true reflection of the load sensor deflection.

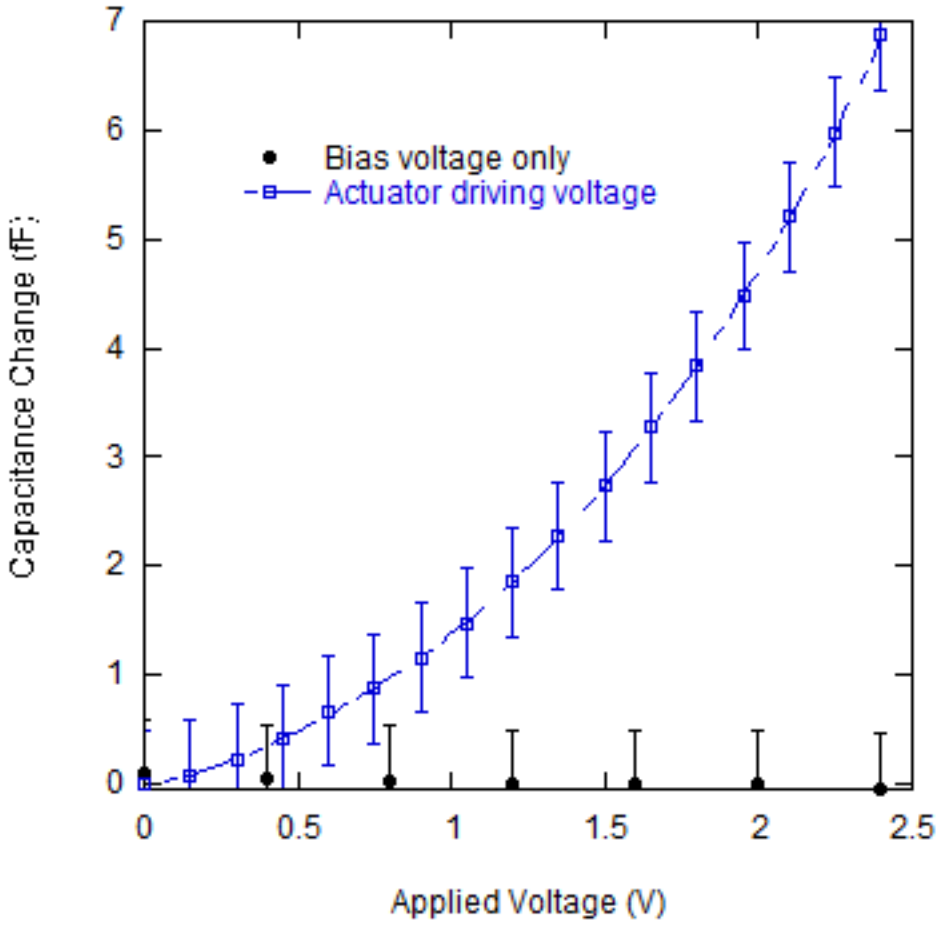

Figure 2.38: The effect of varying bias voltage on the capacitance in absence of load sensor deflection, compared to the capacitance change due to load sensor deflection for applied actuator driving voltage for a glued SOIMUMPs24 device.

2.7.2.2.4 Capacitance Change with Load Sensor Deflection

The load sensor design was identical for both SOIMUMPs24 and SOIMUMPs27. Consequently the same capacitance change would be expected for both for the same load sensor deflection.

Optical calibration curves as well as capacitance characterization plots for glued devices were used to determine the capacitance change as a function of load sensor

deflection. The capacitance change variation with load sensor deflection (actuator deflection ~ load sensor deflection for glued devices) was found to be in good agreement for both SOIMUMPs24 and SOIMUMPs27 (Fig. 2.39).

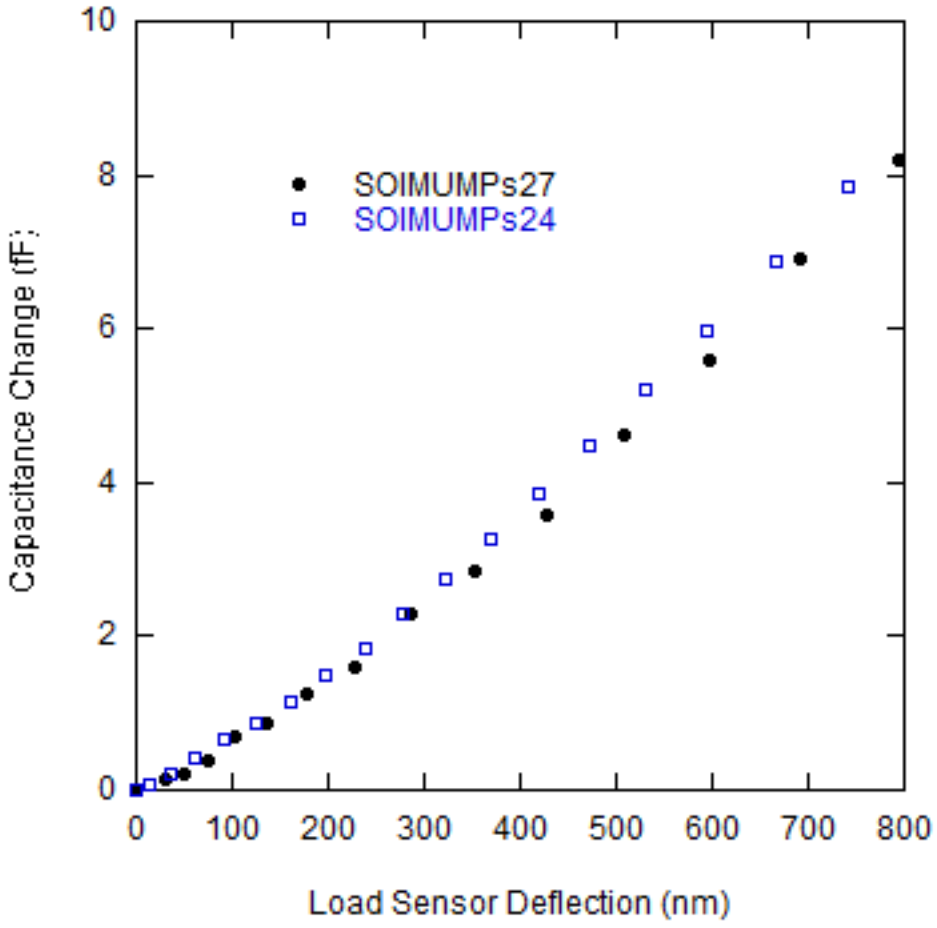

Figure 2.39: Capacitance change variation with load sensor deflection for both SOIMUMPs24 and SOIMUMPs27.

For a typical tensile test, the load sensor deflection can consequently be calculated from the measured capacitance change using the above characterization plots (Fig. 2.39). This can further be used to calculate the specimen stress and elongation (refer Section 2.2).

A precision of ~5nm in terms of load sensor deflection was achieved using the developed methodologies (refer Appendix B). However, only one side of the load sensor was actually utilized in the discussed experiments. Higher resolution could be achieved by utilizing both sides of the load sensor (twice the capacitance change for the same deflection).

It was observed that due to the extremely small value for the feedback capacitor (C_F), there could be significant errors in the absolute value of C_F and consequently the absolute values of the capacitance change measured (refer Appendix B for detailed discussions). This resulted in a constant scaling factor (~2.5, see Figs. 2.6 and 2.39) for the measured capacitance change as compared to the actual values. To address this issue, the same feedback capacitor C_F was used throughout the study.

2.8 Finite Element Modeling

Finite element modeling (Ansys 12.0.1) was used to numerically analyze the various components of the MEMS nanotensile tester and compare with the experimental results presented in sections 2.4, 2.5 and 2.6.

2.8.1 Actuator

A 3D model was developed for the actuator and a coupled electrical-thermal-structural (multiphysics) analysis was done to determine the actuator deflections as well as temperatures achieved at different locations for varied applied driving voltages.

2.8.1.1 Geometry

The actuator consists of a 10 micron thick doped single crystal silicon structural layer. Surface doping results in a resistivity variation along the depth of silicon layer. To capture this behavior the silicon structural layer was modeled with two different layers. The bottom layer was assumed to be N-type bulk silicon layer with a resistivity of 10 ohm-cm (refer Table 2.1). The top layer was assumed to be highly doped silicon and the resistivity of the layer for a particular layer thickness was calculated based on the total actuator resistance measured experimentally (typical value for actuator resistance ~ 100 Ω).

The 500 micron thick air cushion between the device and the substrate was modeled to account for conductive heat transfer through the air to the substrate below. Furthermore, convective heat transfer was also modeled for air around the actuator. The FE model for the actuator is shown in Figs. 2.40 to 2.42. Due to symmetry only half the actuator was modeled to decrease the computational time.

2.8.1.2 Material Properties

The model for the actuator consists of three different materials:

(a) Top highly doped silicon layer (low resistivity)

(b) Bottom silicon layer with high resistivity

(c) Air around the actuator

The stiffness matrix for Si (100) is given in Table 2.3. However since the device is oriented along the <110> direction on (100) plane, the local coordinates for the two single crystal silicon layers (anisotropic) were defined at 45° to global coordinates.

Table 2.3: Stiffness Matrix for Silicon (100) (Courtesy Chang et. al. [57])

$$\mathbf{C}_{(100)} = \begin{bmatrix} C_{11} & C_{12} & C_{12} & 0 & 0 & 0 \\ C_{12} & C_{11} & C_{12} & 0 & 0 & 0 \\ C_{12} & C_{12} & C_{11} & 0 & 0 & 0 \\ 0 & 0 & 0 & C_{44} & 0 & 0 \\ 0 & 0 & 0 & 0 & C_{44} & 0 \\ 0 & 0 & 0 & 0 & 0 & C_{44} \end{bmatrix}$$

$$C_{11} = 165.7 \text{ GPa}, \quad C_{12} = 63.9 \text{ GPa}, \quad C_{44} = 79.6 \text{ GPa}.$$

The coefficient of linear thermal expansion and thermal conductivity of silicon shows a temperature dependent behavior which was included in the model. The thermal expansion and thermal conductivity used for the two silicon layers are given in Table 2.4.

Table 2.4: Variation of coefficient of linear thermal expansion α and thermal conductivity k_t with temperature. (Courtesy Mankame et. al. [58])

Temperature (K)	k_t (W m^{-1} K^{-1})	α (μm m^{-1} K^{-1})
300	146.4	2.568
400	98.3	3.212
500	73.2	3.594
600	57.5	3.831
700	49.2	3.987
800	41.8	4.099
900	37.6	4.185

Thermal conductivity of air used was 0.026 W m^{-1} $°C^{-1}$ (refer Huang et. al. [59]). Convection heat transfer coefficients for air were varied between 10 - 100 W m^{-2} K^{-1} (refer Mankame et. al. [58]) and their effect was studied.

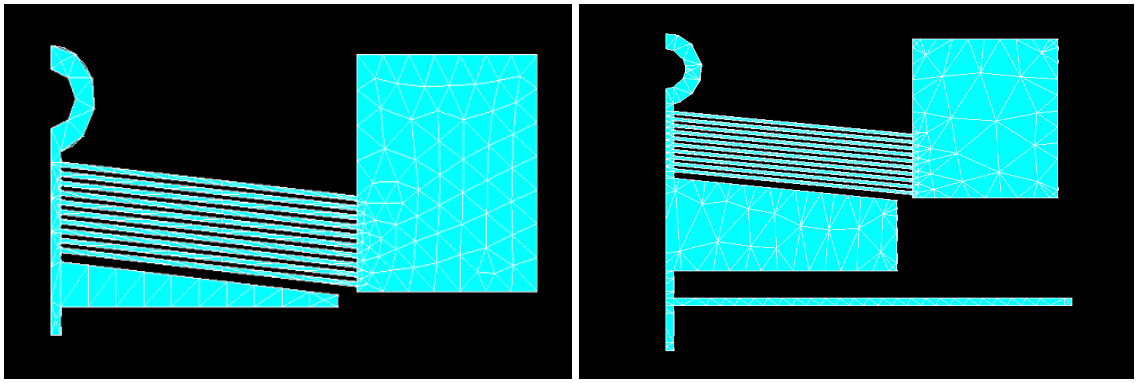

(a) (b)

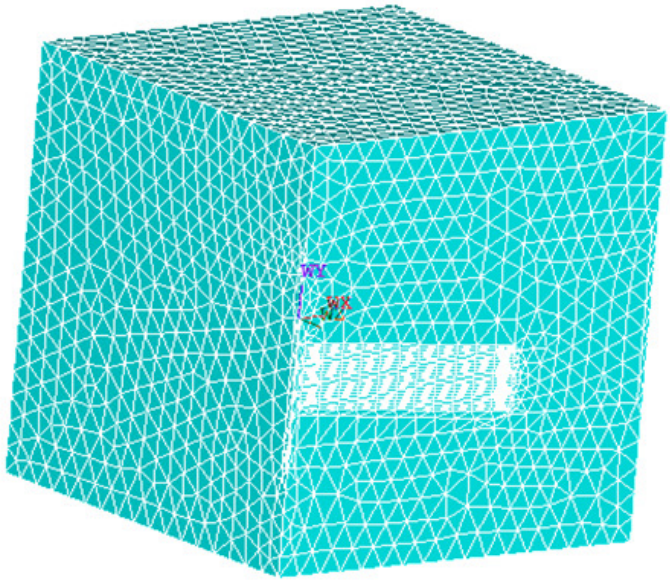

(c)

Figure 2.40: Finite element model for (a) SOIMUMPs24 (b) SOIMUMPs27 (c) Actuator modeled with air around it.

2.8.1.3 Boundary Conditions

Boundary conditions were required for each of the three domains: electrical, thermal, and structural. It was assumed that the device could be modeled symmetrically. At the symmetry plane the displacement and heat flow normal to the symmetry plane acted symmetrically, while the voltage was taken to be zero for the actuator. In addition, for the electrical domain, the voltage was set to $V_{total}/2$ on the actuator pad modeled. For the thermal domain, it was assumed that the temperature on the actuator pad was set at room temperature (298 K) along with the lower face of the modeled air block (substrate). All the displacements were set to zero on the actuator pad and the stiffness beam pad for the structural boundary.

2.8.1.4 Element Type

A multiphysics analysis including the three domains: electrical, thermal and structural was required and consequently SOLID227 elements were used for meshing the model for a coupled analysis.

2.8.1.5 Results

Actuator deflection was determined for various applied actuator driving voltages, using the finite element model discussed (Fig. 2.41). Also the temperature achieved near the specimen was determined for an applied 3V driving voltage (Fig. 2.42). Mesh convergence was done for both actuator deflection and temperatures obtained near the specimen (see Figs. 2.43 and 2.44).

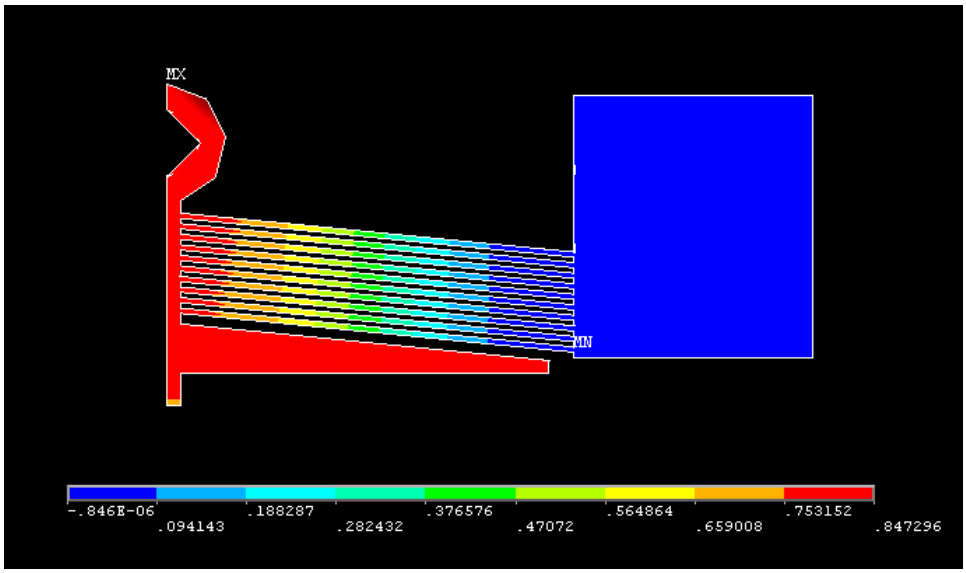

(a)

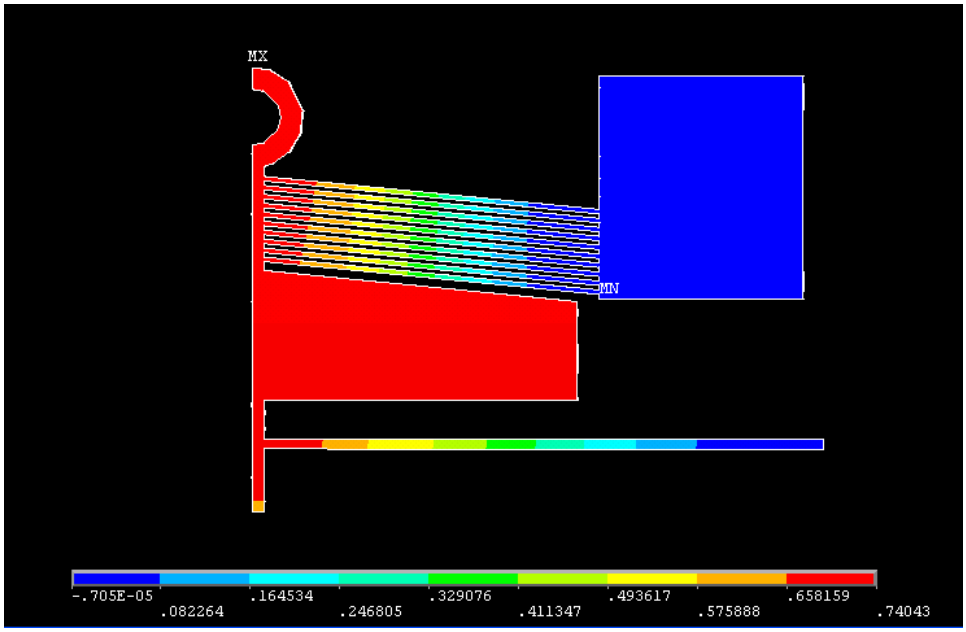

(b)

Figure 2.41: Shows the actuator deflection (in microns) profile obtained for an applied 3V driving voltage for (a) SOIMUMPs24 (b) SOIMUMPs27.

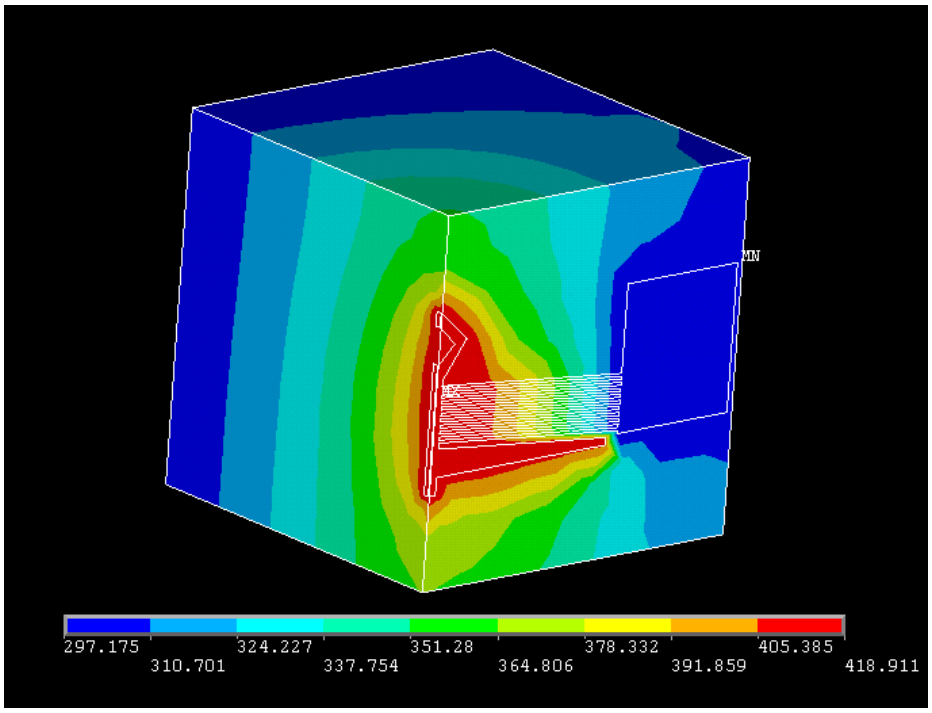

(a)

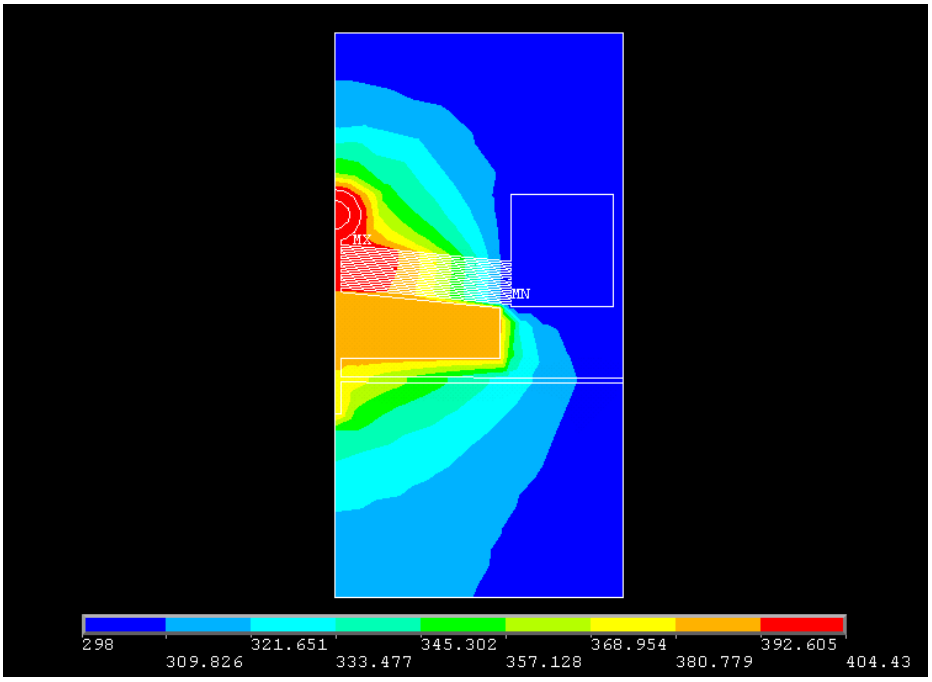

(b)

Figure 2.42: Shows the temperature (in K) profile obtained for an applied 3V driving voltage for (a) SOIMUMPs24 (b) SOIMUMPs27. The room temperature was assumed to be 298K.

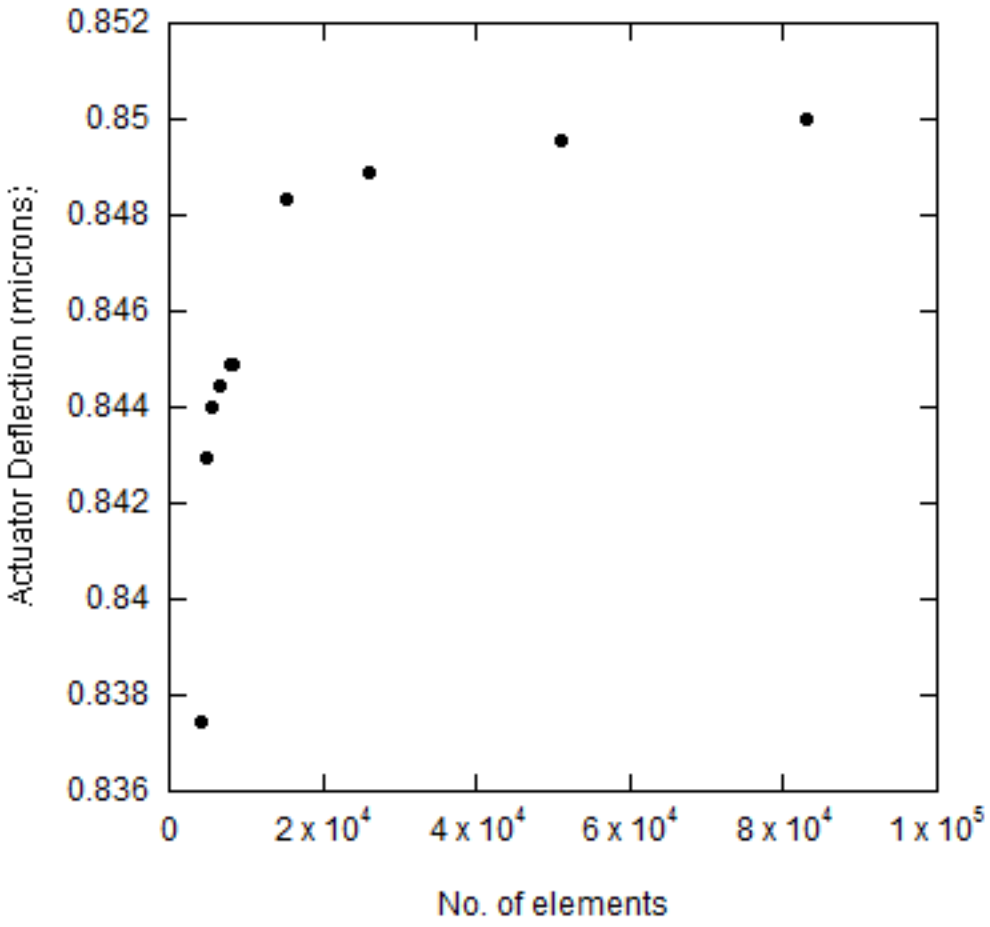

Figure 2.43: Mesh convergence for actuator deflection for SOIMUMPs24 design for an applied 3V driving voltage.

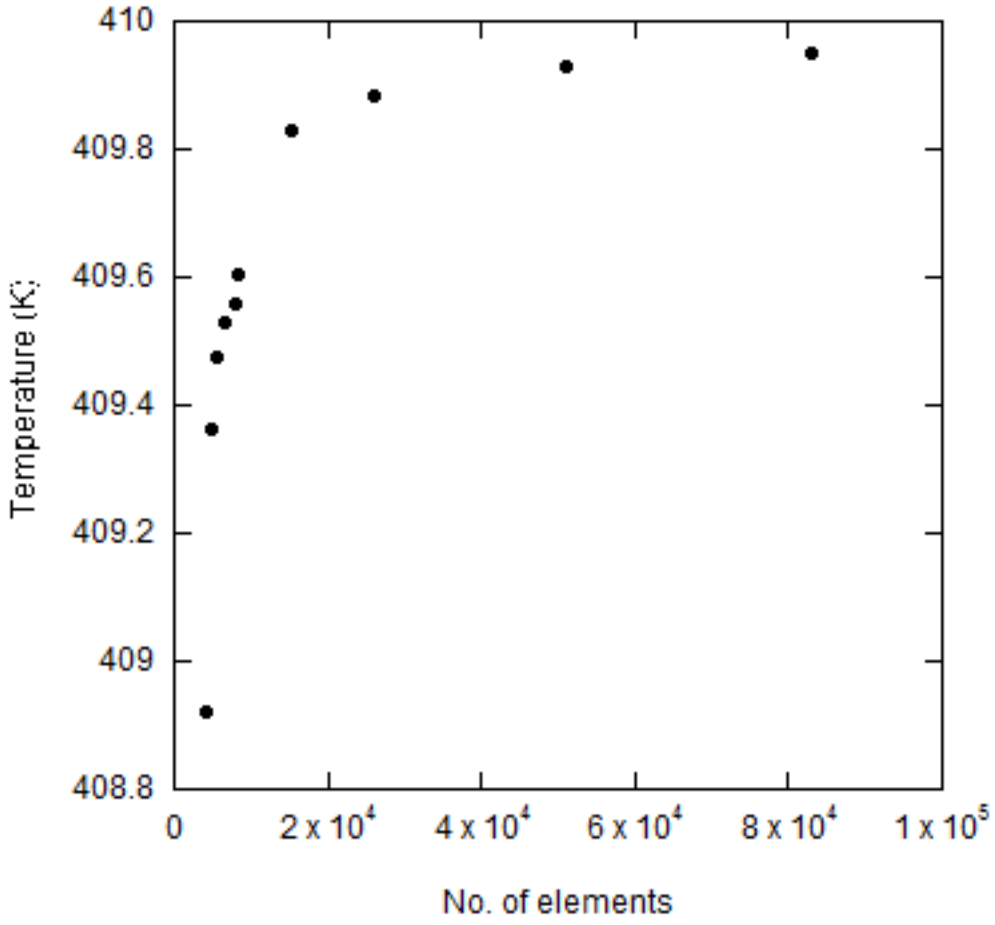

Figure 2.44: Mesh convergence for temperatures near the specimen for SOIMUMPs24 design for an applied 3V driving voltage. Room temperature was assumed to be 298 K.

Here, the top highly conductive doped silicon layer was assumed to be 2 microns thick. However variation of this doped layer thickness resulted in less than 1% variation in the actuator deflection. The resistivity of the highly doped top layer had to be recalculated from experimental results depending on the top layer thickness assumed (the total actuator resistance was ~ 100 Ω.

Furthermore the variation of convective heat transfer coefficients for air from 10 - 100 W m^{-2} K^{-1} resulted in less than 5% variation in actuator deflection. Consequently it can be

inferred that convective heat transfer plays a less significant role for these devices as compared to conduction through silicon and air.

Finite element results for actuator deflection and temperatures obtained near the specimen show good correlation with the experimental results for both SOIMUMPs24 and SOIMUMPs27 (see Figs. 2.45 and 2.46).

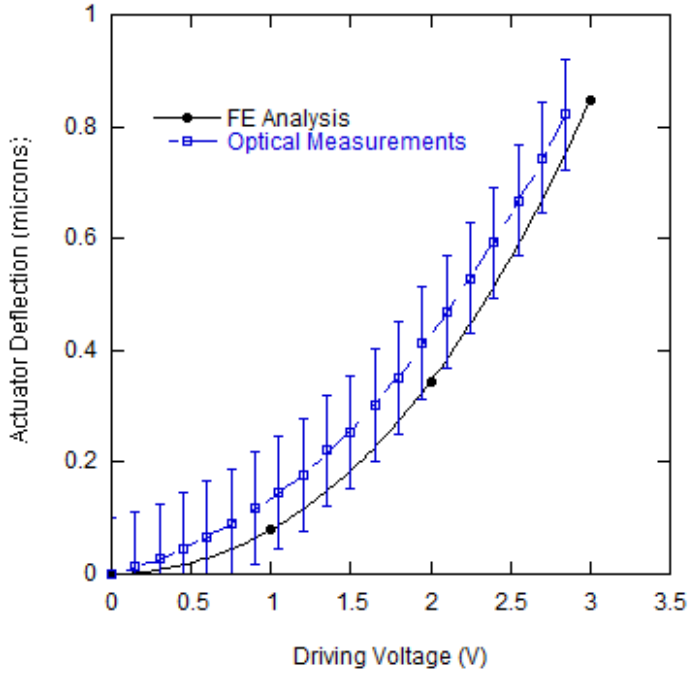

(a)

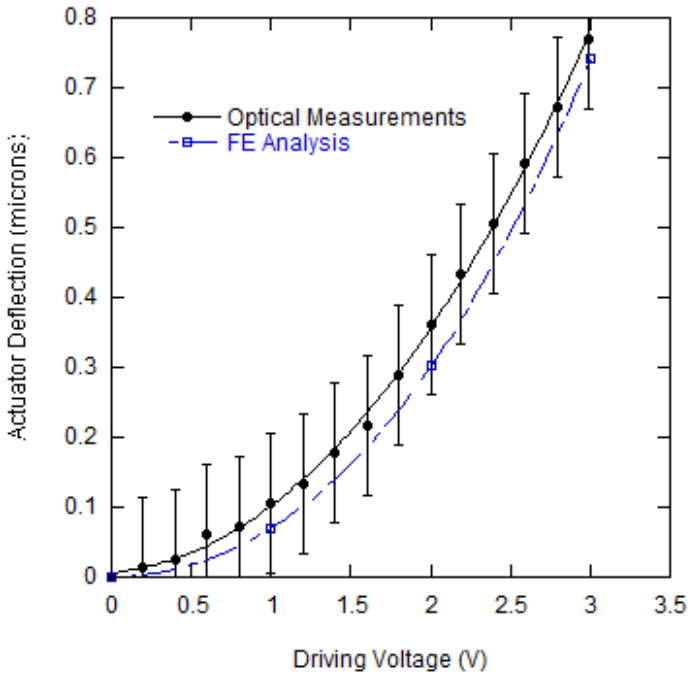

(b)

Figure 2.45: Comparison of the actuator deflections obtained experimentally (optically) as well as using finite element analysis for (a) SOIMUMPs24 (b) SOIMUMPS27.

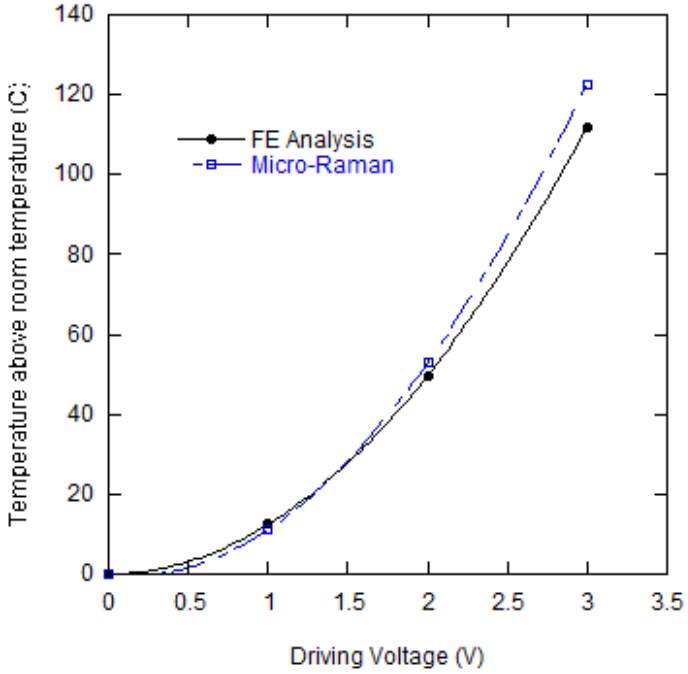

(a)

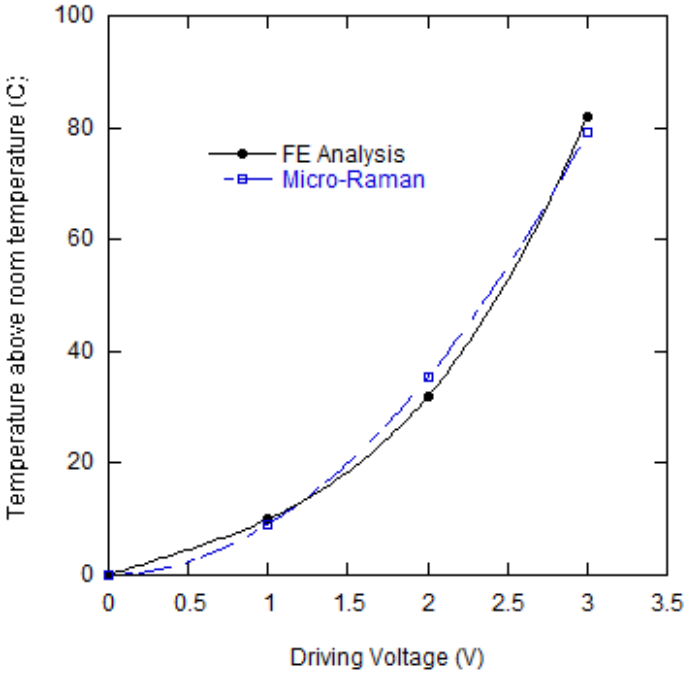

(b)

Figure 2.46: Comparison of the temperatures (above room temperature) achieved near specimen obtained using Micro-Raman as well as finite element analysis for (a) SOIMUMPs24 (b) SOIMUMPs27.

2.8.2 Load Sensor Stiffness Effect on Actuator Deflection

The effect of load sensor stiffness on the actuator deflection, during the tensile test of a specimen or for a calibration device, was investigated. It is important to ensure that the stiffness of the actuator is sufficiently large as compared to the load sensor, so that the load sensor stiffness does not affect the actuator deflection during a nanotensile test. For this a calibration device was modeled (Fig. 2.47) i.e. the load sensor was connected to the actuator and the actuator deflection for this configuration was compared to actuator alone. Less than 1% change in actuator deflection (0.846 microns as compared to 0.85 microns) was observed for a 9 micron load sensor suggesting that the actuator stiffness is sufficiently large as compared to the actuator.

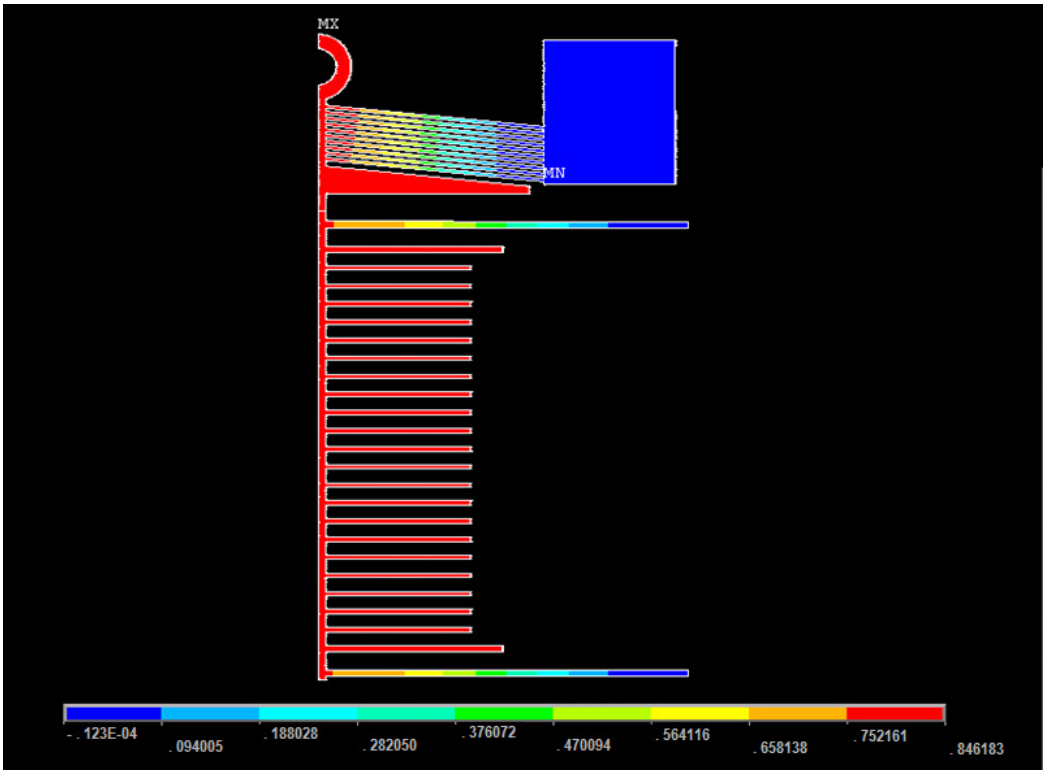

Figure 2.47: Deflection (vertical) profile for a 3V driving voltage, when the load sensor is attached to the actuator for SOIMUMPs24 device with 9 micron load sensor stiffness beams.

2.8.3 Load Sensor Stiffness

The load sensor stiffness beams were modeled using Ansys to characterize the load sensor stiffness behavior. The modeled 3D geometry is shown in Fig. 2.48. Since only the four stiffness beams contribute to the stiffness of the load sensor, the comb structures for capacitive sensing were excluded from the model to minimize computational time.

The mechanical properties of monocrystalline silicon were used to model the 10 micron thick structural layer of the load sensor. The stiffness matrix for Si (100) is given in Table 2.3. However since the device is oriented along the (110) direction on (100) plane, the local coordinates for the two single crystal silicon layers (anisotropic) were modeled at 45° to global coordinates. SOLID 187 element type was used for meshing the structure. The fixed ends of the load sensor stiffness beams were given a zero displacement boundary condition. The deflection obtained for a small applied force to the actuator was used to calculate the stiffness of the load sensor. A typical deflection profile of the load sensor has been shown in Fig. 2.49. Mesh refinement was done until convergence of the results was achieved (see Fig. 2.50). The results for stiffness of the 9 µm load sensor using FE (~ 39 N/m) was found to be in good agreement (see Section 2.6) with experimental results (~ 36 N/m).

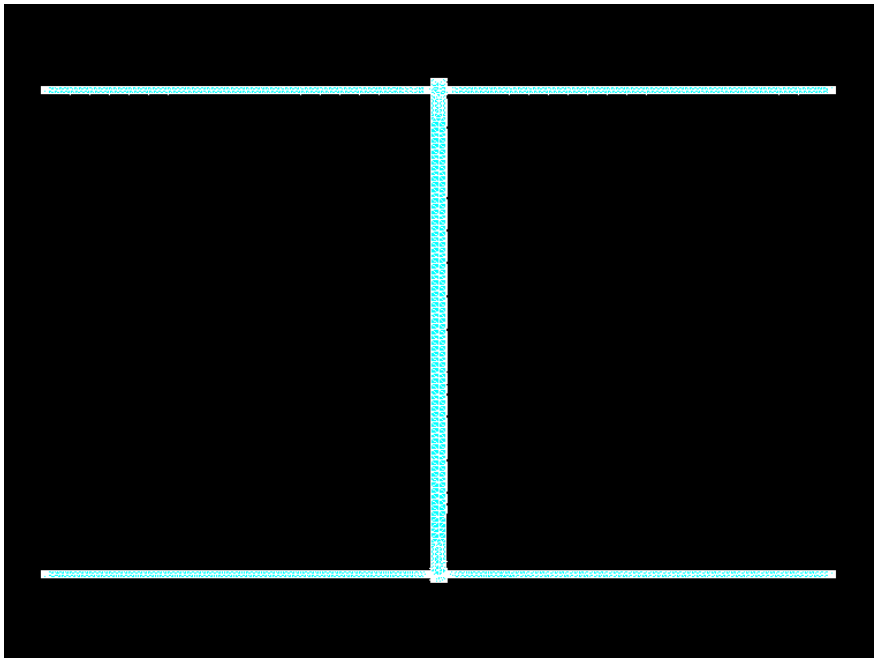

(a)

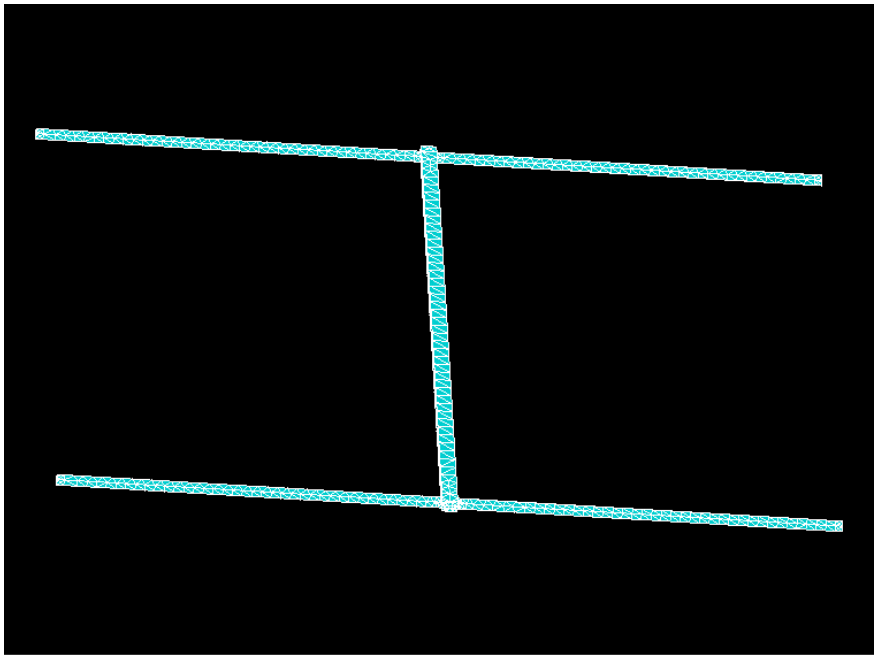

(b)

Figure 2.48: Geometry and meshing for the modeled load sensor (9 micron stiffness beams) (a) Top view, (b) View at an angle

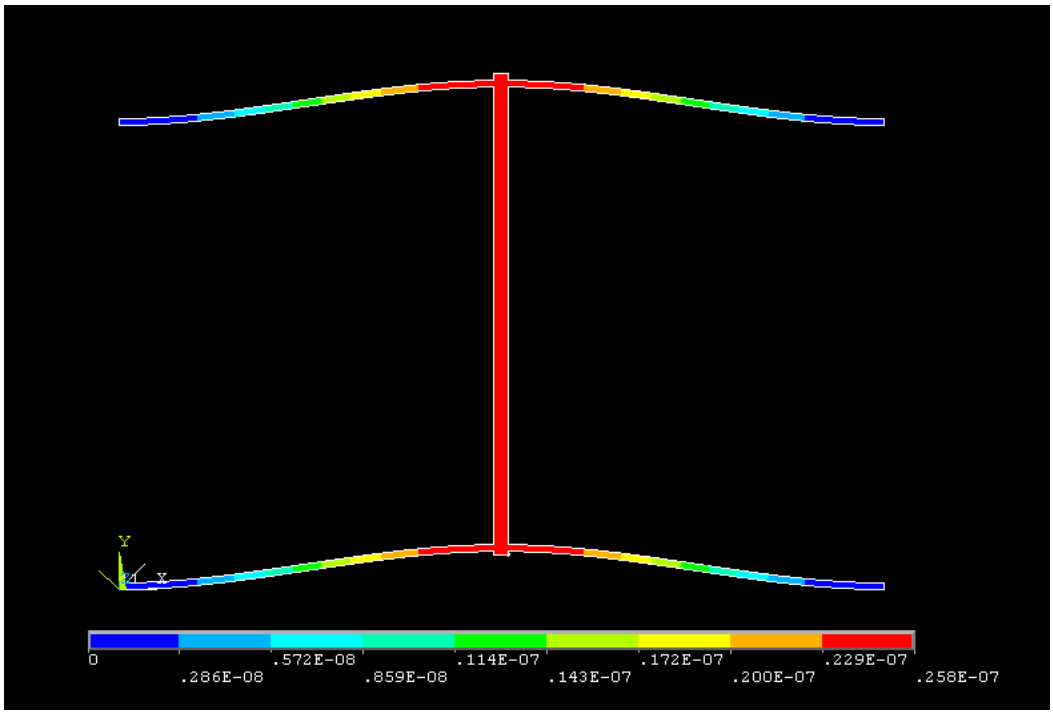

Figure 2.49: Load sensor deflection profile (values in meters) for an applied vertical force of 1 μN along the plane of symmetry for a 9 micron stiffness beam.

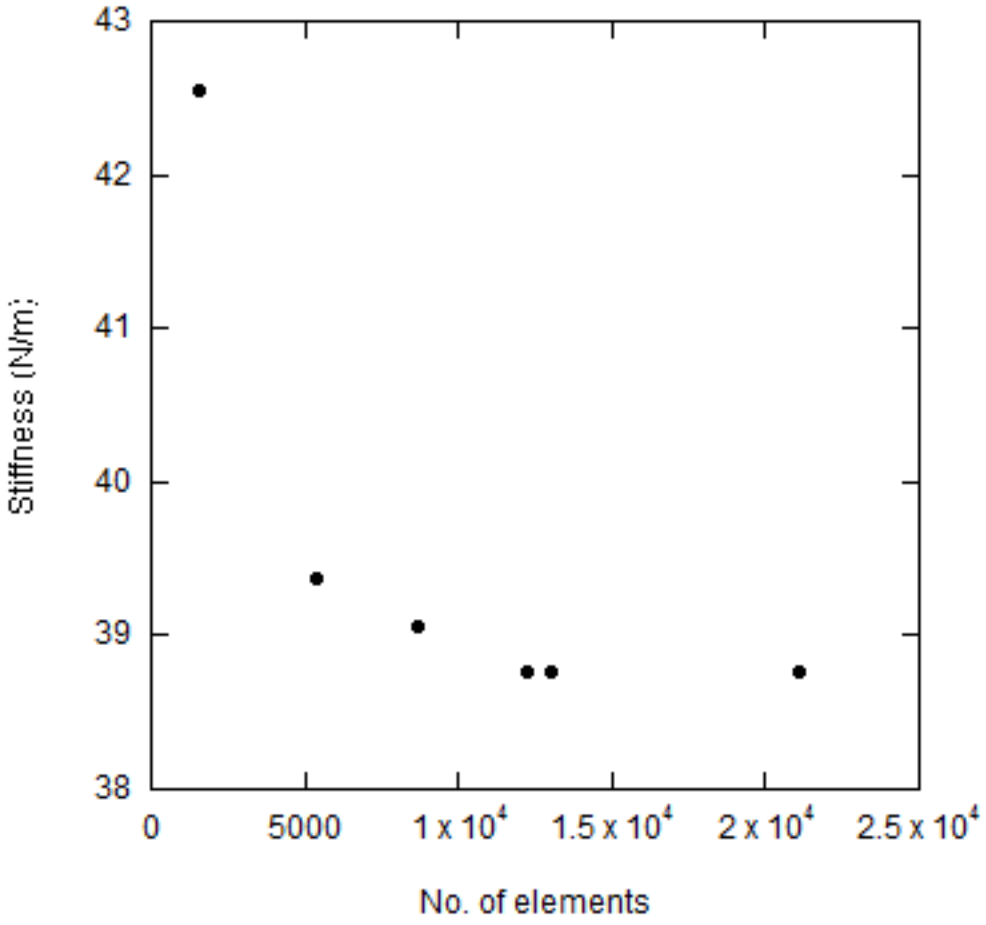

Figure 2.50: Mesh convergence for a 9 micron load sensor beam (10 micron thick structural layer) for small deflections (~30 nm).

2.8.3.1 Non-linear Effects of Load Sensor Stiffness for Large Deflections

The effect of large deflections (using NLGEOM function in Ansys) on the load sensor stiffness was investigated to ensure accurate force calculations for specimen testing. No significant effect of the load sensor stiffness was observed for large deflections for typical maximum deflection values of 1 micron (see Figs.2.51 to 2.54). However higher deflection may require the necessary stiffness value corrections for accurate stress measurements.

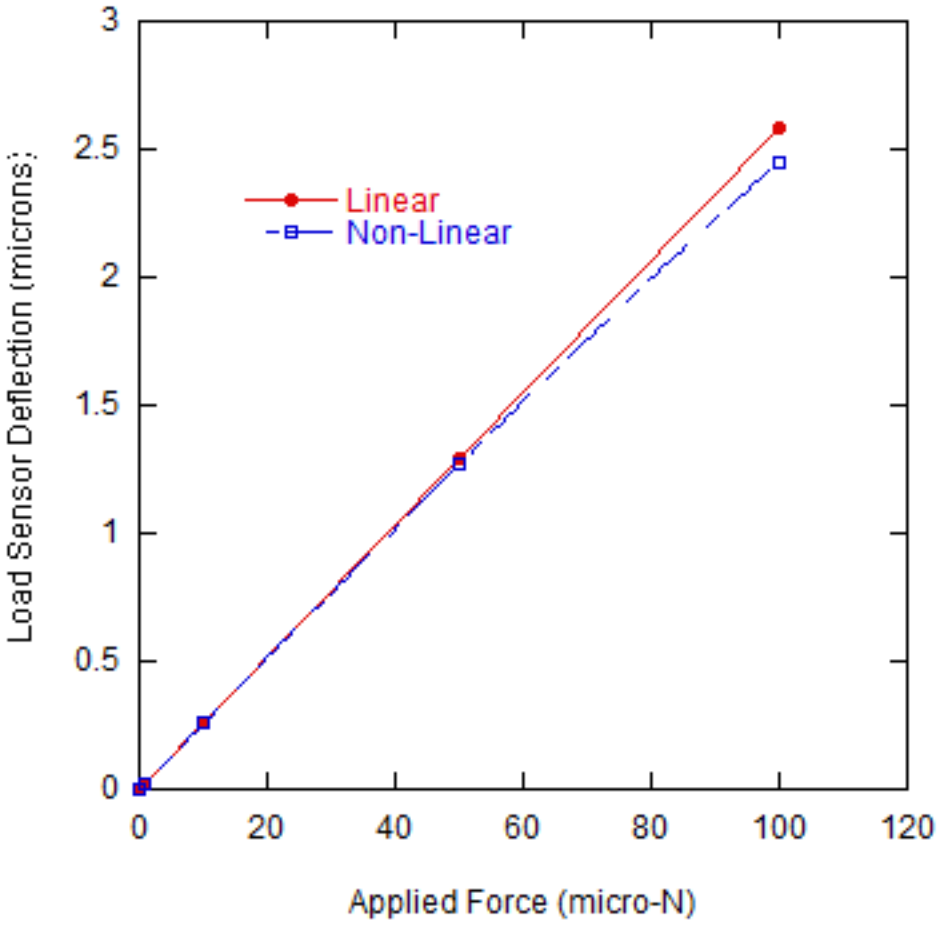

Figure 2.51: Non-linear (large deflection) effects on the deflection of the load sensor for various applied forces for a 9 micron stiffness beam.

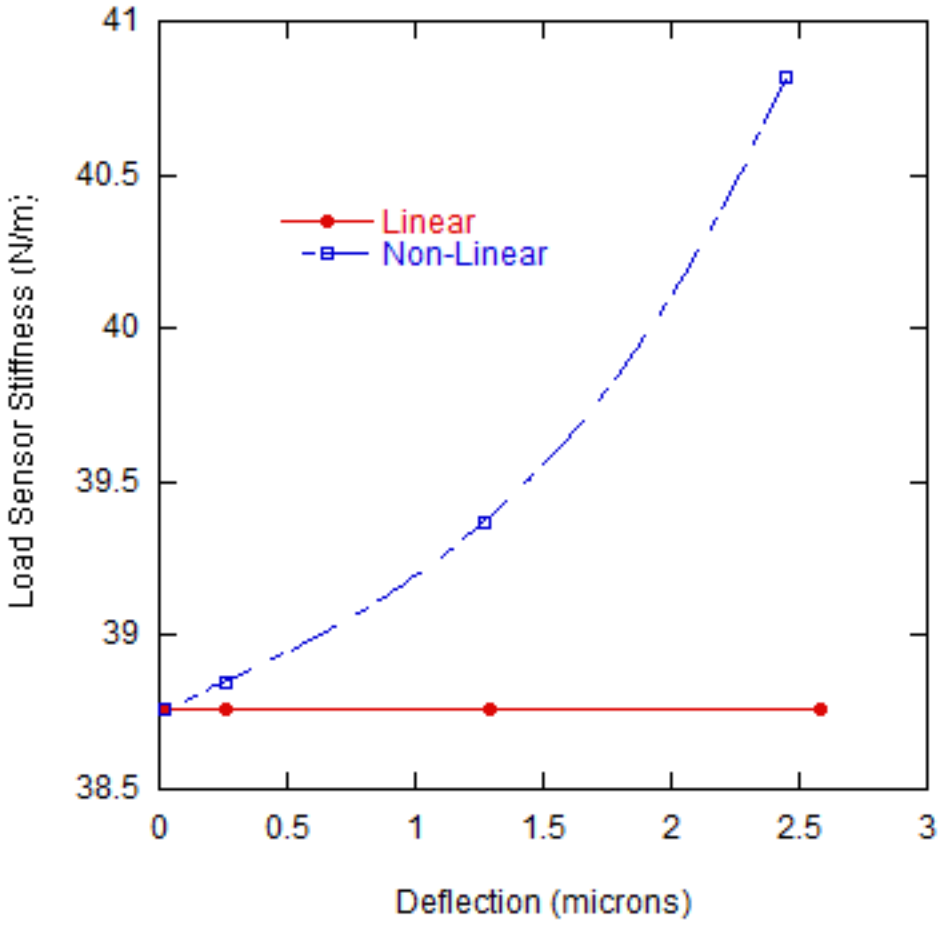

Figure 2.52: Non-linear (large deflection) effects on the load sensor stiffness variation with deflection for a 9 micron stiffness beam.

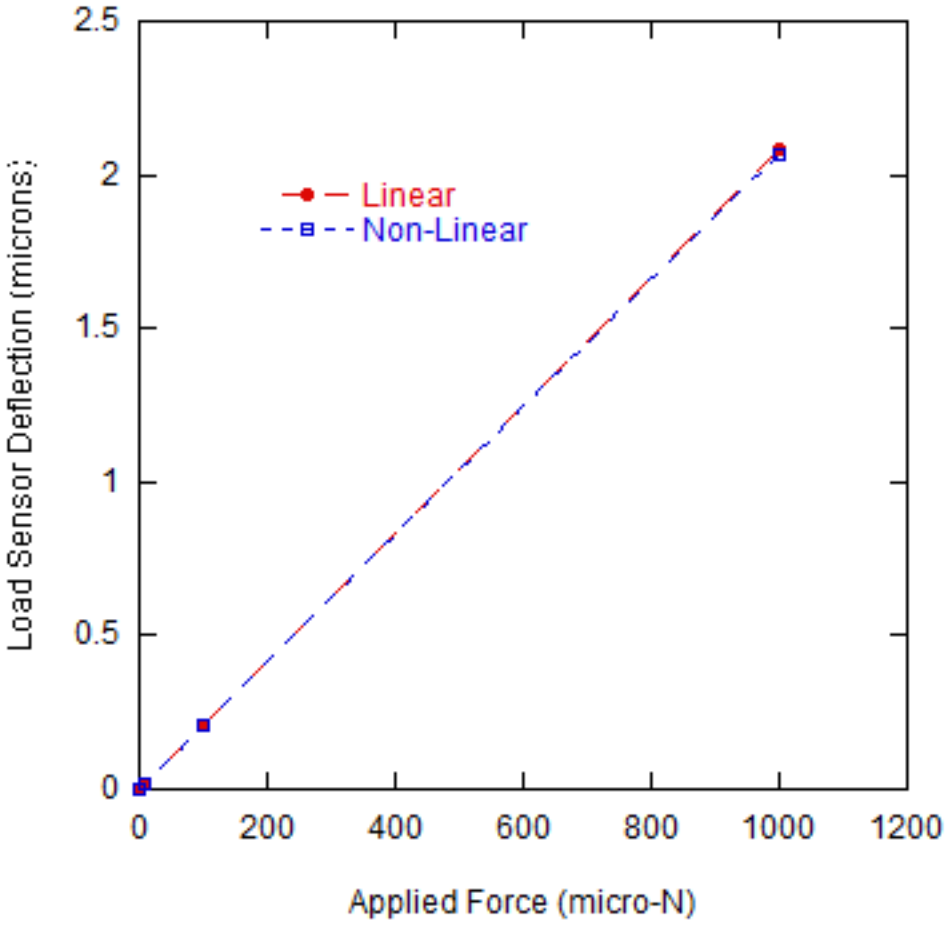

Figure 2.53: Non-linear (large deflection) effects on the deflection of the load sensor for various applied forces for a 21 micron stiffness beam.

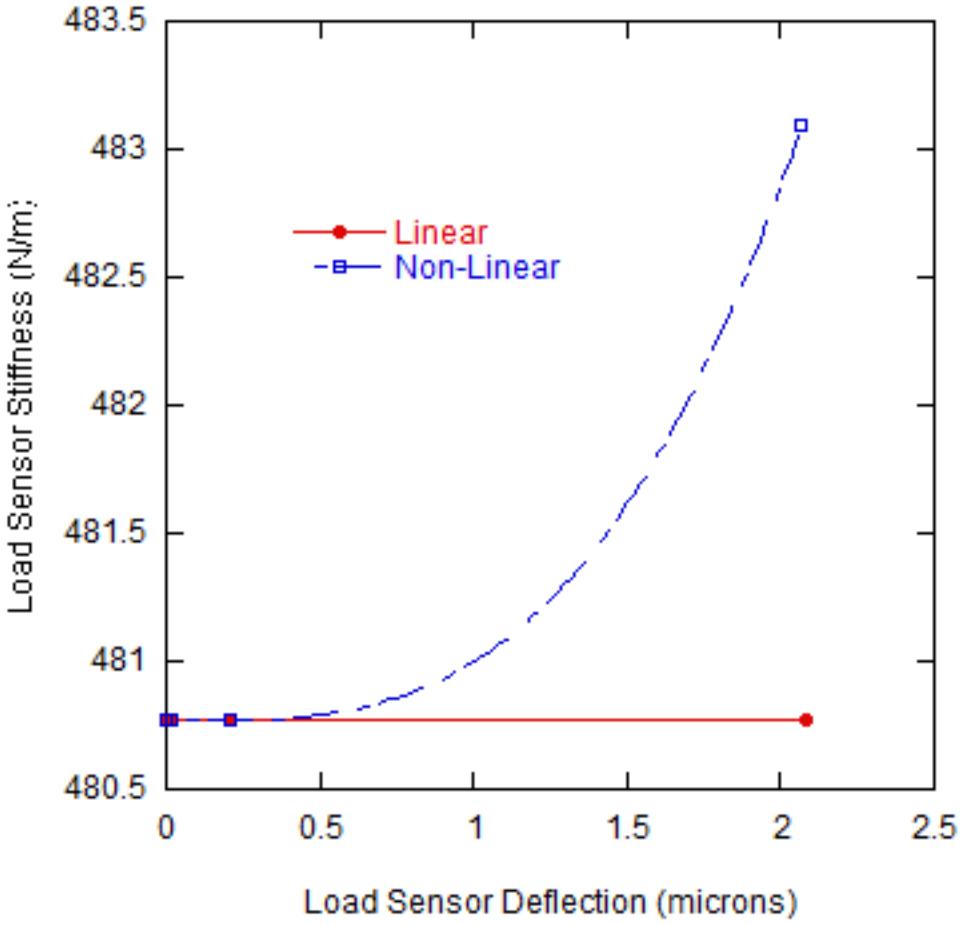

Figure 2.54: Non-linear (large deflection) effects on the load sensor stiffness variation with deflection for a 21 micron stiffness beam.

CHAPTER 3

MECHANICAL TESTING OF NANOSTRUCTURES

3.1 Introduction

This chapter deals with the actual tensile testing of nanostructures using the MEMS devices described in Chapter 2. Attempts were made to test two types of nanostructures – brittle Si nanowires and Ni nanobeams. Nano-tensile testing requires manipulation of nanostructures over the specimen gap which proves to be extremely challenging specially for brittle Si nanowires. An efficient procedure for such manipulation involving fabricated Ni nanobeams was developed (refer Section 3.3). Furthermore testing of conductive nanostructures using capacitive sensing was hampered by issues involving burning of nanostructures due to electrical coupling between the actuator and sensing. However observations regarding plastic deformations for nanocrystalling (NC) Ni nanobeams were made using these devices. Improved MEMS devices (discussed in Chapter 4) should allow proper tensile testing of such nanostructures using capacitive sensing. This improved design is also expected to resolve issues regarding variation of specimen temperature during the testing process.

3.2 Fabrication of Nanostructures

Ni nanobeams with different dimensions were fabricated (courtesy Eva Baumert). First the Si substrate was spin coated with positive resist PMMA A7 followed by E-beam lithography using JEOL JBX-9300FS EBL System. The photoresist was developed in MIBK:IPA 1:1 solution. E-beam evaporation using CHA evaporator was used to deposit

the required Ni thickness followed by lift-off using 1165 resist remover. Finally Xactix Xenon Diflouride Etcher was used to etch the Si underneath the Ni structures releasing the nanobeams. The final cantilevers obtained were fixed at one end to the substrate and free at the other end for efficient manipulation of the nanostructures over the MEMS devices (refer Section 3.3).

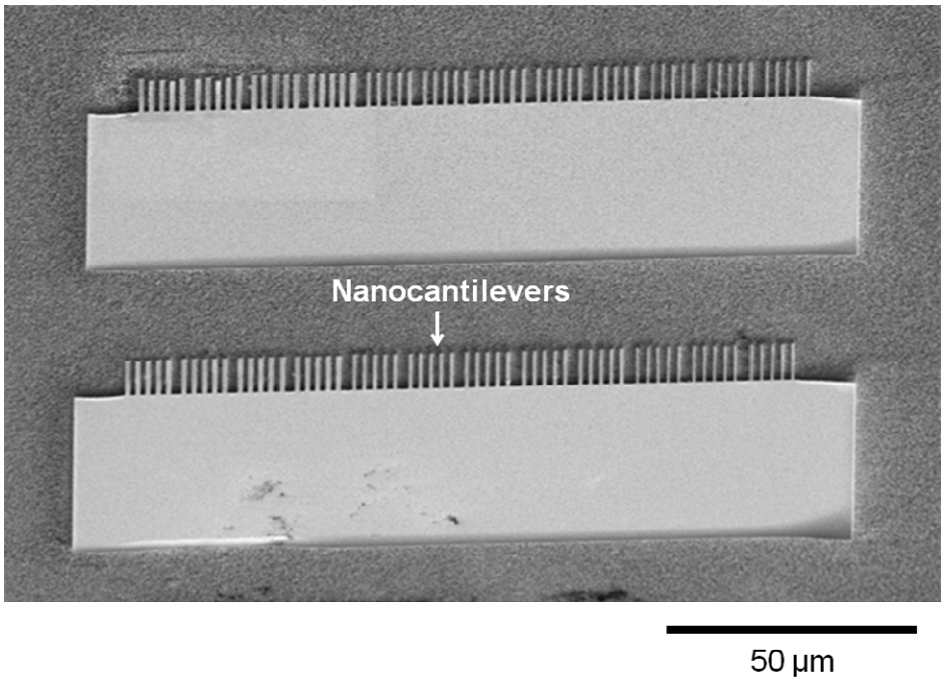

Figure 3.1: SEM image of the fabricated Ni nanobeams/nanocantilevers.

Two different lengths, 10 µm and 20 µm of the Ni nanostructures were fabricated. For each length size, two different nanobeam designs with cross-sectional dimensions 1000 nm x 500 nm and 550 nm x 250 nm were fabricated.

SEM imaging was done for the fabricated Ni nanobeams which were found to be nanocrystalline based on the grain size (see Fig. 3.2). The average grain size on the lower surface was approximately 40 nm while on the upper surface it was approximately 150 nm.

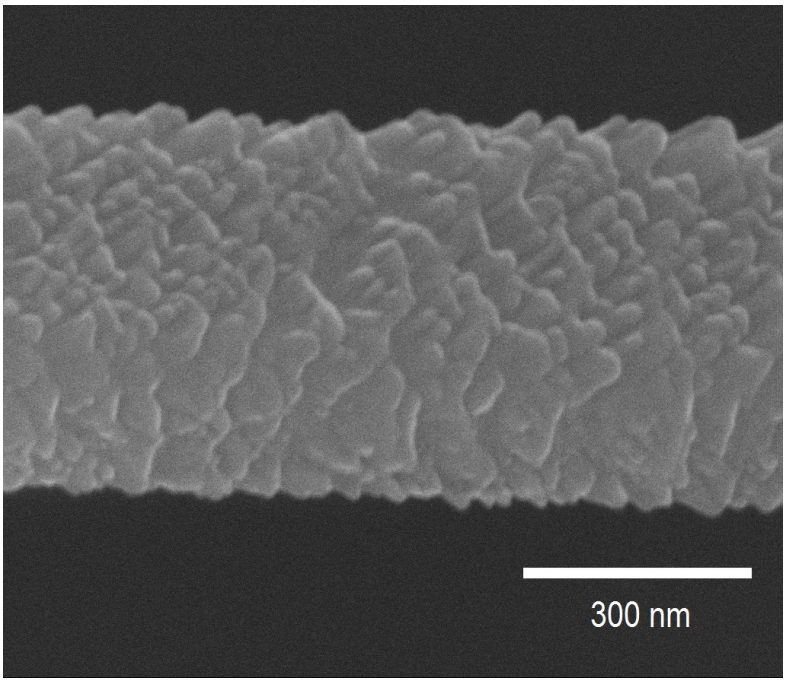

(a)

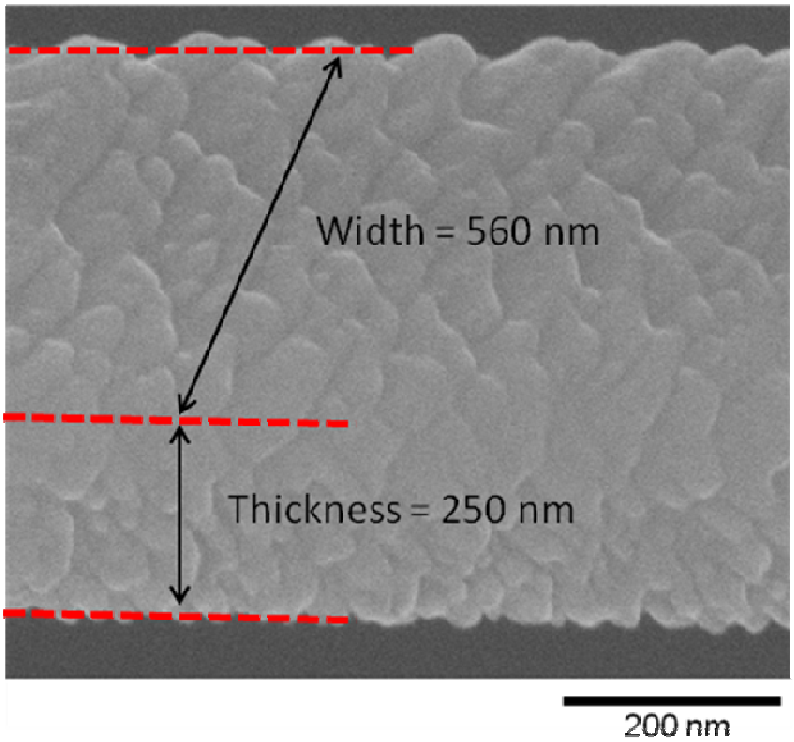

(b)

Figure 3.2: SEM images of the grain structure of the fabricated Ni nanobeams with 550±20 nm width and 250±50 nm thickness. The viewing angle of the image is 52° from the top.

Monocrystalline n-type doped Si nanowires (Fig. 3.3) tested were obtained from Illuminex Corporation and were fabricated using a VSL technique [60, 61, 62]. The diameters of the 20 µm long nanowires ranged from 30 nm – 300 nm.

(a)

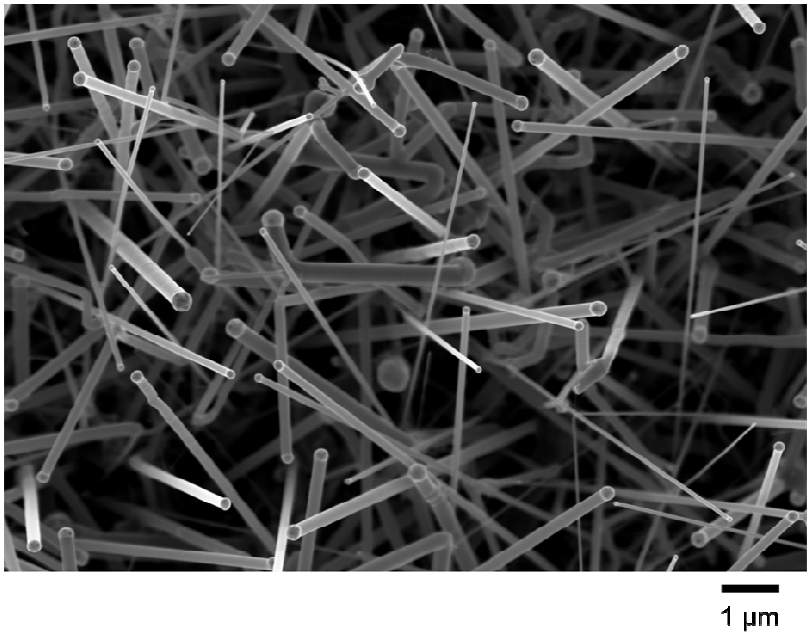

(b)

Figure 3.3: SEM images of the Si nanowires.

3.3 Manipulation of Nanostructures onto MEMS Devices

For nano-tensile testing, the specimen must be placed and clamped across the gap (see Fig. 2.2) of the MEMS devices.

The process requires the use of SEM (Scanning Electron Microscope), FIB (Focused Ion Beam), Micromanipulator and Pt deposition incorporated in the same system. FEI Nova Nanolab 200 FIB/SEM (Fig. 3.4) with GIS (Gas Injection System) for Ion Assisted Pt deposition module was used as the base system. Kleindeik Nanotehnik MM3A Micromanipulator (Fig. 3.5) was added to the Nova system for micromanipulation capability.

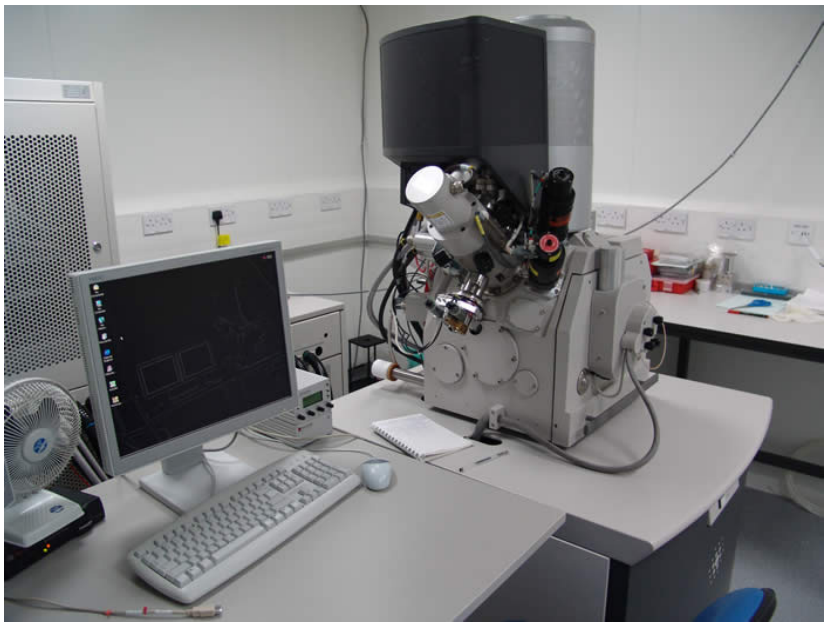

Figure 3.4: FEI Nova Nanolab 200 FIB/SEM system

Figure 3.5: Kleindeik Nanotehnik MM3A Micromanipulator system

It was observed that wirebonding process may cause nanowire failure even before the testing process (this problem may be more prominent for brittle materials like Si). Hence, it is important to wirebond the electrical pads on the MEMS device before the specimen manipulation.

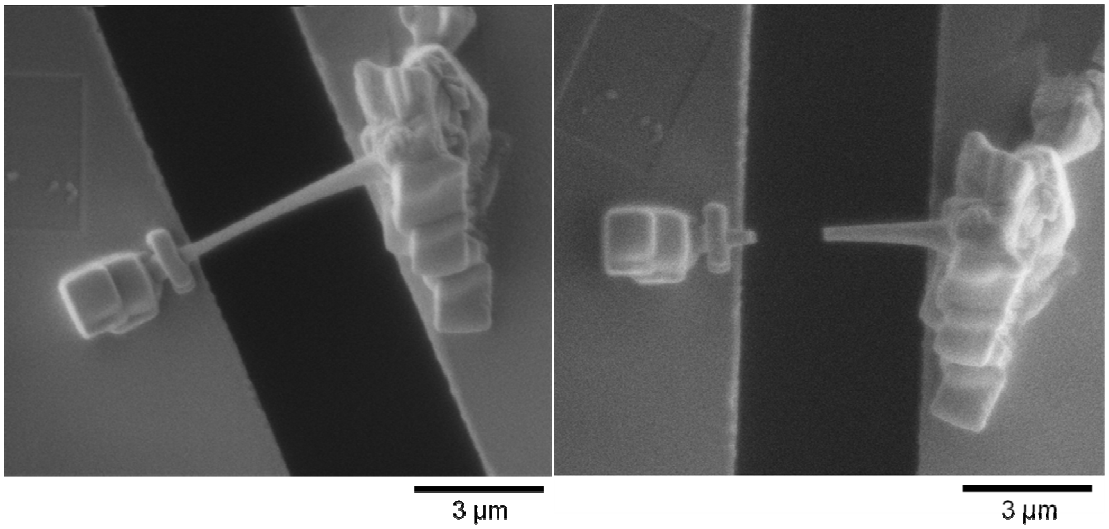

Figure 3.6: SEM image of a broken Si nanowire due to wirebonding. Left: Before wirebonding, Right: After wirebonding

FIB may result in Ga ion implantation as well as degradation of the surface of the nanowire during the imaging process itself. Hence care must be taken to avoid use of FIB

for imaging purposes. However it is necessary to have views from both e-beam as well as ion beam for positioning the nanostructure in 3D space. For such a case the lowest possible beam current must be used so as to minimize damage to the nanowire due to ion-beam.

3.3.1 Manipulation of Si Nanowires

The procedure for manipulation of Si nanowires has been illustrated in Fig. 3.7. Si nanowires were first attached to the micromanipulator tip using ion assisted Pt deposition. The nanowire was then aligned and positioned across the specimen gap of the MEMS device. This step requires extreme caution for successful placement of the nanowire. The micromanipulator must be positioned such that the Si nanowire almost touches the device surface. If hard contact is made between the nanowire and device surface, the contact force itself may be sufficient to break the extremely brittle Si nanowires in bending mode. Ion assisted Pt deposition was used to clamp one end of the nanowire. Lateral drift over time in the micromanipulator during or after the clamping process may also cause failure of the brittle Si nanowire in bending mode. However if the nanowire is positioned far above the MEMS surface, significant amount of Pt deposition is required for clamping. This results in seepage of deposited Pt along the length of the nanowire as well as increased risk of failure caused by micromanipulator drift due to increased deposition time. The other end of the nanowire attached to the micromanipulator tip is then milled off using FIB followed by clamping using Pt deposition.

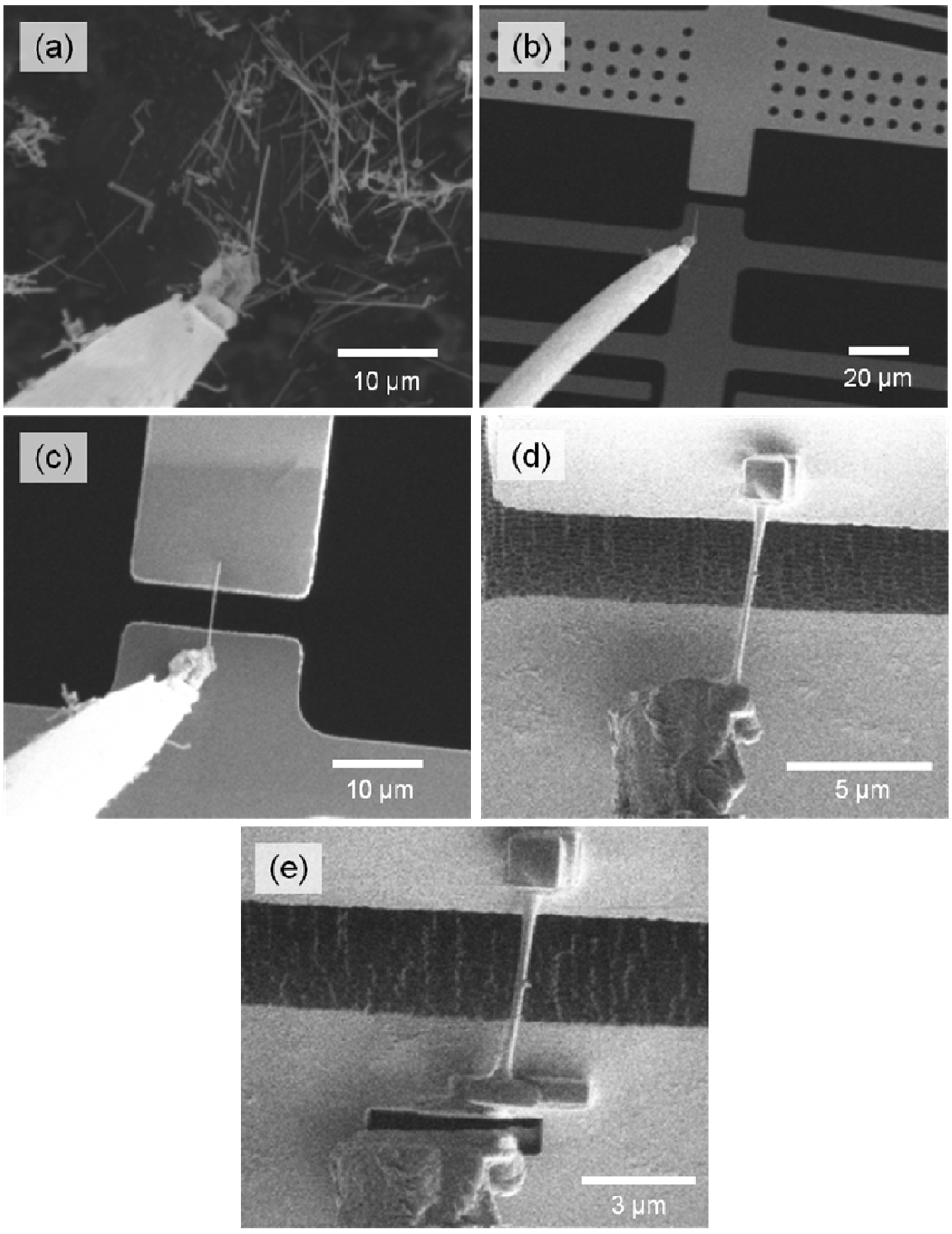

Figure 3.7: SEM images illustrating the procedure for manipulation of Si nanowires. (a) A Si nanowire attached to the micromanipulator tip using ion assisted Pt deposition (b) Micromanipulator tip with attached Si nanowire positioned over a MEMS device (c) Si nanowire being aligned and positioned across the specimen gap (d) Si nanowire clamped at one end using ion assisted Pt deposition (e) Nanowire detached from the micromanipulator tip using FIB and clamped at the other end using Pt deposition.

Apart from the difficulty in manipulation, Si nanowires were subjected to alignment issues (Fig. 3.8). Two types of misalignments namely horizontal and vertical are possible (refer Fig. 3.8). Horizontal misalignments can be minimized by rotation of MEMS device to align it along the length of nanowire. However due to the limitations in the degrees of freedom available in the micromanipulator, vertical alignments cannot be easily corrected. Due to the randomly placed nanowires on the surface it is difficult to pick up a perfectly horizontally aligned nanowire. It is difficult to correct this misalignment during nanowire placement due to the brittle nature of Si. Such misalignment can cause bending stresses in the nanowire during tensile loading in the nanowire resulting in erroneous results.

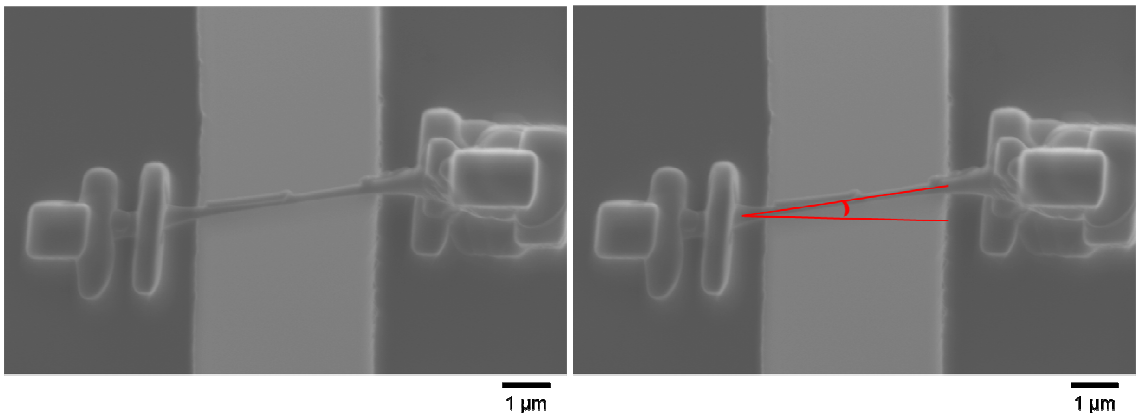

(a)

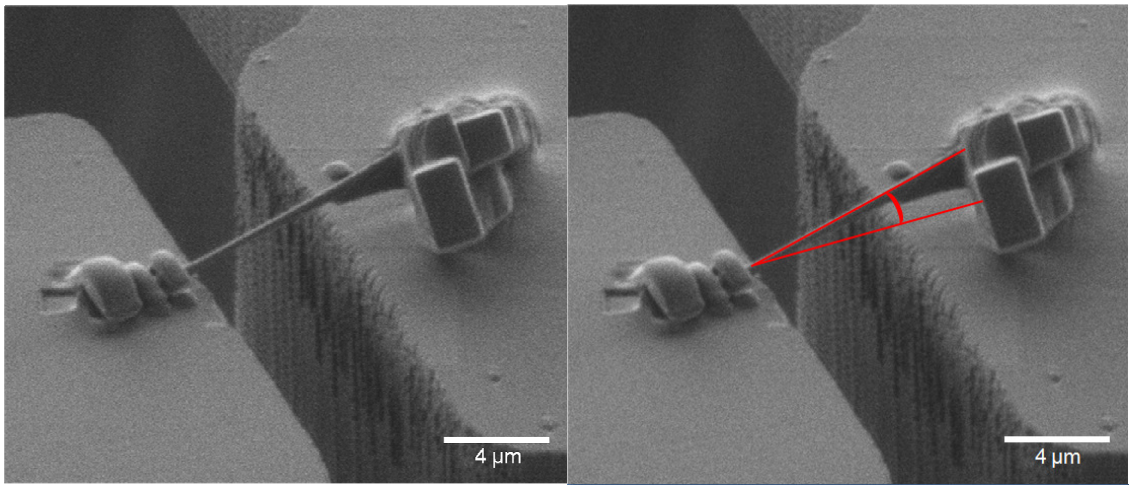

(b)

Figure 3.8: SEM image of a Si nanowire with misalignment (a) Top view - Horizontal misalignment (nanowire not aligned along the force direction) (b) View at 52° from top - Vertical misalignment (both the nanowire ends are not at the same horizontal level).

3.3.2 Manipulation of Ni Nanobeams

The fabricated Ni nanobeams are attached to the substrate at one end and free at the other. The micromanipulator tip is positioned to be in contact with the free end of the nanobeams (Fig. 3.9). Ion assisted Pt deposition is used to attach the micromanipulator tip to the free end of the nanobeam. The end attached to the substrate is milled off (see

Fig. 3.10) using FIB. The micromanipulator tip with the nanostructure (Fig. 3.11) is then positioned on the MEMS device across the specimen gap (Figs. 3.12 and 3.13). Ion assisted Pt deposition utilizing GIS (Fig. 3.14) is used to clamp the free end of the nanobeam on one side of the specimen gap (Fig. 3.15). The other end of the nanobeam is milled off using FIB (Fig. 3.16) and the micromanipulator tip is moved away (Fig. 3.17). Finally the other end of the nanostructure is also clamped using Pt deposition (Fig. 3.18).

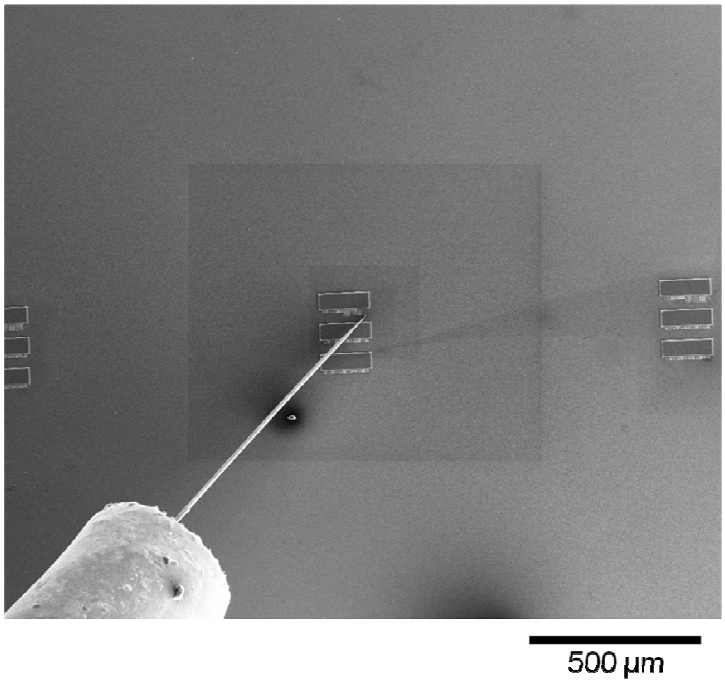

Figure 3.9: Low magnification SEM image of Micromanipulator tip positioned over the fabricated nanostructures.

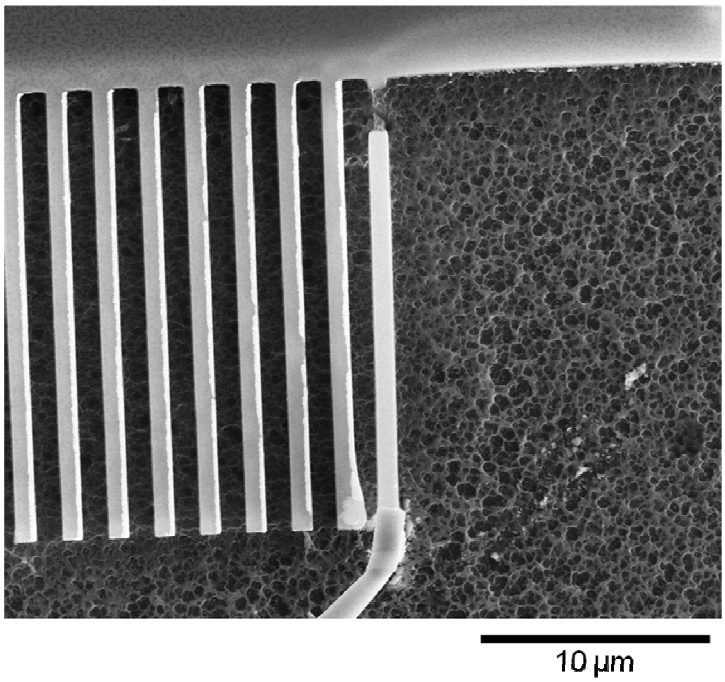

Figure 3.10: SEM image of the micromanipulator tip attached to the free end of a nanobeam while the other end is milled off using FIB.

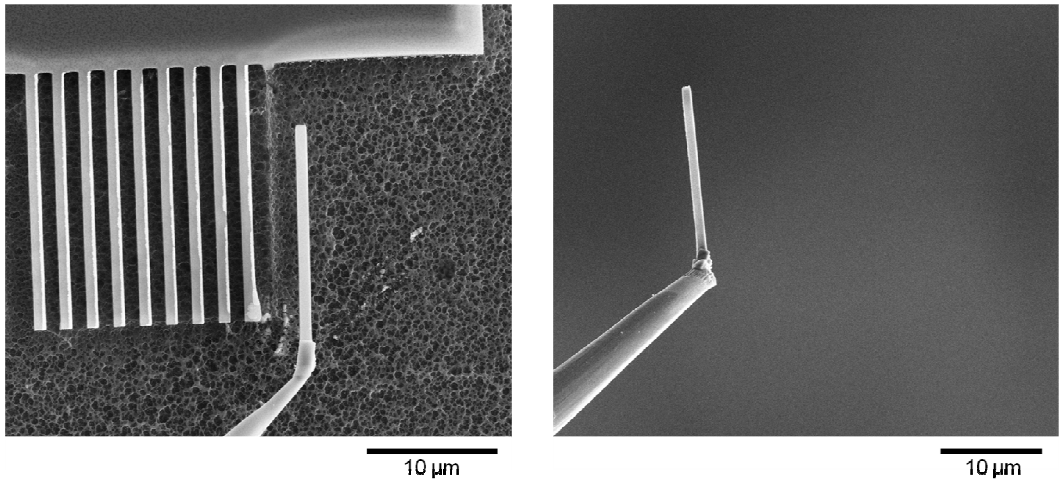

Figure 3.11: Nanobeam attached to the micromanipulator tip being removed from the substrate.

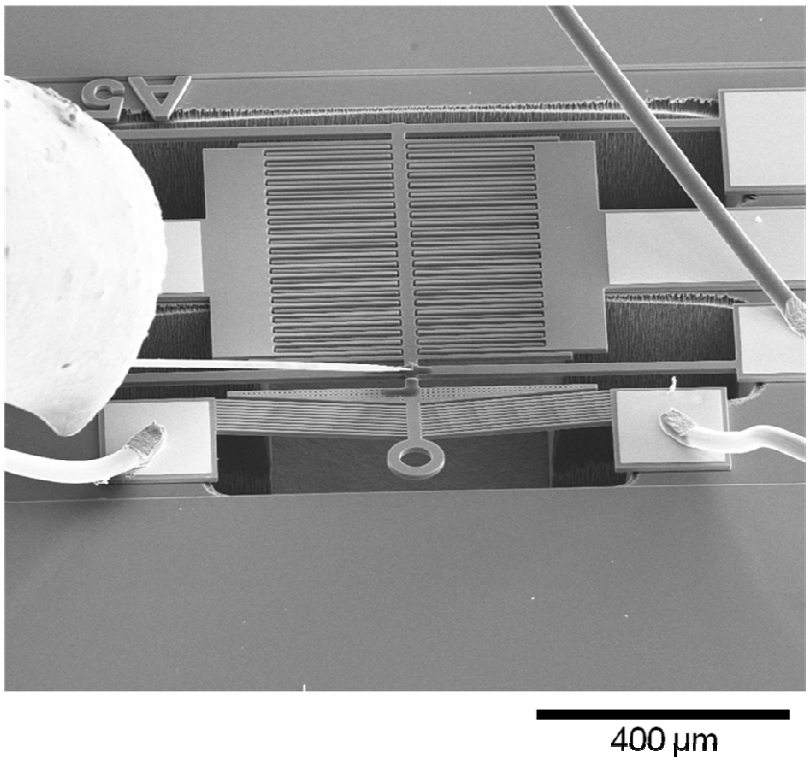

Figure 3.12: SEM image of the micromanipulator tip with the nanostructure positioned over the MEMS device.

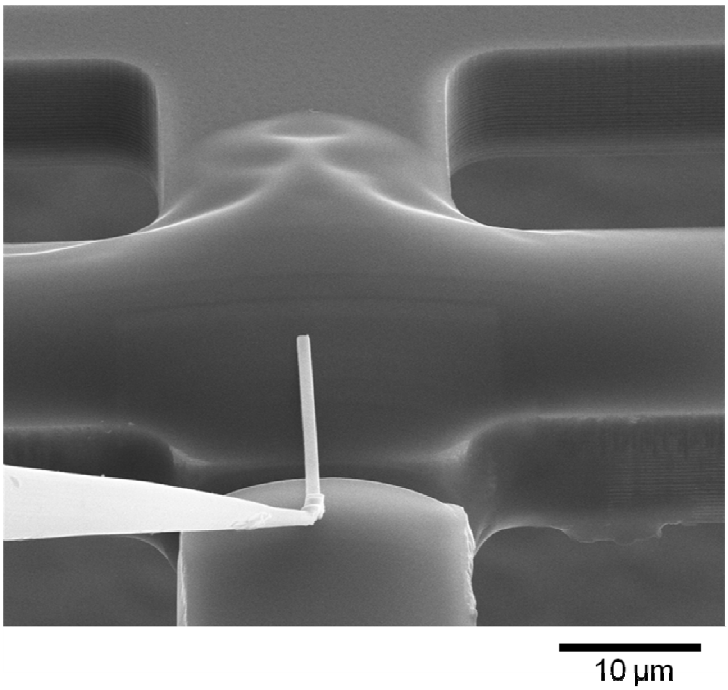

Figure 3.13: SEM image of the micromanipulator tip with the nanostructure positioned over the specimen gap.

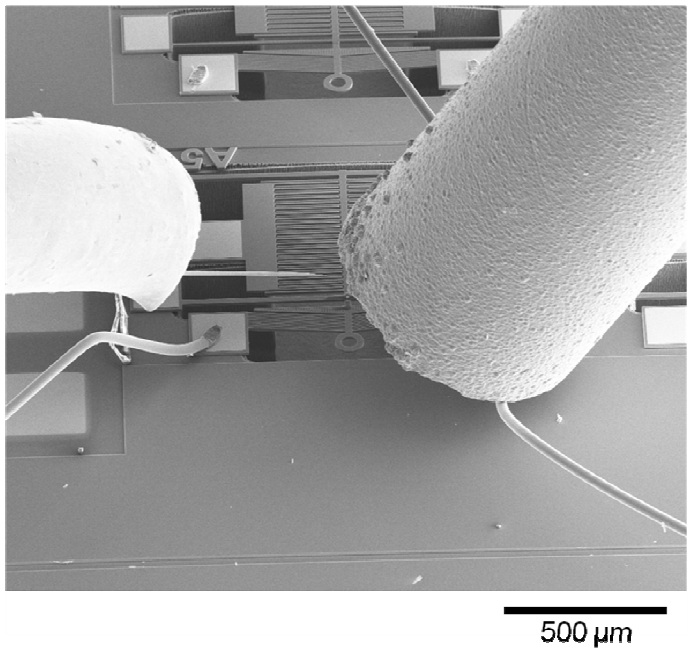

Figure 3.14: SEM image of the GIS needle inserted into the system for ion assisted Pt deposition.

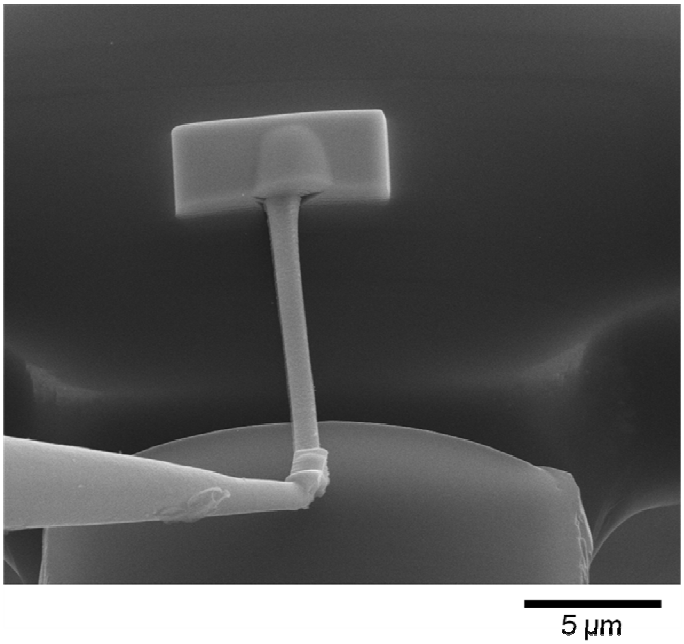

Figure 3.15: Pt deposition at one end of the nanostructure for clamping while the other end is still attached to the micromanipulator tip.

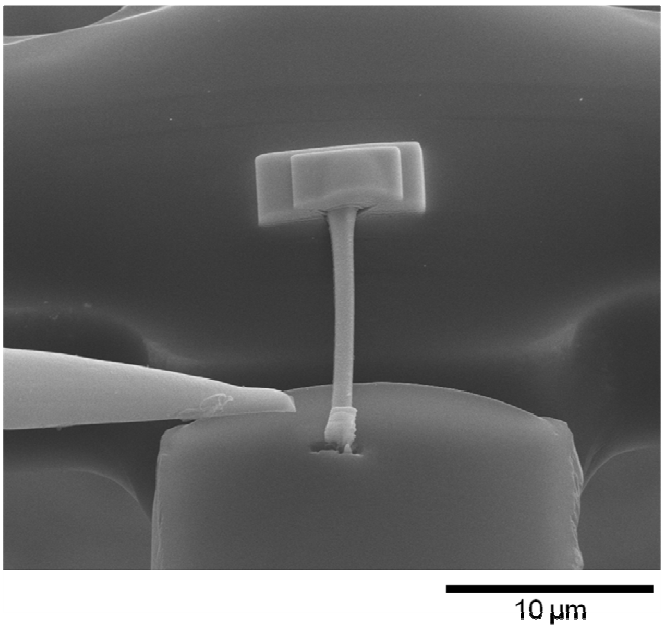

Figure 3.16: Separating the micromanipulator tip from the nanostructure using FIB milling.

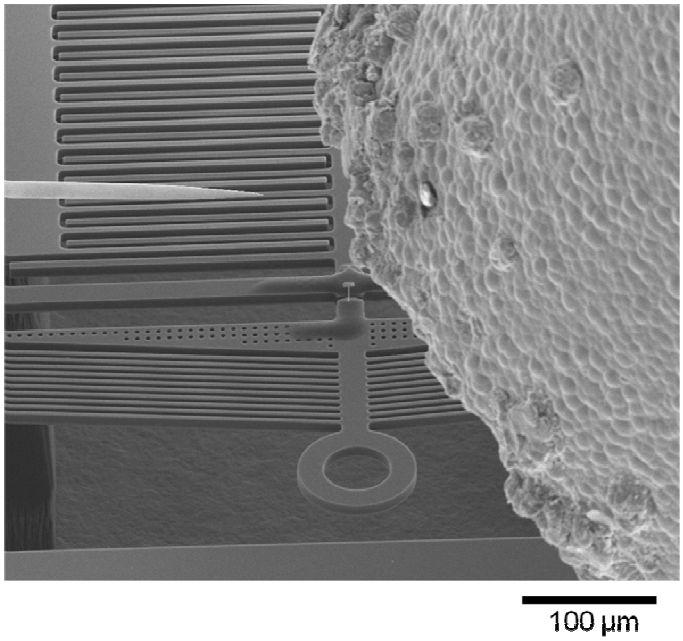

Figure 3.17: SEM image of the micromanipulator tip being removed after attaching the nanostructure over the MEMS device. The GIS system needle is visible in the right part of the image.

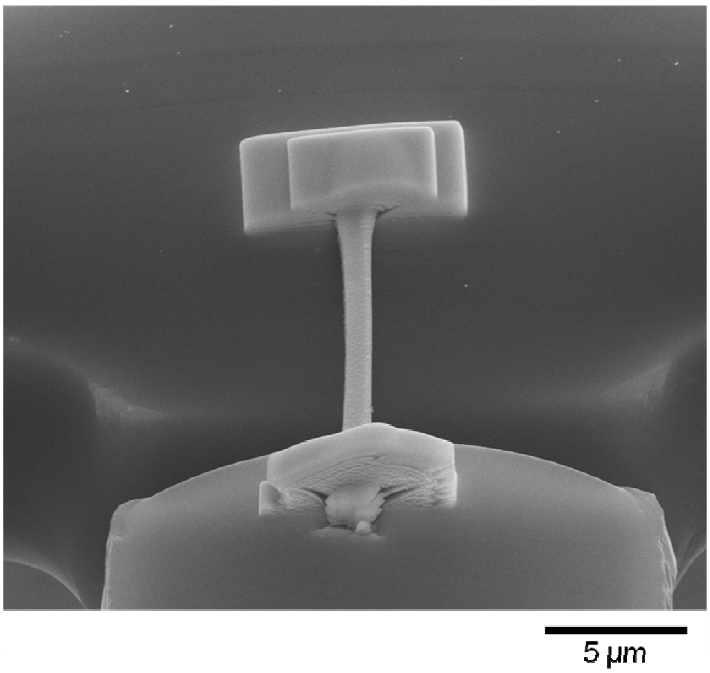

Figure 3.18: SEM image of the positioned nanostructure clamped across the specimen gap using ion assisted Pt deposition.

The Ni nanobeams were relatively easier to manipulate with a higher success rate as compared to highly brittle Si nanowires which were much more prone to failure during the manipulation process itself. Furthermore due to the horizontally aligned fabricated Ni nanobeams, the alignment issue was less significant. Small misalignments could be corrected during the manipulation process as compared to brittle Si nanowires which were much more prone to failure in bending mode.

3.3.3 Strength of Pt Clamps

It is important to ensure that the strength of the deposited Pt clamps is sufficient for tensile testing i.e. clamps should not fail before the nanostructure being tested. To investigate the strength of the Pt clamps, a Si nanowire was manipulated and clamped across the specimen gap of a MEMS device. The micromanipulator tip itself was used to

deflect the load sensor resulting in failure of the nanowire in tensile mode. It can be observed in Fig. 3.19 that the failure occurred in the nanowire and not the Pt clamps. Hence it can be deduced that the deposited Pt is sufficient for tensile testing of the nanostructures.

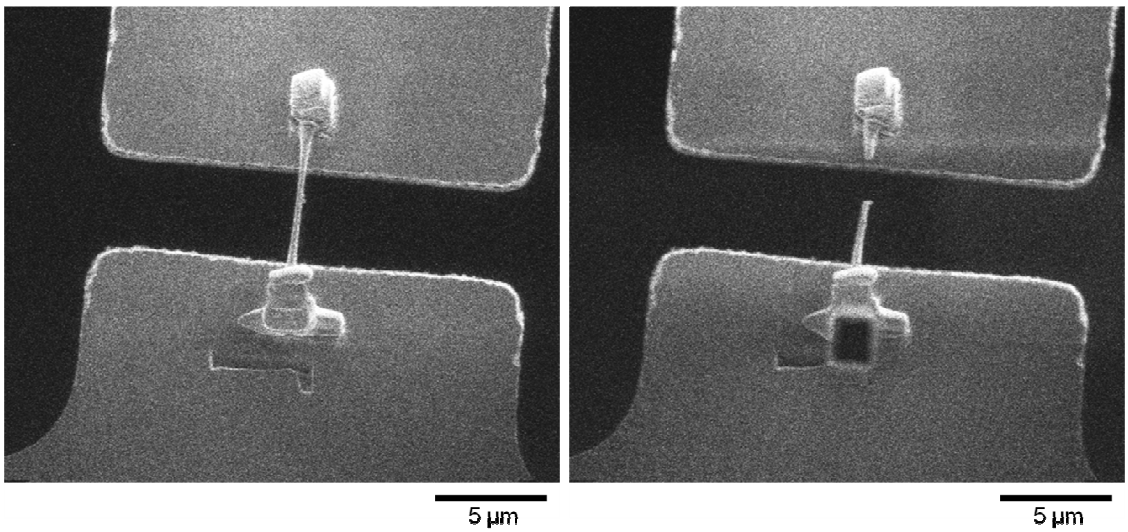

Figure 3.19: SEM images of: Left- Si nanowire before tensile loading, Right- Failed Si nanowire due to applied load sensor deflection.

3.4 Testing of Nanostructures

Two sensing schemes were used for testing namely capacitive and resistive (refer Chapter 2 for detailed discussions). The advantages and issues involved with both schemes are discussed next.

3.4.1 Capacitive Sensing

Capacitive sensing for the MEMS devices can be used to study the stress-strain behavior for nanostructures (refer Chapter 2 for details). For the current design, there were a few issues pertaining to testing of conductive nanostructures. Attempts were made to test the fabricated Ni nanostructures (refer Section 3.2) capacitive sensing. However due to electrical coupling between the actuation and sensing for conductive Ni nanostructures, a current flow (current densities > 10^{10}A/m^2 for Ni nanobeams) through the nanostructures (due to differential potential for actuation and sensing) resulted in burning (Fig. 3.20) of the nanostructures (Joule heating due to current flow).

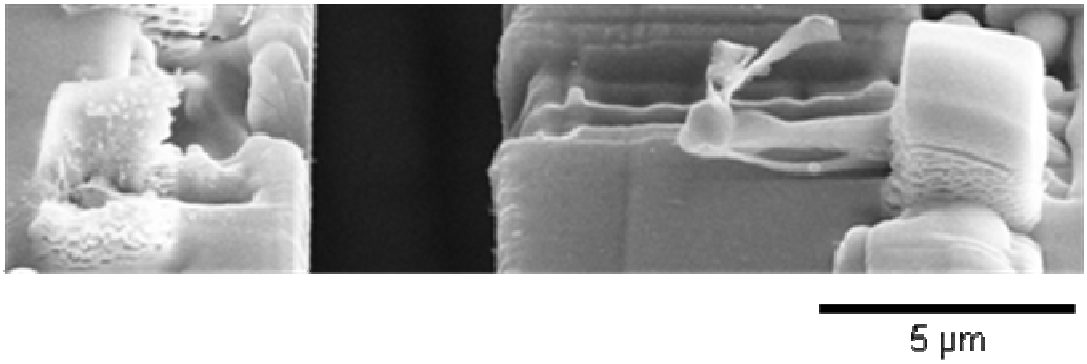

(a)

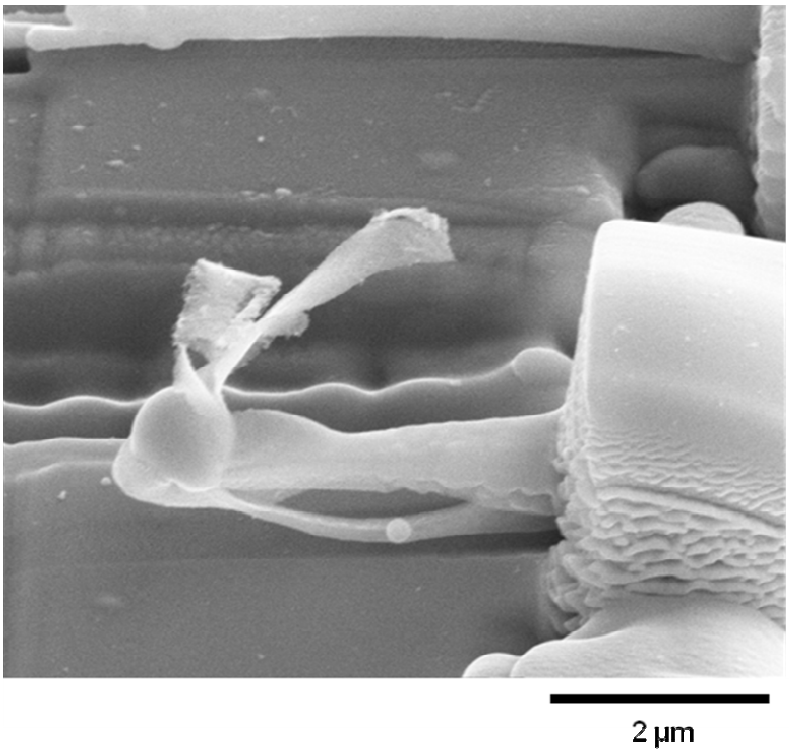

(b)

Figure 3.20: SEM image of a Ni nanostructure burnt due to electrical coupling between actuator and capacitive sensing.

Similar burning issues were observed for Si nanowires. Fig. 3.21 shows a globule formation due to melting of Si nanowire. A much more sever burning case has been shown in Figs. 3.22 and 3.23.

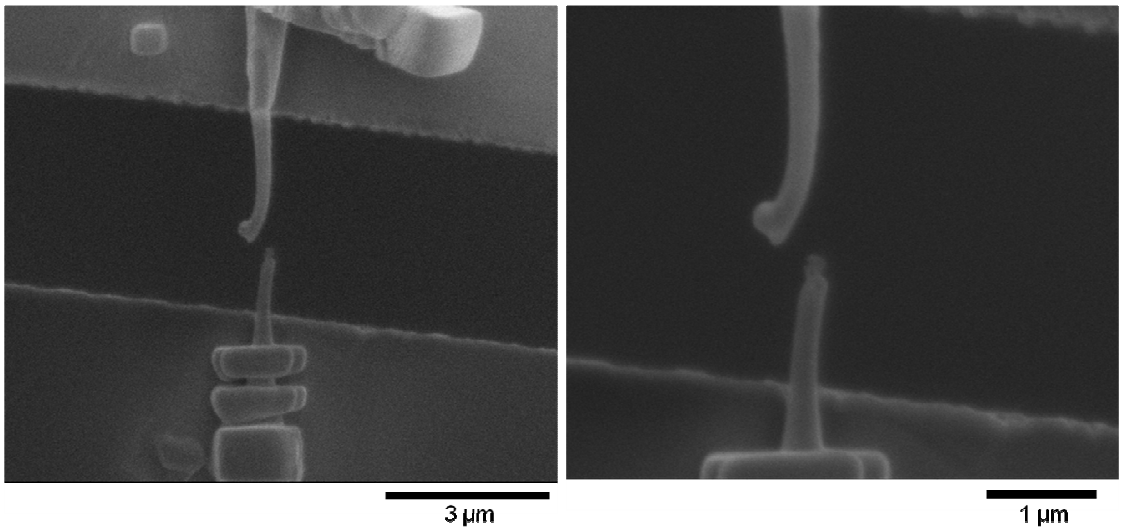

Figure 3.21: SEM image of a melted Si nanowire due to electrical coupling between actuator and capacitive sensing.

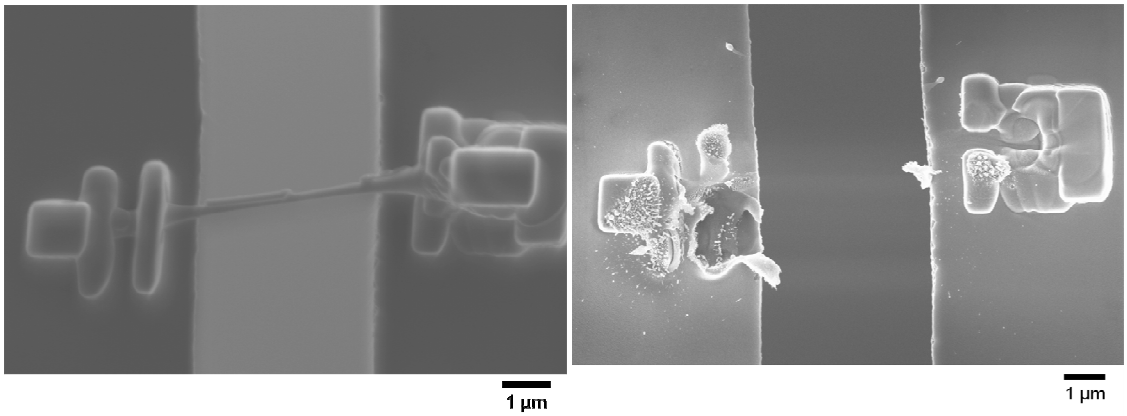

Figure 3.22: Severe melting case of Si nanowire due to electrical coupling between actuator and capacitive sensing. Left: Original nanowire, Right: Burnt after testing.

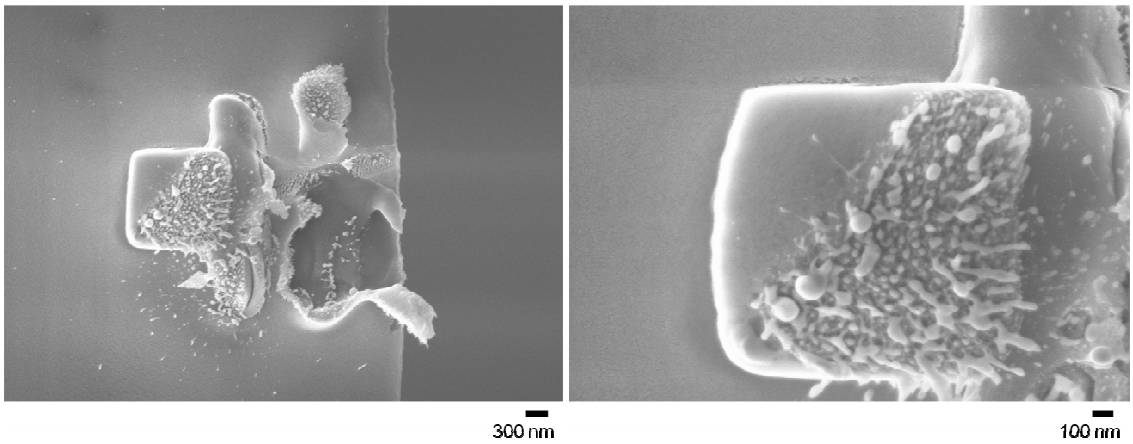

Figure 3.23: Higher magnification SEM images for burnt Si nanowire in Fig. 3.22. Droplets formed due to melted material can be clearly observed.

The devices were coated with 150 nm of insulating Al_2O_3 layer using ALD (Atomic Layer Deposition) in an attempt to electrically insulate the conductive nanowires from the actuator and sensing. However the thickness of the deposited layer was insufficient to prevent electrical breakdown resulting in burning of nanowires (Fig. 3.24)

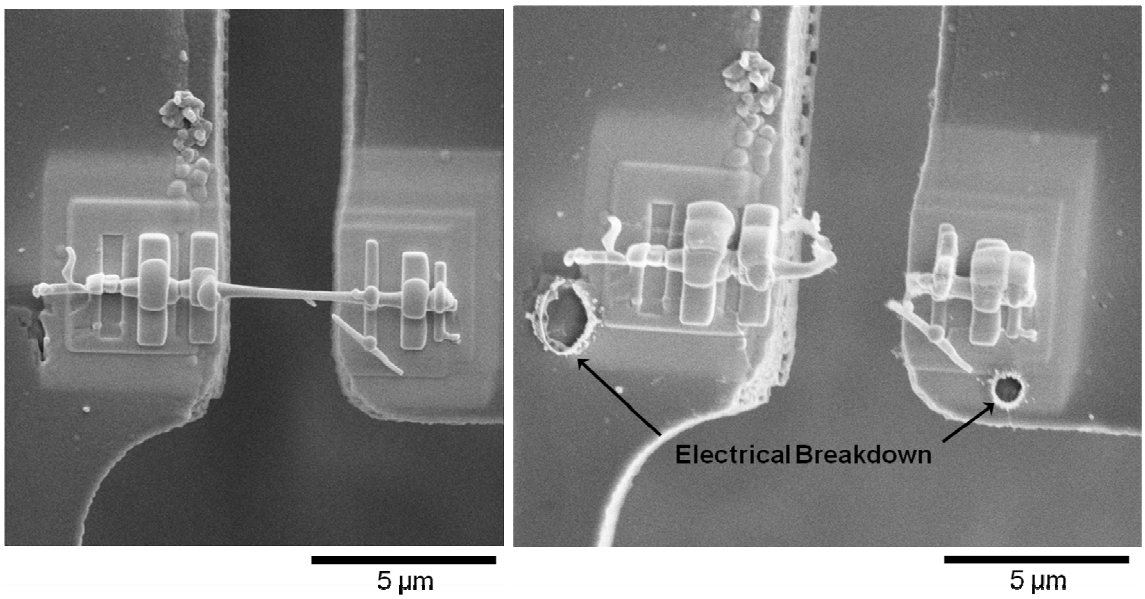

Figure 3.24: SEM image of burnt Si nanowire over ALD coated MEMS device. Left: Original nanowire, Right: Burnt after testing. Electrical breakdown of the Al_2O_3 layer is clearly visible in the right image.

This emphasized the need for a thicker insulating coating to prevent electrical breakdown of the insulating layer. However the long time required for thicker Al_2O_3 coating using ALD makes it impractical and consequently use of epoxy glue was attempted.

Insulating epoxy glue was applied across the specimen gap (Fig. 3.25). This glue was then cut completely using FIB (Focused Ion Beam) to separate the actuator and load sensor.

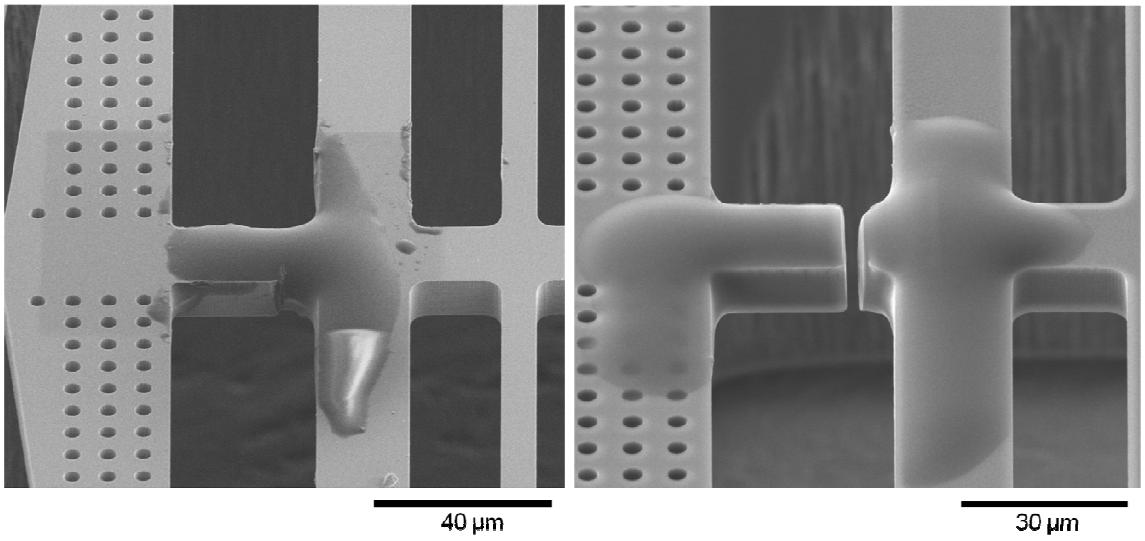

Figure 3.25: SEM images of: Left:- epoxy glue applied over the specimen gap, Right:- epoxy glue milled completely to separate the actuator and load sensor.

A Ni nanostructure was placed across the milled gap over the dry epoxy glue and tested with capacitive sensing. However the glue thickness obtained still did not prove to be thick enough and electrical breakdown of the glue layer resulting in nanowire melting was observed (Fig. 3.26). The cutting process using FIB itself reduces the glue thickness significantly especially near the gap edges. Consequently breakdown of the glue layer occurred closer to the gap edges as can be observed in Fig. 3.26.

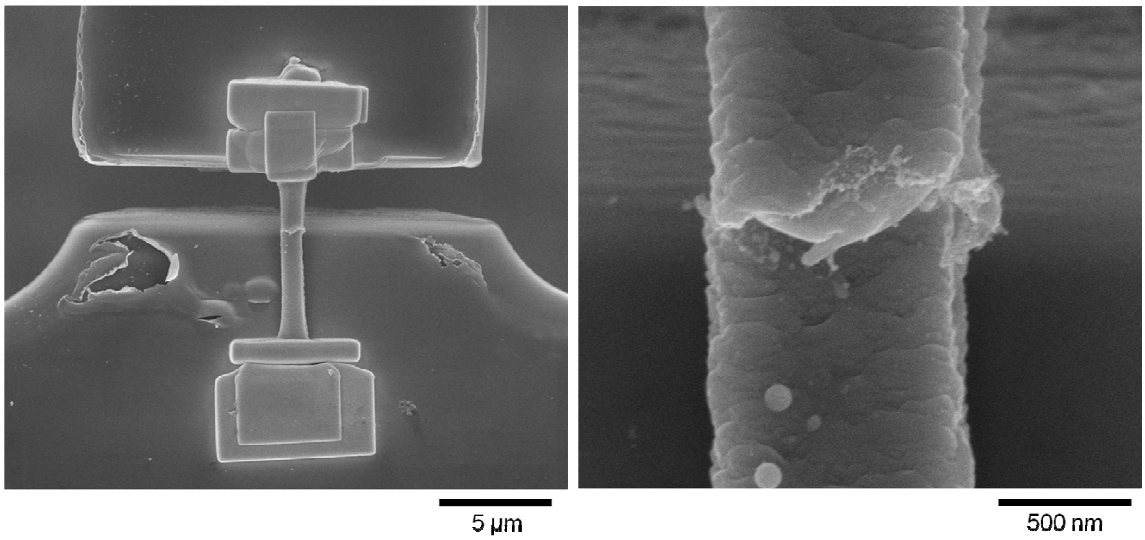

Figure 3.26: SEM images of: Left – Electrical breakdown of the glue layer, Right – Melting of Ni nanostructure due to the breakdown.

Hence even higher effective thickness of insulating glue layer would be required to prevent electrical breakdown and nanowire burning issues. This necessitates modifications in the MEMS device design for testing of conductive specimens and has been further discussed in Chapter 4.

3.4.2 Resistive Sensing

Resistive sensing can be used to detect specimen failure for nanotensile testing. SOIMUMPs27 design was used for two point resistance measurements. The resistance across the conductive nanostructure was measured (see Chapter 2 for details) using Agilent 34420A NanoVolt, Micro-Ohm Meter. Failure of specimen theoretically results in an infinite resistance. Ni nanobeams fabricated (see Section 3.2) were placed across the specimen gap of uncoated SOIMUMPs27 MEMS devices and tested using resistive sensing. However resistance sensing can only be used to detect specimen failure. It does

not provide any direct information regarding the force-displacement behavior of the tested specimen.

3.4.2.1 Specimen Degradation Effects Due to Resistive Sensing

To ensure that the resistive sensing itself does not cause degradation of nanostructures (Figs. 3.27-3.29), the sensing scheme was applied to a Ni nanostructure for 1 hour and SEM imaging was done to detect any signs of degradation (Fig. 3.29). The surface profile for the nanostructures did not show observable degradation due to the current flow during resistance sensing. Furthermore, the current densities used for resistive sensing were ~10^7 A/m^2 which are much below the critical current densities (~10^{12}A/m^2) quoted for various materials (refer Huang et. al. [62] and Durkan et. al. [63]).

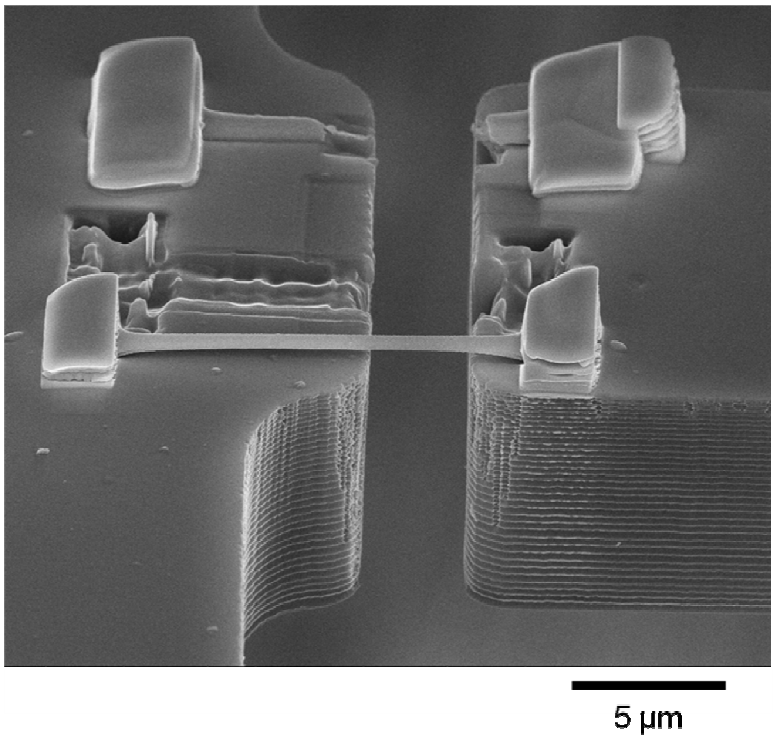

Figure 3.27: SEM image of Ni nanostructure before resistive sensing.

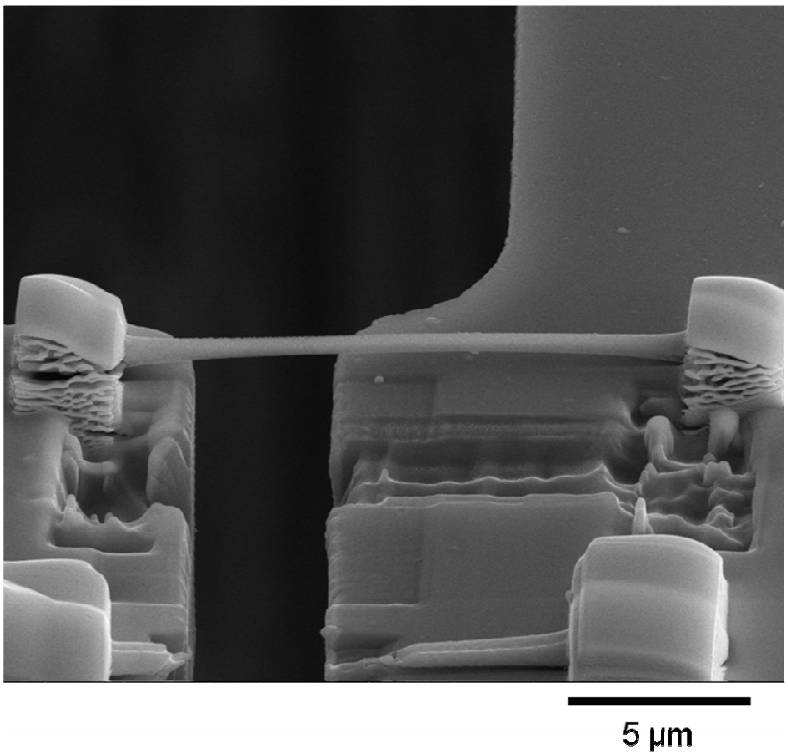

Figure 3.28: SEM image of Ni nanostructure after applying resistive sensing scheme for test duration.

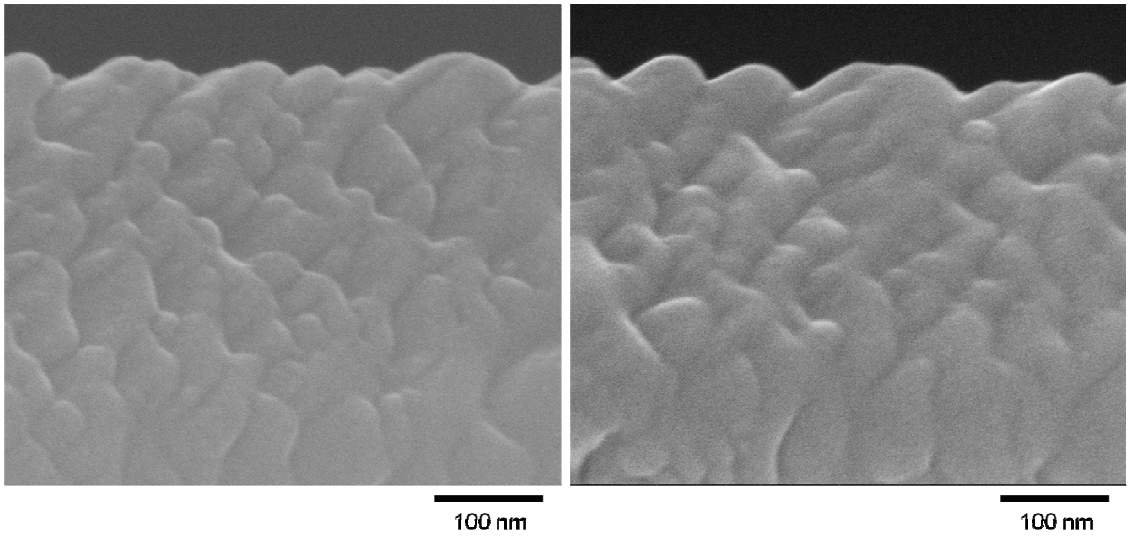

Figure 3.29: SEM image of the Ni nanostructure surface before (left) and after (right) 1 hour of resistive sensing. No actuator voltage was applied during the process.

3.4.2.2 Tensile Test

A Ni nanostructure with cross-sectional dimension 1000 nm x 500 nm and length 12.3 µm was placed on a SOIMUMPs27 MEMS device (Fig. 3.30) with 21 µm Load Sensor stiffness beams (stiffness 480 N/m).

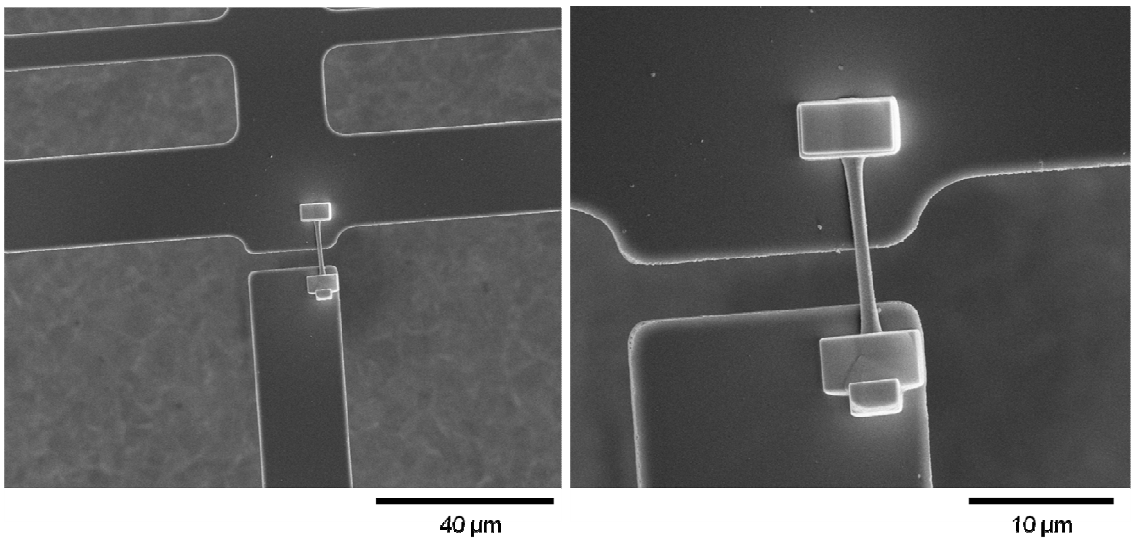

Figure 3.30: SEM images of a Ni nanostructure placed and clamped across the specimen gap of a SOIMUMPs27 MEMS device.

Two point resistance measurements (using Agilent 34420A NanoVolt, Micro-Ohm Meter) were done across the Ni nanostructure to detect the failure point. Agilent 3649a was used as the power source to give the required driving voltage to the actuator.

The actuator driving voltage was increased in increments and simultaneous resistance measurements were done. Very slow loading rates were applied: - a total actuator deflection of 1500 nm corresponding to 1.36 GPa specimen stress was applied in 20 minutes. No failure of the specimen was observed during the tensile loading. Unloading was done very rapidly. Actuator deflection was decreased from 1500 nm (1.36 GPa stress) to 0 nm in 5 seconds. Specimen failure occurred during the unloading process and was confirmed from SEM images.

A probable cause of specimen failure during unloading process can be attributed to the plastic deformations due to tensile loading. Upon rapid unloading of the actuator (1500 nm to 0 nm in 5 seconds), these plastic deformations can result in compressive stresses in the nanostructure which can in turn lead to specimen failure due to buckling. The buckling failure hypothesis of the nanostructure was strengthened by the SEM images of the failed specimen (see Fig. 3.31).

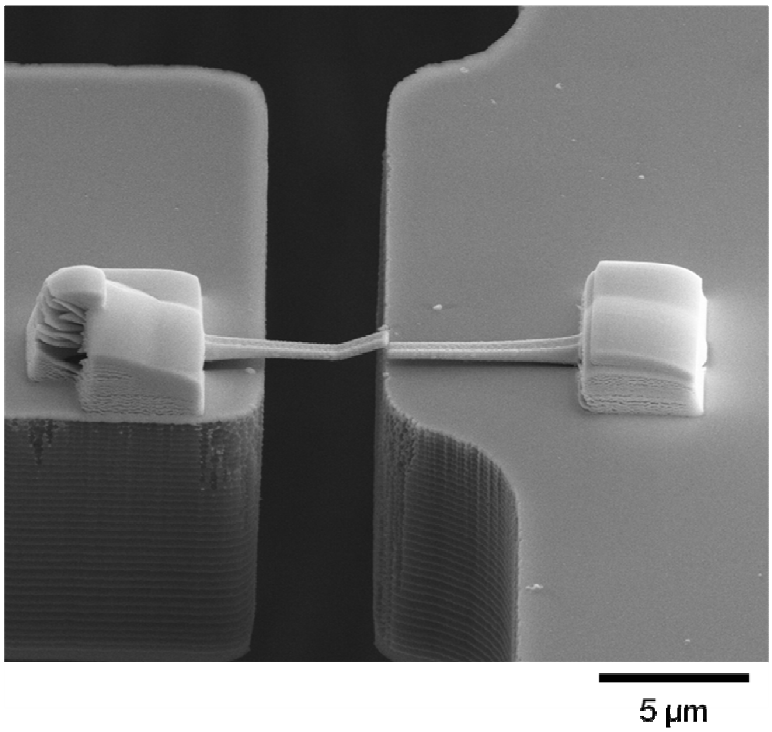

(a)

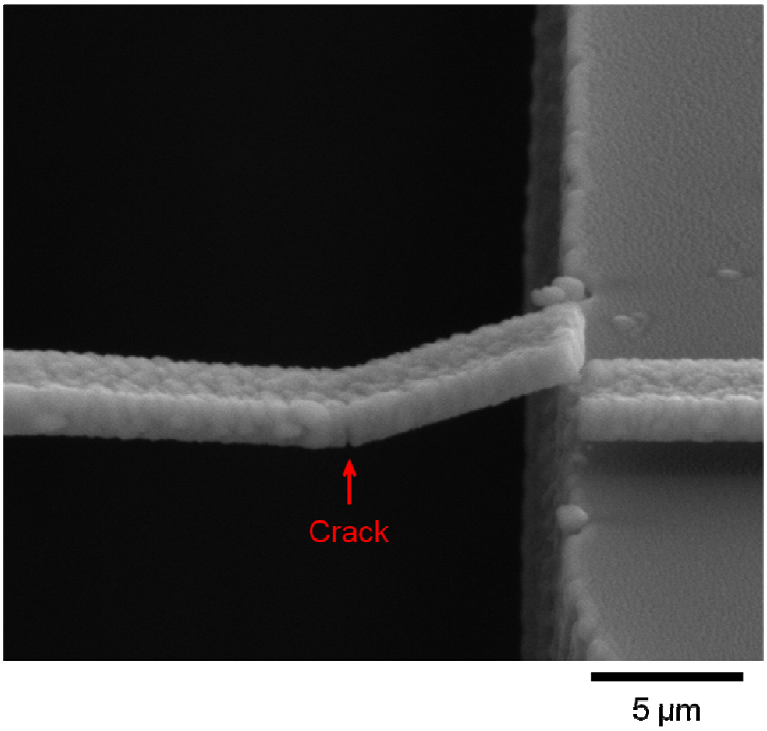

(b)

Figure 3.31: (a) SEM image of the failed Ni nanostructure (b) High magnification SEM image of the failure region. The presence of crack in the lower surface and the failure configuration hints towards buckling failure.

However further evidence for the presence of plastic deformation in the nanostructure required for such a buckling failure hypothesis was required and so the matter was further investigated.

A Ni nanobeam with dimensions 15.5 μm x 550 nm x 250 nm was placed on a SOIMUMPs27 MEMS device (load sensor stiffness 480 N/m). Different actuator deflections were applied followed by unloading and SEM imaging was done for the specimen after each unloading. Slow loading and unloading was done for the devices (1100 nm actuator deflection corresponding to 2.58±0.3 GPa specimen stress in 4 minutes). Slow unloading was done to prevent specimen failure during the unloading process. Fig. 3.32 shows the specimen profile after different loadings. However during the test, the specimen temperature changes with the applied actuator voltage and consequently actuator deflection. The corresponding stress values calculated using equations 2.1 and 2.2 and SEM images and corresponding specimen temperatures have been mentioned in Fig 3.22. No measurable plastic deformation was observed for a lower stress of ~ 550±200 MPa (Fig. 3.32 (b)). However significant plastic deformation can be observed for higher stress values (see Fig. 3.32 (c)) thus validating the hypothesis for buckling failure during the unloading process due to residual plastic deformations.

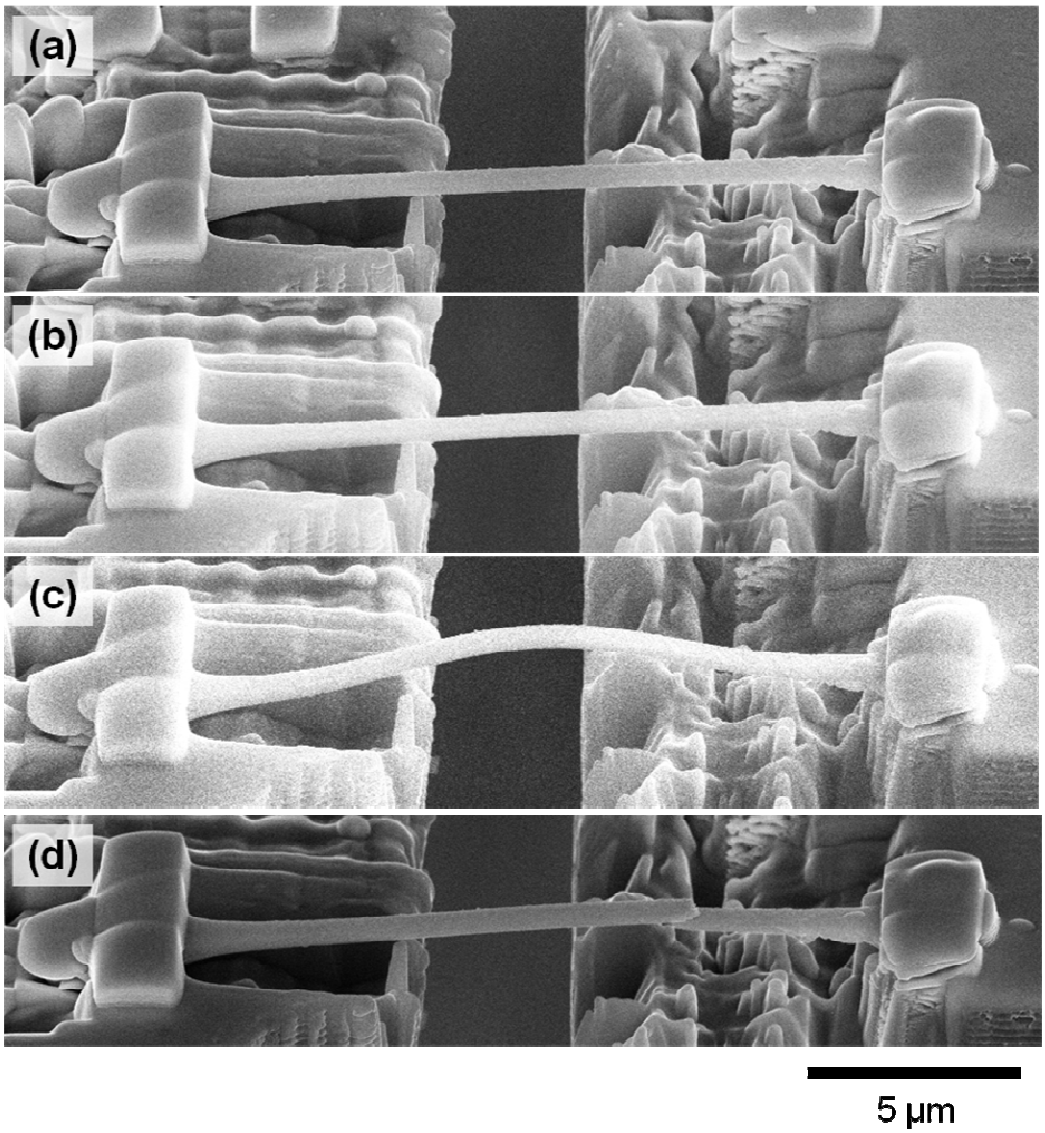

Figure 3.32: SEM images of the Ni nanostructure tested after different applied loadings. (a) Before testing (b) After 200 nm applied actuator deflection, 550±200 MPa stress and ~40°C specimen temperature (c) After 1100 nm applied actuator deflection, 2.58±0.3 GPa stress and 140°C specimen temperature (d) After failure. (Viewed at 52° from the top)

SEM images were used to calculate the plastic deformation of the nanostructure for the applied loading. Total 160 nm plastic deformation (1% plastic strain) was observed for 1100 nm applied actuator deflection or 2.58±0.3 GPa applied stress at 140°C for the specimen. The elastic modulus of 200 GPa for nanocrystalline Ni thin films was used [65] for the calculations (refer equations 3.1 and 3.2) for stress and elastic strain

(1.29% elastic strain for 2.58±0.3 GPa applied stress). The plastic deformation was also considered for stress calculations. The governing equations used to calculate the stress and elastic strain are as below (modification of equations 2.1 and 2.2):

$$X_A = X_{S\,(Plastic)} + X_{S\,(Elastic)} + X_{LS} \quad (3.1)$$

$$F = K_S X_{S\,(Elastic)} = K_{LS} X_{LS} \quad (3.2)$$

$$K_S = E * A / L \quad (3.3)$$

Where X_A is the actuator deflection, $X_{NW\,(Plastic)}$ is the plastic elongation of the specimen, $X_{NW\,(Elastic)}$ is the elastic elongation of the specimen, X_{LS} is the deflection of the load sensor, F is the force applied on the specimen and the load sensor, K_{LS} (480 N/m) is the load sensor stiffness and K_S is the specimen stiffness, E=200GPa is the Elastic modulus for the specimen [65], A is the specimen area of cross-section and L is the specimen length between the clamps. Plastic elongation $X_{S\,(Plastic)}$ is obtained from the SEM images. Stress can be calculated as F / A.

Earlier studies have reported a tensile strength of 2 GPa for nanocrystalline (nc) macroscopic Ni specimens [66]. The nanocrystalline Ni nanostructures tested (as discussed above) did not fail in tensile mode 2.58 GPa stress. However plastic deformation was observed for 2.58±0.3 GPa stress at 140°C specimen temperature. Thermal expansion of the specimen due to the increase in specimen temperature are small and can be safely neglected for the stress calculations (~30-40 nm thermal elongation of the tested specimens for 140°C rise in specimen temperature compared to 1100nm actuator deflection). Further increase in loading resulted in the failure of the Ni nanobeam (Figs. 3.33 and 3.34). Plastic deformation at failure calculated using SEM images was found to be ~ 300 nm (1.9%).

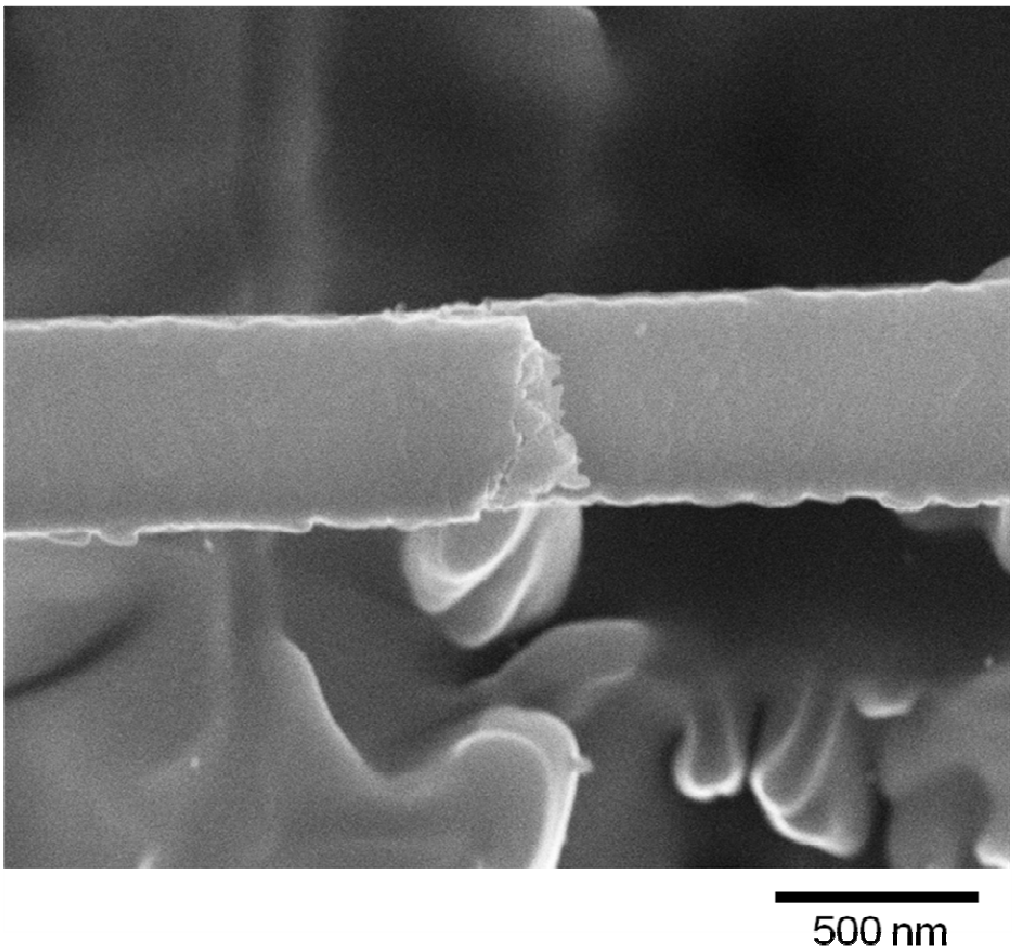

Figure 3.33: SEM image (top view) of the broken Ni nanowire.

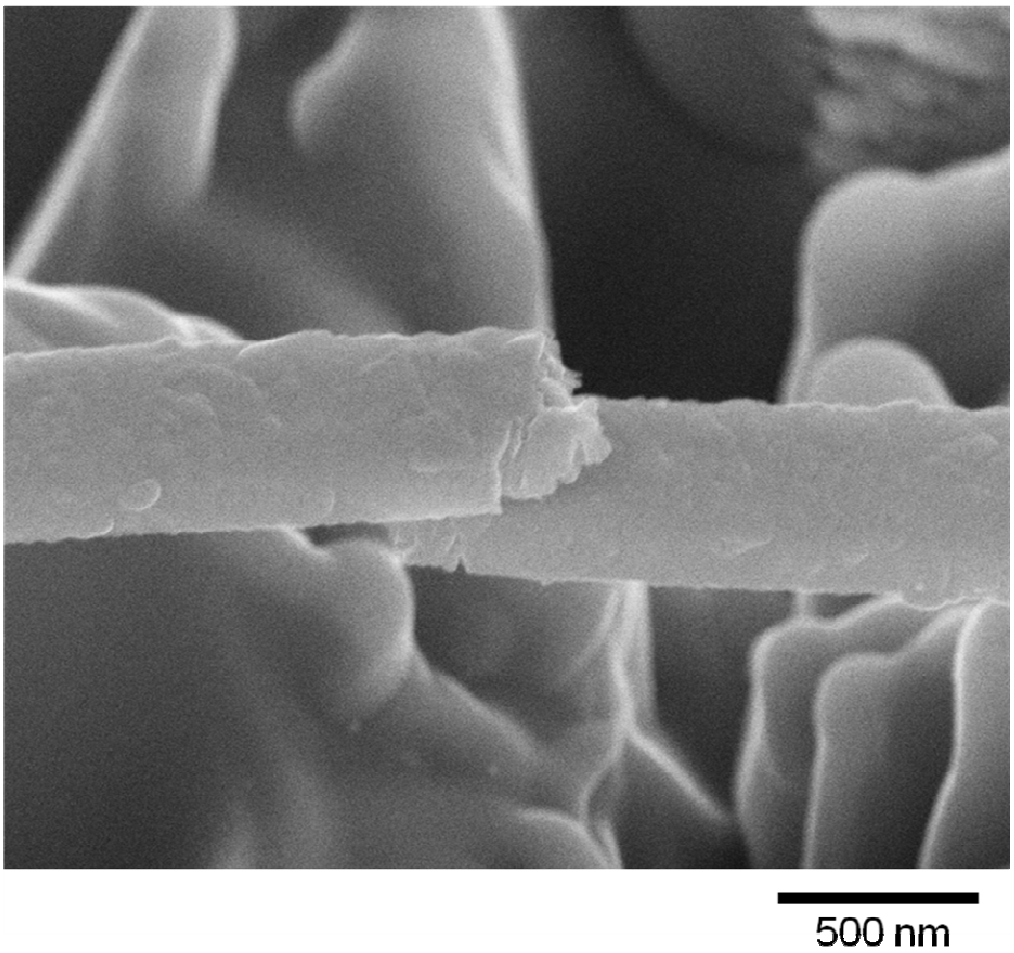

Figure 3.34: SEM image (viewed at 52° from the top) of the broken Ni nanowire.

Further tests to investigate the failure stress and plastic deformation behavior are however required for more conclusive understanding of this behavior. The observed plastic elongation in Ni nanobeams may also be due to creep in the specimen [67]. Higher loading rate tests can be used to further study this behavior.

CHAPTER 4

MEMS REDESIGN FOR NANOSCALE TESTING AT CONTROLLED TEMPERATURES USING CAPACITIVE SENSING

As discussed in Chapter 2, capacitive sensing is required to study the stress-strain behavior of nanostructures. However with the current design, electrical coupling between the actuator and sensing resulted in a current flow through the conductive nanostructures resulting in specimen burning. This prevented the use of capacitive sensing during testing of conductive nanostructures/nanowires. Attempts for the use of Al_2O_3 coating using ALD (Atomic Layer Deposition) as well as epoxy glue to electrically isolate the nanostructure from the actuator and sensing components were unsuccessful due to the insufficient thickness of the layer. Consequently the MEMS devices were redesigned to address this issue.

4.1 Improved Design

A new design for the MEMS nanotensile tester was developed for capacitive sensing (see Fig. 4.1). Several changes were made in the current design, not just to cater to the various complications but also to significantly improve the performance of such testing systems. The basic actuator design from SOIMUMPs24 and SOIMUMPs27 was slightly modified. Additional horizontal breams were provided to reduce the temperature away from the actuator due to conduction through silicon.

Even though the basic design of the load sensor was kept the same as compared to SOIMUMPs24 and SOIMUMPs27, two load sensor units were provided (see Fig. 4.1)

instead of one. This design modification provides the ability to make capacitive measurements in differential mode consequently directly providing the specimen strain.

Another modification in the new design is the presence of three 4 μm gaps instead of only one in the previous design. These gaps are essential for electrical isolation of the specimen from the sensing as well as isolation of the actuator driving voltage from the sensing component. Epoxy glue placed in the first two gaps (see Fig. 4.1) would result in mechanical connectivity of the actuator to the load sensor and the specimen while maintaining electrical isolation. The specimen to be tested must be placed across the third gap.

Detailed discussions on the various improvements and aspects of design are discussed next.

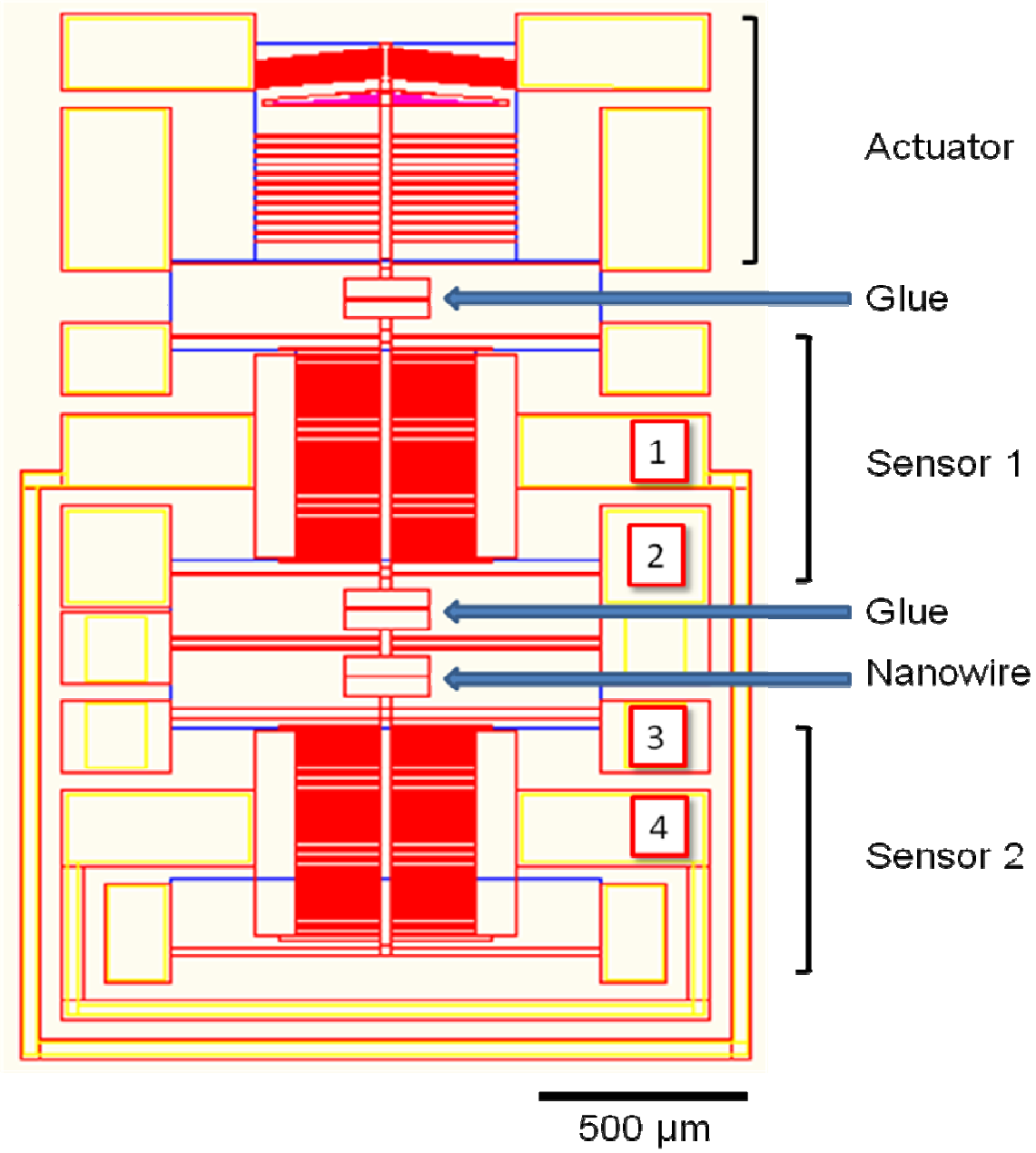

Figure 4.1: Schematic layout of the improved design for MEMS nanotensile tester. Pads 1 and 4 are connected to CS1 and CS2 of MS3110 (refer Chapter 2) and pads 2 and 3 are connected to CSCOM.

4.2 Electrical Isolation

It was observed that no electrical breakdown of glue occurred for glued MEMS devices (refer Chapter 2 for capacitance sensing with glued devices). Consequently it can be deduced that 4 µm thickness of epoxy glue (equal to specimen gap) would be sufficient to prevent electrical breakdown and hence provide electrical isolation of the specimen from the actuator and sensing.

Further tests were conducted to ensure the insulation properties of epoxy glue. The glue thickness proved to be sufficient to prevent effect of DC bias voltage from the actuator on the sensing component (refer Section 2.7.2.2.3).

Furthermore, it is important to ensure that the glue thickness is enough to prevent AC currents flowing through the specimen due to sensing. The sensing circuit uses 2.25 V square waves with frequencies 100 KHz for capacitance change measurements. This was simulated by applying an AC signal with amplitude 2.25 V and frequency 100 KHz (using Agilent 33220A waveform generator) across the specimen gap for a glued SOIMUMPs27 MEMS device. The resulting current was measured using SR570 Low-Noise Current Amplifier. No measureable current flowing through the specimen gap for a glued device was observed. Hence it can be deduced that 4 µm glue thickness is enough to provide sufficient electrical isolation against AC signals from sensing.

4.3 Temperature Near Specimen

A significant problem in the previous design is the increased temperature near the specimen due to the thermal actuator (refer Section 2.5). The new design would be able to cater to this problem. Since the tested specimen is located farther away from the actuator, it would experience insignificant rise in temperatures with increasing driving

voltage. Extra horizontal heat sink beams as well as sensor 1 would contribute to significant heat dissipation resulting in lower temperatures near the specimen. A qualitative estimate of the ability of load sensor can be found from the Infra-Red measurement discussed in Chapter 2. It can be observed from the temperature profiles in Fig. 2.18 that the temperature gradient due to heat dissipation by the load sensor results in near substrate temperatures towards the farther end of the load sensor. Consequently sensor 1 (Fig. 4.1) along with the horizontal actuator heat sink beams should be sufficient to reduce the temperature obtained near the specimen.

4.4 Differential Capacitive Sensing

The new design includes two sensor units (sensor 1 and 2 – see Fig. 4.1) on both sides of the specimen to be tested as compared to only one load sensor in SOIMUMPs24 and SOIMUMPs27 designs. This enables the capacitance change measurements in differential mode for the two sensor units. All difference in capacitance changes for sensor 1 and 2 can be directly measured using MS3110 and can be directly used to calculate the elongation of the specimen. For a particular applied actuator driving voltage, all the actuator deflection (X_A) would be reflected as the deflection in sensor 1 (X_{S1}) (assuming glue stiffness is much higher than stiffness of sensors 1 and 2). Now this deflection X_{S1} is reflected as specimen elongation (X_{NW}) and deflection in sensor 2 (X_{S2}) (Fig. 4.2).

$$X_{S1} = X_{NW} + X_{S2} \tag{4.1}$$

$$\Rightarrow \quad X_{NW} = X_{S1} - X_{S2} \tag{4.2}$$

Since the capacitance change shows a linear variation with deflection of load sensor for small deflections (refer Chapter 2, Fig. 2.6) a factor Z can be used to reflect the transformation from deflection to capacitance change.

$$X_{S1} = Z * \Delta C_1 \tag{4.3}$$

Where ΔC_1 is the capacitance change for sensor 1 deflection X_{S1}. This Z can be found from device calibration (using Fig. 2.39). Since the designs of comb structures for sensor 1 and 2 are the same, the same transformation factor Z can be used for sensor 2.

$$X_{S2} = Z * \Delta C_2 \tag{4.4}$$

From equations 4.2, 4.2 and 4.3 we get

$$\Rightarrow \quad X_{NW} = Z * (\Delta C_1 - \Delta C_2) \tag{4.5}$$

In the differential mode for MS3110, $(\Delta C_1 - \Delta C_2)$ i.e. the difference in capacitance change for sensors 1 and 2 can be directly measured. This can be used to calculate directly the elongation in the specimen.

The force applied on the specimen can be calculated by

$$F = K_{S2} * (X_A - X_{NW}) \tag{4.6}$$

Where K_{S2} is the stiffness of Sensor 2.

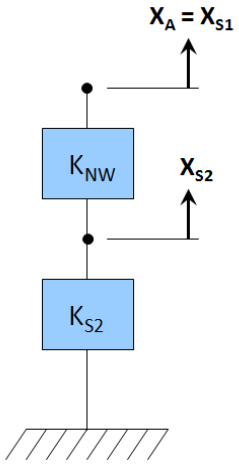

Figure 4.2: Illustration of the Lumped mechanical model for the new design.

However in the earlier design the specimen elongation was calculated using (refer Chapter 2)

$$X_{NW} = X_A - X_{LS} \tag{4.7}$$

Where X_A and X_{LS} are actuator and Load Sensor deflections respectively. Even though measurements of X_{LS} or load sensor deflection for only one sensor case are precise (capacitive measurements), the relatively large errors in X_A from optical calibration can result in significant errors in calculated strain values. This error is significant due to nominal values of specimen elongation being measured (1% strain for a 10 micron long nanowire would represent 100nm specimen elongation). For example a 10% error in optical calibration of actuator (100nm error for 1µm actuator deflection) can result in extremely large errors (up to 100% error) in the calculated strain values. However for the new design, the errors in specimen elongation measurements would be guided by the precision of capacitive measurements which have much higher precision (~5nm for previous design – refer Appendix B) as compared to optical measurements (~100nm error).

4.5 Advantages and Disadvantages of Improved Design

The new design promises several advantages over SOIMUMPs24 and SOIMUMPs27 designs. The primary advantage is to provide electrical isolation for the specimen from the actuator and sensing thus preventing specimen degradation and burning for capacitive sensing. Hence conductive nanostructures can be tested using capacitive sensing for investigating their stress-strain behavior.

Another significant advantage is the ability to perform differential capacitive measurements due to the presence of two capacitive sensors. This enables direct measurements of specimen elongation significantly reducing the measurement errors as compared to the previous designs (refer Section 4.4).

The new design also mitigates the problem of high temperatures near the specimen due to the thermal actuator. The previous designs faced the problem of

temperature dependence near the specimen on the actuator driving voltage and consequently the applied force. The new design shows great promise in that respect.

Another advantage of the improved design is the ability to simultaneously investigate the electrical and mechanical behavior of nanostructures for example to study the piezoressitive effect for nanostructures.

The only disadvantage of the new design is the increased size of the MEMS nanotensile testers due to the presence of two sensors. However the device is still small enough to go inside a TEM chamber. Furthermore the base across the specimen gap for nanowire placement has been significantly increased in size (see Fig. 4.1) so as to allow reuse of the MEMS device for multiple testing.

CHAPTER 5

CONCLUSIONS

This study focused on the development of a MEMS thermal nanotensile tester to investigate the mechanical behavior of one-dimensional nanostructures. Extensive characterization for two different designs of the developed devices was performed by both experimental methods as well as finite element modeling. The actuator deflections for various applied driving voltages were characterized using optical calibration. Diffraction is known to limit the accuracy of optical measurements to a spatial resolution comparable to the wavelength of light being used. However, the method developed was able to measure the actuator deflection with accuracy below the diffraction limit. The thermal behavior of the devices was extensively studied using Infra-Red (IR) microscopy as well as Micro-Raman to obtain the temperatures near the specimen as well as in the actuator. The stiffness of the load sensor was determined using resonance method. Results obtained from Finite Element Analysis were found to be in good correlation with the experimental characterization performed.

Tensile testing of nanostructures requires manipulation of individual nanostructures on the MEMS device. This proves to be extremely challenging specially for brittle Si nanowires. The various complications involved with the process have been investigated. An efficient procedure for such manipulation involving fabricated Ni nanobeams was developed. Two different sensing schemes for nanoscale testing namely, capacitive and resistive, have been discussed. Capacitive sensing can be used to study the stress-strain behavior of nano-specimens while resistive sensing can only be used to detect specimen failure. Several issues regarding burning and degradation of nanostructures for capacitive sensing due to electrical coupling between the actuator and

sensing, hampered the testing of conductive specimens. Observations regarding plastic deformations for nanocrystalling (NC) Ni nanobeams were made using resistive sensing.

An improved design for the MEMS nanotensile tester was developed for capacitive sensing to investigate the stress-strain behavior of nanostructures. Several changes were made in the current design, not just to cater to the various complications but also to significantly improve the performance of such testing systems. The improved design is expected to achieve electrical isolation of the specimen from the actuator and sensing. The incorporation of two sensors in differential mode would enable direct strain measurements with increased precision. Furthermore it shows much promise in mitigating the temperature variability of the specimen during the testing process.

APPENDIX A

MICRO RAMAN MEASUREMENTS

Micro-Raman measurements (Table A.1) were made to determine the temperatures achieved for varying driving voltages at different locations of the device including regions near the nanowire (see Fig. A.1).

Table A.1: Temperatures at different locations (refer Fig. A.1 for location nomenclature) and varying driving voltages/currents for a SOIMUMPs24 MEMS device obtained with Micro-Raman measurements.

Location	Driving Voltage(V)	Temp [ºC]
Beam Middle	0	19.8
	1	30.9
	2	72.1
	3	149.8
Stem before HS	0	19.8
	1	36.2
	2	84.8
	3	173.6
Near Nanowire Middle L	0	19.8
	1	31.2
	2	78.0
	3	166.4
Near Nanowire Middle M	0	19.8
	1	31.4
	2	75.7
	3	166.6
Near Nanowire Middle H	0	19.8
	1	29.0
	2	77.5
	3	162.6

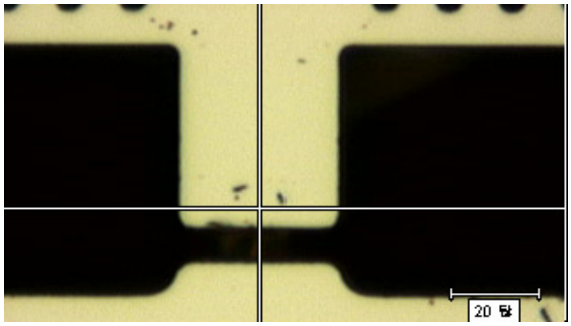

Near Nano Wire Middle L

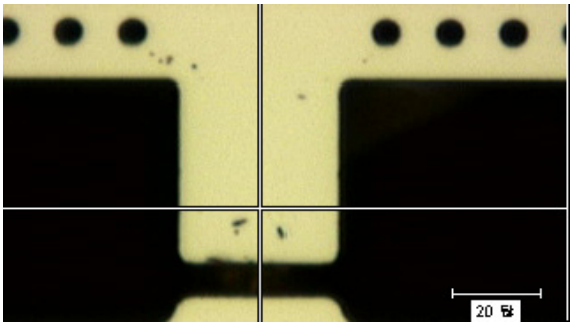

Near Nano Wire Middle M

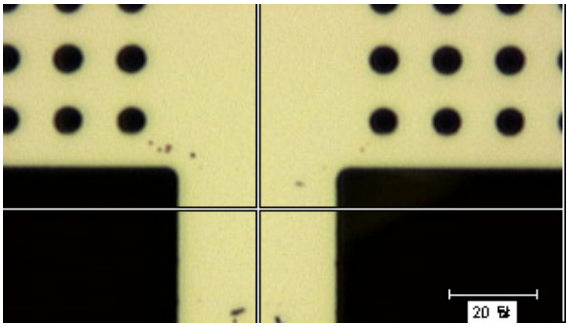

Near Nano Wire Middle H

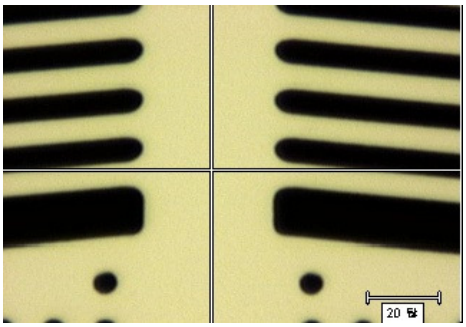

Stem before heat sink

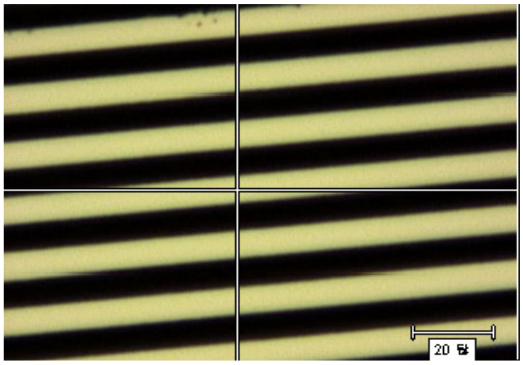

Beam middle

Figure A.1: The different locations where temperatures were measured and their nomenclature.

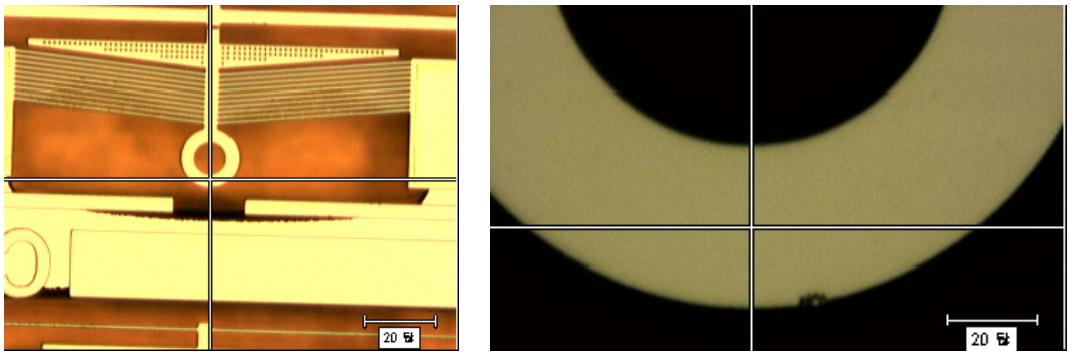

10 X objective 50 X objective

Figure A.2: Location of the point used for initial calibration for Micro-Raman measurements. This point was chosen for minimum stress effect in the peak position based calibration (refer Beechem et. al. [53]).

APPENDIX B

RELIABILITY, REPEATABILITY AND PRECISION FOR CAPACITIVE SENSING

B.1 Repeatability and Precision of Measurements and Device Reliability

Labview was used to control the driving voltage as well as to capture the output signal from the circuit (MS3110). Driving voltage was varied from 0 to 3 V in equal incremental steps. In each step the driving voltage was increased, then some time (2 sec) was provided for the device to reach in equilibrium and then acquisition was started. Acquisition was done at a rate of 1000 data points per second for varying time intervals. These data points were averaged for each acquisition cycle for noise reduction and standard deviation was calculated for the acquired signal. All the tests were performed in air. The experimental setup was as described in Section 2.7.2.

The expression for the output voltage is given by:

$$V_0 = GAIN * V2P25 * 1.14 * (CS2_T - CS1_T)/C_F + VREF \quad (B.1)$$

Where V_0 is the output voltage

GAIN = 2 or 4 V/V nominal

V2P25=2.25V

$CS1_T$=CS1IN+CS1

$CS2_T$=CS2IN+CS2

VREF=2.25V

C_F is the Feedback capacitor

The capacitance change for the load sensor can then be calculated from this change in the output voltage (V_0). Non-conductive epoxy glue was used to glue the actuator and sensor of the device (Fig.2.9). The effect of loading rate and acquisition time on the capacitance change was investigated and good repeatability was observed (Figs. B.1, B.2).

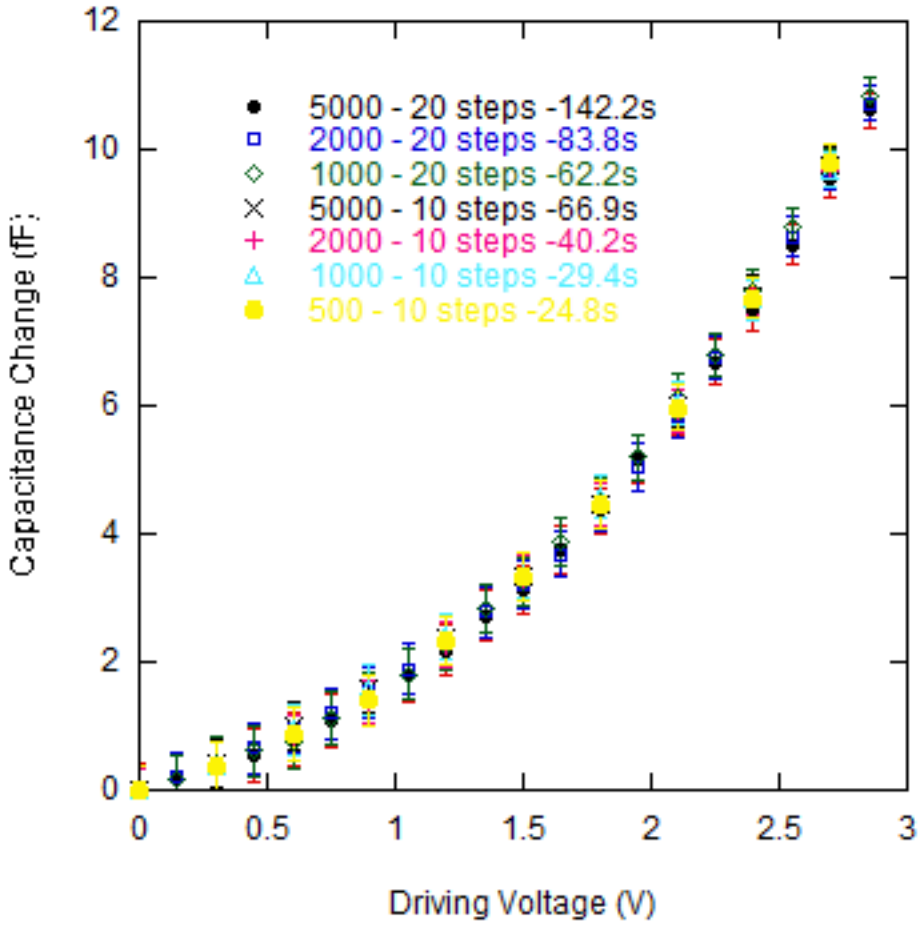

Figure B.1: Influence of loading rates on capacitance change Vs driving voltage (glued SOIMUMPs24 device). Legend :- 5000 - 20 steps -142.2s : 5000 acquisition data points at 1Khz rate, 0-3V in 20 incremental steps, total test time 142.2 sec.

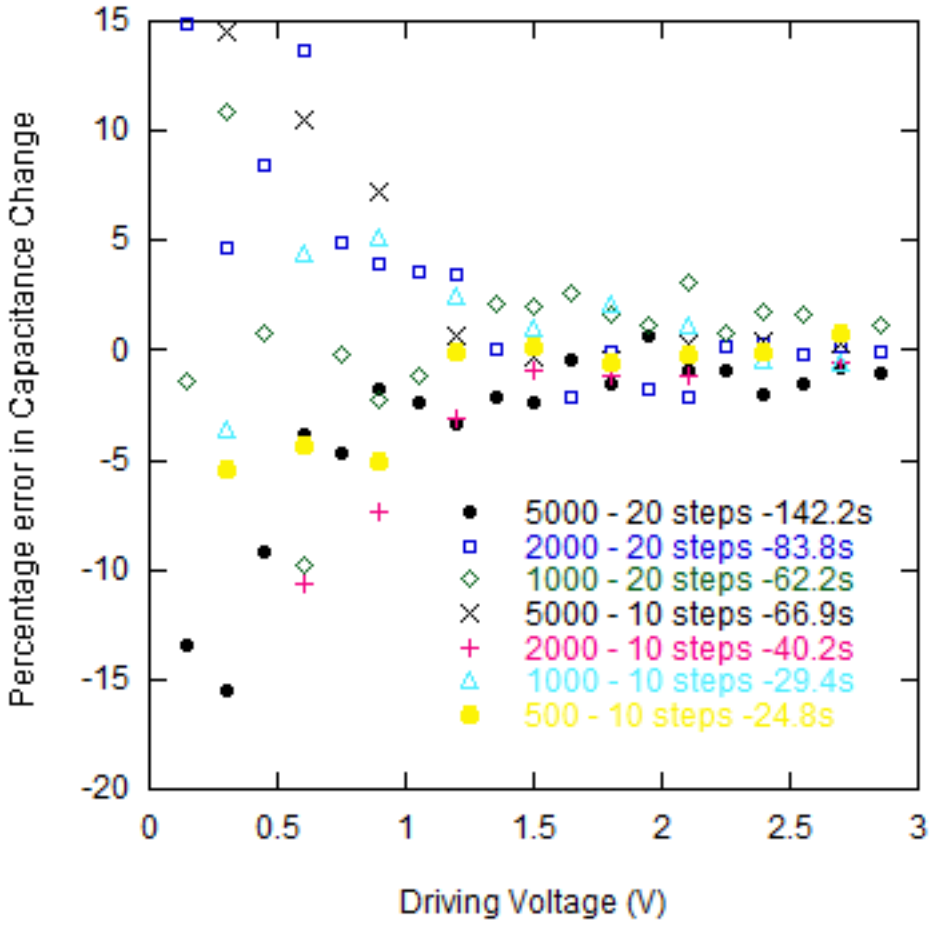

Figure B.2: Percentage error in the capacitance change measurements of a device for different loading rates as compared to the mean values from all the data. The percentage error is higher for small driving voltages due to very small displacements, and is very low for higher displacements (higher driving voltages). Legend :- 5000 - 20 steps -142.2s : 5000 acquisition data points at 1Khz rate, 0-3V in 20 incremental steps, total time 142.2 sec.

High precision small deflection measurements were made for a SOIMUMPs24 glued device (Fig. B.3). Capacitance change variation between multiple tests for the same device was investigated. Results show very high precision with the developed methodologies. Variation of ~0.05fF leading to ~5nm precision in deflection measurements was observed.

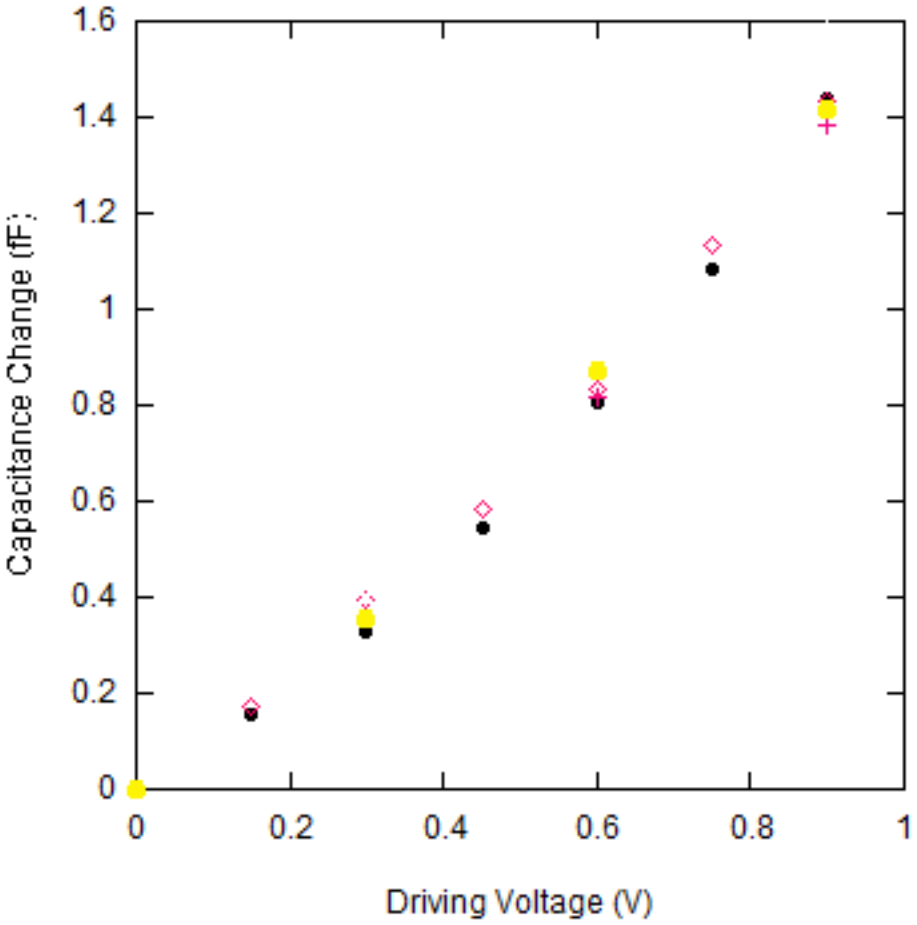

Figure B.3: Precision measurements for the same SOIMUMPs24 glued device.

Tests were done to investigate the variation in behavior between different devices (Fig. B.4). Different devices showed good reproducibility of results.

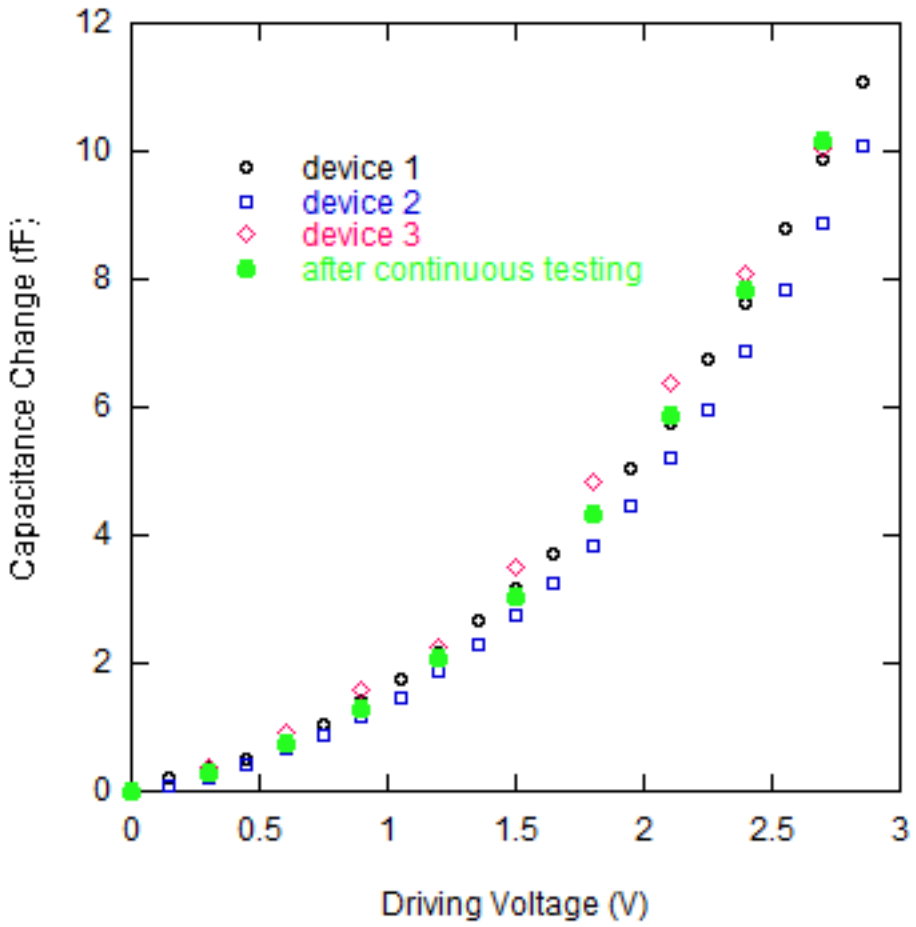

Figure B.4: Capacitance change measurements for different SOIMUMPs24 glued devices. "after continuous testing" represents a device that loaded continuously for ~1 day (at 3V driving voltage) and was tested again after that.

Also of importance is the possible thermal degradation of the devices for reusability. Optically no visible thermal degradation was observed on the actuator surface after multiple device use and application of 3V driving voltage (maximum driving voltage used) for one day.

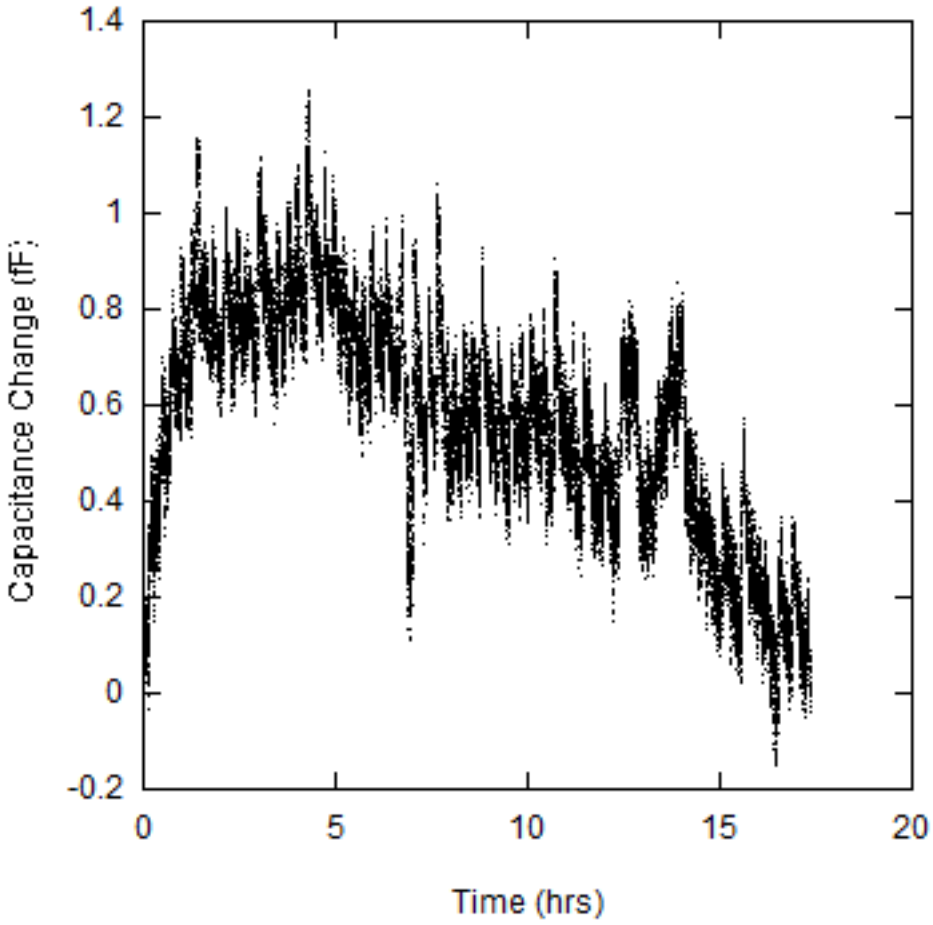

Figure B.5: Capacitance change over continuous testing with time (w.r.t. the capacitance at time =0). A constant driving voltage of 3 V was applied to the actuator and capacitance change was measured over time. No significant capacitance change is observed over time indicating no significant deterioration of the actuator or mechanical properties of the device with repeated usage.

The device was retested after the continuous one day 3V driving voltage application and the device showed no significant change in behavior (Fig. B.4). Furthermore, during continuous application of 3V driving voltage for one day, capacitance change was recorded during the testing which again showed no significant change (Fig. B.5). Hence it can be safely conjectured that the mechanical and electrical properties of the device did not change significantly even after device reuse due to thermal or other possible degradations.

B.2 Accuracy of Measured Capacitance

The capacitance change is measured from the change in output voltage using equation B.1. The capacitance change with driving voltage was measured for the same device using different values of feedback capacitor (C_F) from the circuit. Significant variation was observed in the calculated capacitance values for output voltage (V_0) using different C_F values (see Fig. B.6). Hence the C_F values may not be accurate as stated on the circuit and so the calculated value is not the exact value of the capacitance change but rather incorporates a multiplicative factor.

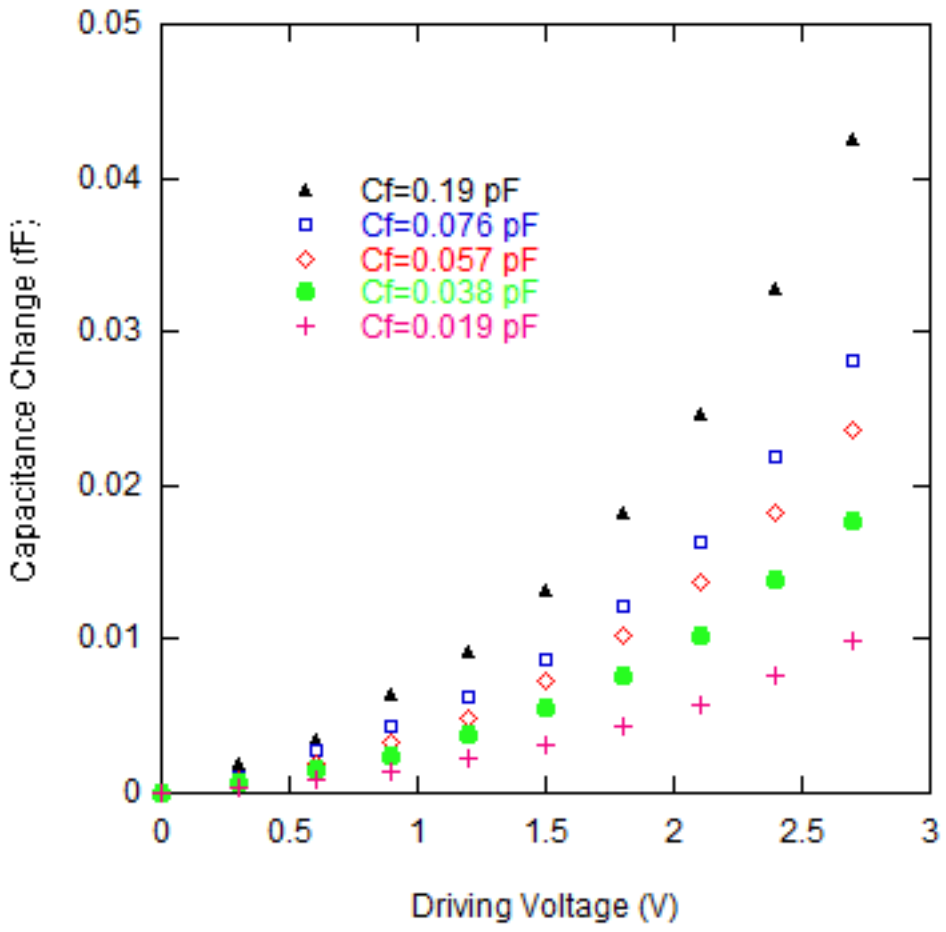

Figure B.6: Capacitance change measurements for the same glued device with varying feedback capacitance C_F.

Due to the extremely small value for the feedback capacitor (C_F), there could be significant errors in the absolute value of C_F and consequently the absolute values of the capacitance change measured. This resulted in a constant scaling factor (~2.5) for the measured capacitance change as compared to the actual values. To address this issue, the same feedback capacitor C_F was used throughout the study.

REFERENCES

[1] MILE, E., JOURDAN, G., BARGATIN, I., LABARTHE, S., MARCOUX, C., ANDREUCCI, P., HENTZ, S., KHARRAT, C., COLINET, E., and DURAFFOURG, L., "In-plane nanoelectromechanical resonators based on silicon nanowire piezoresistive detection", Nanotechnology, vol. 21, pp. 165504-1, 2006.

[2] HE, R., and YANG, P., "Giant piezoresistance effect in silicon nanowires", Nature Nanotechnology Letters, vol. 1, pp. 42-46, 2006.

[3] HAUGERUD, B., BOSWORTH, L. A., and BELFORD, R. E., "Mechanically induced strain enhancement of metal-oxide-semiconductor field-effect transistors", J. Applied Physics, vol. 94, pp. 4102-4107, 2003.

[4] LEE, M. L., FITZGERALD, E. A., BULSARA, M. T., CURRIE, M. T., and LOCHTEFELD, A., "Strained Si, SiGe and Ge channels for high mobility metal-oxide-semiconductor field effect transistors", J. Applied Physics, vol. 97, pp. 011101-1, 2005.

[5] HIEROLD, C., JUNGEN, A., STAMPFER, C., and HELBLING, T., "Nano electromechanical sensors based on carbon nanotubes", Sensors and Actuators A, vol. 136, pp. 51-61, 2007.

[6] JUNGEN, A., DURRER, L., STAMPFER, C., ROMAN, C., and HIEROLD, C., "Progress in carbon nanotube based nanoelectromechanical systems synthesis," Phys. Stat. Sol. (b) 244, vol. 11, pp. 4323-4326, 2007.

[7] JUNGEN, A., STAMPFER, C., HOETZEL, J., BRIGHT, V. M., and HIEROLD, C., "Process integration of carbon nanotubes into microelectromechanical systems," Sensors and Actuators A, vol. 130-131, pp. 588-594, 2006.

[8] WELDON, J. A., ALEMAN, B.,SUSSMAN, A., GANNET, W., and ZETTL, A. K., "Sustained Mechanical Self-Oscillations in Carbon Nanotubes," Nano Letters, vol. 10, no. 5, pp. 1728-1733, 2010.

[9] HORNG, Y. Y., LU, Y. C., HSU, Y. K., CHEN, C. C., CHEN, L. C., and CHEN, K. H., "Flexible supercapacitor based on polyaniline nanowires/carbon cloth with both

high gravimetric and area-normalized capacitance", Journal of Power Sources, vol. 195, pp. 4418-4422, 2010.

[10] JING, G. Y., DUAN, H. L., SUN, X. M., ZHANG, J. X., LI, Y. D., WANG, J.X., and YU, D. P., "Surface effects on elastic properties of silver nanowires: Contact atomic-force microscopy," Physical Review B, vol. 73, pp. 235409-1, 2006.

[11] CUENOT, S., FRETIGNY, C., DEMOUSTIER-CHAMPAGNE, S., and NYSTEN, B., "Surface tension effect on the mechanical properties of nanomaterials measured by atomic force microscopy," Physical Review B, vol. 69, pp. 165410-1, 2004.

[12] WU, B., HEILDELBERG, A., and BOLAND, J. J., "Mechanical properties of ultrahigh-strength gold nanowires," Letters Nature Materials, vol. 4, pp. 525-529, 2005.

[13] WU, B., HEILDELBERG, A., and BOLAND, J. J., "Microstructure-Hardened Silver Nanowires," NanoLetters, vol. 6, no. 3, pp. 468-472.

[14] NI, H., LI, X., and HAO, H., "Elastic modulus of amorphous SiO_2 nanowires," Applied Physics Letters, vol. 88, pp. 043108-1, 2006.

[15] GALL, K., DIAO, J., and DUNN, M. L., "The Strength of Gold Nanowires," Nano Letters, vol. 4, no. 12, pp. 2431-2436, 2004.

[16] LEACH, A. M., MCDOWELL, M., and GALL, K., "Deformation of Top-Down and Bottom-Up Silver Nanowires," Advanced Functional Materials, vol. 17, pp. 43-53, 2007.

[17] UCHIC, M. D., DIMIDUK, D. M., FLORANDO, J. N., and NIX, W. D., "Sample Dimensions Influence Strength and Crystal Plasticity," Science, vol. 305, pp. 986-989, 2004.

[18] GREER, J. R., OLIVER, W. C., and NIX, W. D., "Size dependence of mechanical properties of gold at the micron scale in the absence of strain gradients," Acta Materialia, vol. 53, pp. 1821-1830, 2005.

[19] KIM, J. Y., and GREER, J. R., "Tensile and compressive behavior of gold and molybdenum single crystals at the nano-scale," Acta Materialia, vol. 57, pp. 5245-5253, 2009.

[20] RICHTER, G., HILLERICH, K., GIANOLA, D. S., MONIG, R., KRAFT, O., and VOLKERT, C. A., "Ultrahigh Strength Single Crystalline Nanowhiskers Grown by Physical Vapor Deposition," Nano Letters, vol. 9, no. 8, pp. 3048-3052, 2009.

[21] LU, Y., GANESHAN, J., and LOU, J., "A multi-step method for in situ mechanical characterization of 1-D nanostructures using a novel micromechanical device," Experimental Mechanics, vol. 50, pp. 47-54, 2010.

[22] QUINN, G. D., FULLER, E., DAN, X., JILLAVENKATESA, A., LI, M., SMITH, D., and BEALL, J., "A novel method for measuring mechanical properties at the small scale: the theta specimen," Ceramic Engineering and Science proceedings, vol. 26, no. 2, pp. 117-126, 2005.

[23] HAQUE, M. A., and SAIF, M. T. A., "In-situ Tensile Testing of Nano-scale Specimens in SEM and TEM," Experimental Mechanics, vol. 42, no. 1, pp. 123-128, 2002.

[24] ZHANG, B., and FANG, D., "Modeling and modification of the parallel plate variable MEMS capacitors considering deformation issue," Mechanism and Machine Theory, vol. 44, pp. 647-655, 2009.

[25] NATHANSON, H. C., NEWELL, W. E., WICKSTROM, R. A., and DAVIS, J. R., "The resonant gate transistor," IEEE Transactions on Electron Devices, vol. 14, pp. 117-133, 1967.

[26] SEEGER, J. I., and BOSER, B. E., "Negative capacitance for control of gap-closing electrostatic actuators," in Proceedings of the 12th International Conference on Solid-State Sensors, Actuators and Microsystems (Transducers 03), Boston, MA, pp. 484–487.

[27] YOUNIS, M. I., "Investigation of the mechanical behavior of microbeam-based MEMS devices," MSc Thesis, Virginia Polytechnic Institute and State University, Blacksburg, VA., 2001.

[28] YOUNIS, M. I., and NAYFEH, A. H., "A study of the nonlinear response of a resonant microbeam to an electric actuation," Nonlinear Dynamics, vol. 31, pp. 91-117, 2003.

[29] RHOADS, J. F., SHAW, S. W., and TURNER, K. L., "The nonlinear response of resonant microbeam systems with purely-parametric electrostatic actuation," Journal of Micromechanics and Microengineering, vol. 16, pp. 890-899, 2006.

[30] KWUIMY, C. A. K., and WOAFO, P., "Modeling and dynamics of a self-sustained electrostatic microelectromechanical system," Journal of Computational and Nonlinear Dynamics, vol. 5, pp. 021010-1, 2010.

[31] NARAGHI, M., and CHASIOTIS, I., "Optimization of Comb-Driven Devices for Mechanical Testing of Polymeric Nanofibers Subjected to Large Deformations," Journal of Microelectromechanical Systems, vol. 18, no. 5, pp. 1032-1046, 2009.

[32] KIUCHI, M., MATSUI, S., and ISONO, Y., "Mechanical characteristics of FIB deposited carbon nanowires using an electrostatic actuated Nano tensile testing device," Journal of Microelectromechanical Systems, vol. 16, no. 2, pp. 191-201, 2007.

[33] CHEN, Y. C., CHANG, I. C. M., CHEN, R., and HOU, M. T. K., "On the side instability of comb-fingers in MEMS electrostatic devices," Sensors and Actuators A, vol. 148, pp. 201-210, 2008.

[34] RIETHMULLER, W., and BENECKE, W., "Thermally Excited Silicon Microactuators," IEEE TRANSACTIONS ON ELECTRON DEVICES, vol. 35, no. 6, pp. 758-763, 1988.

[35] MOULTON, T., and ANANTHASURESH, G. K., "Micromechanical devices with embedded electro-thermal-compliant actuation," Sensors and Actuators A: Physical, vol. 90, issues 1-2, pp. 38-48, 2001.

[36] LIN, L., and LIN, S. H., "Vertically driven microactuators by electrothermal buckling effects," Sensors and Actuators A, vol. 71, pp. 35-39, 1998.

[37] LERCH, P., SLIMANE, C. K., ROMANOWICZ, B., and RENAUD, P., "Modelization and characterization of asymmetrical thermal micro-actuators," J. Micromech. Microeng., vol. 6, pp. 134-137, 1996.

[38] COMTOIS, J. H., MICHALICEK, M. A., and BARRON, C. C., "Electrothermal actuators fabricated in four-level planarized surface micromachined polycrystalline silicon," Sensors and Actuators A, vol. 70, pp. 23-31, 1998.

[39] QUE, L., PARK, J. S., and GIANCHANDANI, Y. B., "Bent-Beam Electrothermal Actuators—Part I: Single Beam and Cascaded Devices," Journal of Microelectromechanical Systems, vol. 10, no. 2, pp. 247-254, 2001.

[40] HUANG, Q. A., and LEE, N. K. S., "Analysis and design of polysilicon thermal flexure actuator," J. Micromech. Microeng., vol. 9, pp. 64-70, 1999.

[41] HUANG, Q. A., and LEE, N. K. S., "Analytical modeling and optimization for a laterally-driven polysilicon thermal actuator," Microsystem Technologies, vol. 5, pp. 133-137, 1999.

[42] PAN, C. S., and HSU, W., "An electro-thermally and laterally driven polysilicon microactuator," J. Micromech. Microeng., vol. 7, pp. 7-13, 1997.

[43] LIN, L., and CHIAO, M., "Electrothermal responses of lineshape microstructures," Sensors and Actuators A, vol. 55, pp. 35-41, 1996.

[44] LU, S., DIKIN, D. A., ZHANG, S., FISHER, F. T., LEE, J., and RUOFF, R. S., "Realization of nanoscale resolution with a micromachined thermally actuated testing stage," Review of Scientific Instruments, vol. 75, no. 6, pp. 2154-2162, 2004.

[45] LU, S., GUO, Z., DING, W., and RUOFF, R. S., "Analysis of a microelectromechanical system testing stage for tensile loading of nanostructures," Review of Scientific Instruments, vol. 77, pp. 056103-1, 2006.

[46] VARONA, J., TECPOYOTL-TORRES, M., and HAMOUI, A. A., "Design of MEMS vertical–horizontal chevron thermal actuators," Sensors and Actuators, vol. A 153, pp. 127-130, 2009.

[47] ZHU, Y., CORIGLIANO, A., and ESPINOSA, H. D., "A thermal actuator for nanoscale in situ microscopy testing: design and characterization," Journal of Micromechanics and Microengineering, vol. 16, pp. 242-253, 2006.

[48] ZHU, Y., MOLDOVAN, N., and ESPINOSA, H. D., "A microelectromechanical load sensor for in situ electron and x-ray microscopy tensile testing of nanostructures," Applied Physics Letters, vol. 86, pp. 013506-1, 2005.

[49] ZHANG, X., and LIU, Z., "Superlenses to overcome the diffraction limit", Nature Materials, vol. 7, pp. 435-441, 2008.

[50] IPPOLITO, S. B , Goldberg, B. B., and ÜNLÜ, M. S., "High spatial resolution subsurface microscopy", Applied Physics Letters, vol. 78, no. 26, pp. 4071-4073, 2001.

[51] IPPOLITO, S. B , Goldberg, B. B., and ÜNLÜ, M. S., "Theoretical analysis of numerical aperture increasing lens microscopy", Journal of Applied Physics, vol. 97, pp. 053105-1, 2005.

[52] OXLEY, C. H., and HOPPER, R. H., "Effect of transparency within a semiconductor on emissivity mapping for thermal profile measurements of a semiconductor device", IET Science Measurement & Technology, vol. 1, no. 2, pp. 79-81, 2007.

[53] BEECHEM, T., GRAHAM, S., KEARNEY, S. P., PHINNEY, L. M., and SERRANO, J. R., "Invited Article: Simultaneous mapping of temperature and stress in microdevices using micro-Raman spectroscopy", Review of Scientific Instruments, vol. 78, pp. 061301-1, 2007.

[54] TANG, W. C., NGUYEN, T. C. H., and HOWE, R. T., "Laterally Driven Polysilicon Resonant Microstructures", Sensors and Actuators, vol. 20, pp. 25-32, 1989.

[55] WU, H., GRABARNIK, S, EMADI, A., GRAAF, G. D., and WOLFFENBUTTEL, R. F., "Characterization of thermal cross-talk in a MEMS-based thermopile detector array", Journal of Micromechanics and Microengineering, vol. 19, pp. 074022-1, 2009.

[56] YOUNG, J. Y. J., "Squeeze film damping for MEMS structures", MS Thesis, Massachusetts, 1998.

[57] CHANG, C. O., CHANG, G. E., CHOU, C. S., CHIEN, W. T. C., and CHEN, P. C., "In-plane free vibration of a single-crystal silicon ring", International Journal of Solids and Structures, vol. 45, pp. 6114-6132, 2008.

[58] MANKAME, N. D., and ANATHASURESH, G. K., "Comprehensive thermal modelling and characterization of an electro-thermal-compliant microactuator", Journal of Micromechanics and Microengineering, vol. 11, pp. 452-462, 2001.

[59] HUANG, Q. A., and LEE, N. K. S., "Analysis and design of polysilicon thermal flexure actuator", Journal of Micromechanics and Microengineering, vol. 9, pp. 64-70, 1999.

[60] LECESTRE, A., DUBOIS, E., VILLARET, A., SKOTNICKI, T., CORONEL, P., PATRIARCHE, G., and MAURICE, C., "Confined VLS growth and structural characterization of silicon nanoribbons", Microelectronic Engineering, vol. 87, pp. 1522-1526, 2010.

[61] MADRAS, P., DAILEY, E., and DRUCKER, J., "Spreading of Liquid AuSi on Vapor-Liquid-Solid-Grown Si Nanowires", Nanoletters, vol. 10, pp. 1759-1763, 2010.

[62] WEN, C. Y., REUTER, M. C., TERSOFF, J., STACH, E. A., and ROSS, F. M., "Structure, Growth Kinetics, and Ledge Flow during Vapor-Solid-Solid Growth of Copper-Catalyzed Silicon Nanowires", Nanoletters, vol. 10, pp. 514-519, 2010.

[63] HUANG, Q., LILLEY, C. M., BODE, M., and DIVAN, R., "Surface and size effects on the electrical properties of Cu nanowires", Journal of Applied Physics, vol. 104, pp. 023709-1, 2008.

[64] DURKAN, C., and WELLAND, M. E., "Analysis of failure mechanisms in electrically stressed gold nanowires", Ultramicroscopy, vol. 82, pp. 125-133, 2000.

[65] ZHANG, X.F., FUJITA, T., PAN, D., YU, J. S., SAKURAI, T., and CHEN, M. W., "Influences of grain size and grain boundary segregation on mechanical behavior of nanocrystalline Ni", Metallurgical and Materials Transactions A, vol. 41A, pp. 621-630, 2010.

[66] TORRE, F. D., Swygenhoven, H. V., and VICTORIA, M., "Nanocrystalline electrodeposited Ni: microstructure and tensile properties", Acta Materialia, vol. 50, pp. 3957–3970, 2002.

[67] WANG, C. L., ZHANG, M., and NIEH, T. G., "Nanoindentation creep of nanocrystalline nickel at elevated temperatures", Journal of Physics D: Applied Physics, vol. 42, pp. 115405-1, 2009.